Experimental Search for the Decay Mode $K_L \to \pi^+\pi^-e^+e^-$

Tadashi Nomura

January, 1998

A dissertation submitted
by
Tadashi Nomura
to
The Graduate School
in Partial Fulfillment of Requirements
for the Degree of
Doctor of Science (physics)
in
Department of Physics
Faculty of Science
Kyoto University

Abstract

In this thesis, the result of an experimental search for the $K_L \to \pi^+\pi^-e^+e^-$ decay mode is reported.

Rare decay mode $K_L \to \pi^+\pi^-e^+e^-$ may provide a good testing ground for studying CP violation phenomena. Its decay amplitude contains both CP-even and CP-odd components, and the existence of their interference manifests CP violation. One of the observables of this interference is an asymmetry of the partial decay rate, which can be seen in the angle of $\pi^+\pi^-$ and e^+e^- plane. One of the theoretical calculations predicts its branching ratio of $O(10^{-7})$ and the asymmetry of about 14%. This relatively large and well calculated observable opens up new prospects to lead thorough and detailed investigation of CP violation.

In the experimental status, this mode has not been observed and only upper limit of its branching ratio has been reported. It is important to study this mode and to build up a foundation for observing new CP violation effects.

We have performed the experimental search for the decay $K_L \to \pi^+\pi^-e^+e^-$ at the neutral beam line (K0) of the 12-GeV/c Proton Synchrotron at High Energy Accelerator and Research Organization (KEK). The experiment, KEK-E162, aimed to study K_L rare decay modes with 3 or more daughters including e^+e^- pairs. The neutral kaon beam was produced by the interaction of 12-GeV/c primary protons with the target. The experimental setup was composed of 4-m-long decay volume, four sets of trigger hodoscope planes, a spectrometer which consisted of an analyzing magnet and four sets of large drift chambers, a gas Cherenkov counter to identify electrons, and an electromagnetic calorimeter with pure CsI crystals most downstream of the detectors.

We present the result of the data taken during five weeks before summer in 1996.

After the event reconstruction and some kinematical cuts to reduce backgrounds, we have found no evidence for the decay, while 2618 $K_L \to \pi^+\pi^-\pi^0$ with $\pi^0 \to e^+e^-\gamma$ events have been recorded as the normalization process. This results in the upper limit of 4.6×10^{-7} ($M_{ee} \geq 4MeV/c^2$) for the branching ratio of $K_L \to \pi^+\pi^-e^+e^-$ at a 90% confidence level. This result has improved the previous upper limit by a factor of 5.

Contents

List of Tables

List of Figures

Dedication

To my parents,

To my wife and little daughter.

Acknowledgements

Since I began to grapple with this hard and challenging and interesting subject in 1988, many people have given a helping hand to me and to our experiment. After carrying out the work in this dissertation, I am very glad to express my gratitude to the following people.

I am indebted in particular to my supervisor, Prof. Noboru Sasao, for his continuous support and useful advise. He gave me a chance to touch the world of the experimental particle physics and to join this attractive experiment.

I am grateful to my former supervisor, Prof. Kozo Miyake, for his guidance in early year in the graduate school.

I would like to thank all collaborators of the KEK-E162 experiment, Prof. H. Sakamoto, Dr. Y. Hemmi, Dr. H. Kurashige, Mr. M. Suehiro, Mr. Y. Matono, Mr. K. Murakami, Mr. Y. Takeuchi, who are the members of High Energy group of Kyoto University, and Prof. Y. Fukushima, Dr. T. Taniguchi, Dr. Y. Ikegami, Mr. T. T. Nakamura, who belong to KEK, and Prof. M. Asai, who is the staff of Hiroshima Institute of Technology.

I wish to thank to former members of the experiment, Mr. H. Kobayashi, who designed and constructed the CsI calorimeter, Dr. M. Morii, who designed and laid a foundation for the construction of drift chambers, Mr. T. Yamashita, who contributed to the construction of the calibration system for the calorimeter, Mr. K. Shibata, who also worked on the calorimeter construction, and other juniors who helped in detector construction.

I express my gratitude to Prof. H. Sugawara, Prof. K. Nakai and Prof. S. Iwata for their support and encouragement. We thank the staff of Mechanichal Engineering Center at KEK, in particular Mr. Y. Higashi and Mr. Y. Funahashi, for their contributions in construction of the detector. All the long time I worked on the construction of Cherenkov counter and drift chambers, their kind cooperation encouraged me. We also appreciate the support from the operating crew of the Proton Synchrotron, members of Beam Channel group and Computing Center at KEK.

I would like to acknowledge the support provided by JSPS Fellowship for Japanese Junior Scientists (F.Y.1993–1994).

Finally, I thank my parents for their support during the long years of my education. And, I wish to thank my wife, Kasumi Nomura, for her loving help and encouragement.

Chapter 1

Introduction

In present particle physics, the study of CP violating phenomena and their origin is one of the important issues. In spite of many experimental efforts since the discovery of CP violation in the $K_L \to 2\pi$ mode [1] in 1964, CP violating phenomena are observed only in the specific K^0 decay modes. In the theoretical field, the Standard Model can explain the phenomenon by a phase in the Cabbibo-Kobayashi-Maskawa (CKM) matrix [2], and some other theories such as the superweak theory [3] exist being consistent with experimental data. It will be a great help for testing these theories to establish CP violation in other systems, for example, in the $B^0 - \bar{B}^0$ system and other K^0 decay channels. The decay mode $K_L \to \pi^+\pi^-e^+e^-$ may provide an interesting testing ground for investigating CP violation, as will be described in next section. Experimentally, this mode has not been observed and only an upper limit of its branching ratio has been reported. The purpose of this study is to search for the decay mode $K_L \to \pi^+\pi^-e^+e^-$ and to build up a foundation of new testing field for CP violation.

In this thesis, experimental search for the decay mode $K_L \to \pi^+\pi^-e^+e^-$, conducted with 12-GeV/c proton synchrotron at High Energy Accelerator Research Organization (KEK), will be discussed. Data used here have been taken during five weeks, spanning in three beam cycles, before summer in 1996. At first, the physics motivation and the experimental status concerned with the decay mode are introduced in this chapter. Next, the explanation of our experiment will be made in Chapter 2. The general procedure of the analysis will be mentioned in Chapter 3. In Chapter 4, the analysis for the normalization mode $K_L \to \pi^+\pi^-\pi^0$ with $\pi^0 \to e^+e^-\gamma$ ($K_L \to \pi^+\pi^-\pi^0_D$) and the target mode $K_L \to \pi^+\pi^-e^+e^-$ will be discussed. Finally, the result of the experiment will be summarized. The Monte Carlo simulation we employed will be described in detail in Appendix A.

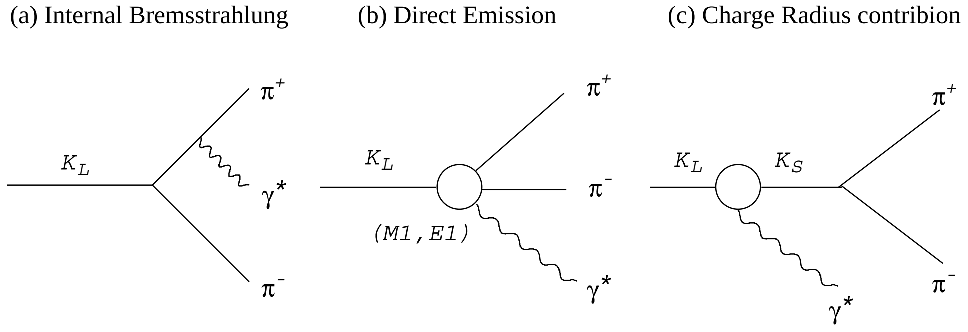

Figure 1.1: Diagrams illustrating (a) internal bremsstrahlung, (b) direct M1 or E1 emission and (c) K^0 charge radius contribution

1.1 Theoretical Interest

The decay $K_L \to \pi^+\pi^-e^+e^-$ is expected to occur via $\pi^+\pi^-\gamma^*$ intermediate state converting the virtual photon into an e^+e^- pair.

At first, the CP property of the decay $K_L \to \pi^+\pi^-\gamma$ is considered, which is closely related to our target mode $K_L \to \pi^+\pi^-e^+e^-$. In case of real γ, two components for the photon emission are contained in the amplitude, which have been known experimentally [4]. One is an internal bremsstrahlung (IB) associated with the $K_L \to \pi^+\pi^-$ and the other is a direct emission (DE), which are illustrated in Figure 1.1(a)(b), substituting γ^* for real γ. The photon emission by magnetic and electric multipoles, MJ and EJ where J denotes to the angular momentum, has its CP eigenvalue of $(-1)^{J+1}$ and $(-1)^J$, respectively. The internal bremsstrahlung has a form equivalent to EJ term with odd J. Since $\pi^+\pi^-$ system is CP-even state, the final state $\pi^+\pi^-\gamma$ has both CP=+1 and -1 states, corresponding to IB or E1 and M1 contributions respectively, in the approximation of retaining only dipole terms in direct emission. The interference between two different CP states doesn't appear if the photon polarization is not measured. Thus, in order to study CP violation experimentally in this mode, we must measure the photon polarization directly or indirectly.

As a probe of the photon polarization, $K_L \to \pi^+\pi^-e^+e^-$ is the mode with a good prospect, which is its internal conversion process. The polarization can be measured indirectly by studying the correlation of the e^+e^- plane relative to the $\pi^+\pi^-$ plane, and CP violating interference is revealed. Calculations of the decay $K_L \to \pi^+\pi^-e^+e^-$ have been carried out in some papers [5]. Along their procedure, calculations and results are reviewed below.

The matrix element of the decay $K_L \to \pi^+\pi^-e^+e^-$ is represented as

$$\mathcal{M}(K_L \to \pi^+\pi^-e^+e^-) = \mathcal{M}_{IB} + \mathcal{M}_{DE}^{M1} + \mathcal{M}_{DE}^{E1} + \mathcal{M}_{CR} \ , \tag{1.1}$$

where the terms $\mathcal{M}_{IB}, \mathcal{M}_{DE}^{M1}$ and $\mathcal{M}_{DE}^{E1}$ denote the internal bremsstrahlung, magnetic and electric dipole, respectively. An additional term $\mathcal{M}_{CR}$ is the contribution of the K^0 charge radius, as shown in Fig.1.1(c), which can exist when the photon is virtual.

If we use the notation: $K_L(P) \to \pi^+(p_+)\pi^-(p_-)e^+(k_+)e^-(k_-)$, the matrix element can be written as

$$\begin{aligned}
&\mathcal{M}(K_L \to \pi^+\pi^-e^+e^-) \\
= \;& e|f_s| \left[g_{IB} \left[\frac{p_{+\mu}}{p_+ \cdot k} - \frac{p_{-\mu}}{p_- \cdot k} \right] \right. \\
+ \;& \frac{g_{E1}}{m_K^4} \left[(P \cdot k) p_{+\mu} - (p_+ \cdot k) P_\mu \right] \\
+ \;& \frac{g_{M1}}{m_K^4} \epsilon_{\mu\nu\rho\sigma} k^\nu p_+^\rho p_-^\sigma \\
+ \;& \left. \frac{g_{CR}}{m_K^2} \left[k^2 P_\mu - (P \cdot k) k_\mu \right] \frac{1}{k^2 - 2P \cdot k} \right] \frac{e}{k^2} \bar{u}(k_-) \gamma^\mu v(k_+) \ , \qquad (1.2)
\end{aligned}$$

where $k = k_+ + k_-$. The discussion of the parameters in the expression follows below.

1. f_s is the coupling constant for $K_S \to \pi^+\pi^-$ defined by

$$\Gamma(K_S \to \pi^+\pi^-) = \frac{|f_s|^2}{16\pi m_K} \left[1 - \frac{4m_\pi^2}{m_K^2} \right]^{1/2} . \qquad (1.3)$$

2. The parameter g_{IB} defines the internal bremsstrahlung. It is given by

$$g_{IB} = \eta_{+-} \cdot \frac{f_s}{|f_s|}, \qquad (1.4)$$

   where η_{+-} is the CP violating parameter, $A(K_L \to \pi^+\pi^-)/A(K_S \to \pi^+\pi^-)$. The phase of g_{IB} is $\Phi_{+-} + \delta_0$, where Φ_{+-} is the phase of η_{+-} and δ_0 is the $I = 0$ $\pi\pi$ s-wave phase shift at $s_\pi = m_K^2$ $(\delta_0(m_K^2))$. Here s_π is the square of the $\pi\pi$ invariant mass, i.e. $s_\pi = (p_+ + p_-)^2$.

3. The parameter g_{M1} defines the CP-odd M1 transition. The absolute value of g_{M1} is measured by the decay rate of the M1 radiation in the $K_L \to \pi^+\pi^-\gamma$, and obtained to be 0.76. The phase of g_{M1} is that of p-wave $I = 1$ $\pi\pi$ scattering at $\sqrt{s_\pi}$ $(\delta_1(s_\pi))$ and also factor of i as a consequence of CPT invariance.

4. The parameter g_{E1} was estimated to be small in [5], compared with g_{M1} and/or g_{IB}. Also the parameter g_{CR} resulted in small contribution. So detail explanation of them is skipped here.

From the matrix element in Eqn.(1.2), differential decay rate is calculated in three variables:

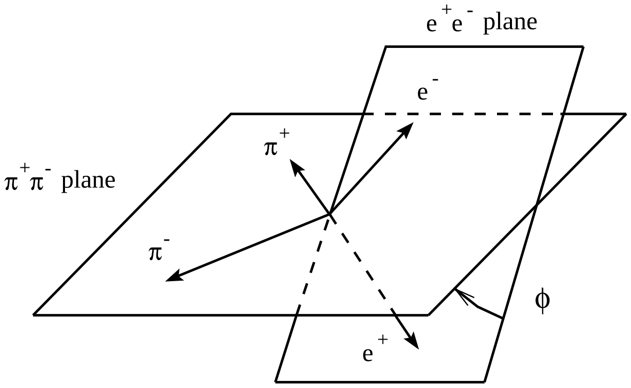

Figure 1.2: Schematic drawing for the definition of the angle ϕ, which is the angle between planes normal to the e^+e^- and $\pi^+\pi^-$ planes.

(i) $x = (p_+ + p_-)^2/m_K^2$ (normalized invariant mass of pions),

(ii) $y = (k_+ + k_-)^2/m_K^2$ (normalized invariant mass of electrons), and

(iii) ϕ (the angle between normals to the e^+e^- and $\pi^+\pi^-$ planes).

The last variable ϕ, illustrated in Fig.1.2, is determined as follows. Let $(\vec{p}_+ + \vec{p}_-)$ be parallel to the positive z direction in the K_L rest frame. Then the unit vector to the +z direction is represented as

$$\vec{n_z} = (\vec{p}_+ + \vec{p}_-)/|(\vec{p}_+ + \vec{p}_-)| \; . \tag{1.5}$$

The unit vectors normals to the $\pi^+\pi^-$ plane

$$\vec{n_\pi} = (\vec{p}_+ \times \vec{p}_-)/|(\vec{p}_+ \times \vec{p}_-)| \tag{1.6}$$

and to the e^+e^- plane

$$\vec{n_l} = (\vec{k}_+ \times \vec{k}_-)/|(\vec{k}_+ \times \vec{k}_-)| \tag{1.7}$$

then lies in the x-y plane and have components

$$\vec{n_\pi} = (\cos\phi_\pi, \sin\phi_\pi, 0) \; ,$$

$$\vec{n_l} = (\cos\phi_l, \sin\phi_l, 0) \; ,$$

where ϕ_π and ϕ_l lie between 0 to 2π. The angle ϕ is defined as

$$\phi = (\phi_\pi - \phi_l) mod(2\pi)$$

and ranges from 0 to 2π. Note that the relation between the angle ϕ and the unit vectors can be written as

$$\cos\phi = \vec{n_l} \cdot \vec{n_\pi} \; , \tag{1.8}$$

$$\sin\phi = (\vec{n_l}\times\vec{n_\pi})\cdot\vec{n_z}. \tag{1.9}$$

The result for the decay rate, normalized by that of $K_S \to \pi^+\pi^-$, is

$$\begin{aligned}
&\frac{\Gamma(K_L \to \pi^+\pi^- e^+e^-)}{\Gamma(K_S \to \pi^+\pi^-)} \\
&= \frac{\alpha^2}{16\pi^2\lambda^{1/2}(1,\mu^2,\mu^2)} \int_{4\nu^2}^{(1-2\mu)^2} dy \frac{\lambda^{1/2}(y,\nu^2,\nu^2)}{y^2} \\
&\quad \int_{4\mu^2}^{(1-\sqrt{y})^2} dx \lambda^{1/2}(1,x,y) \int_0^{2\pi} \frac{d\phi}{2\pi} F(x,y,\phi)\ ,
\end{aligned} \tag{1.10}$$

where the notation

$$\mu^2 = \frac{m_\pi^2}{m_K^2},\ \nu^2 = \frac{m_e^2}{m_K^2}$$

is introduced and $F(x,y,\phi)$ is given by, neglecting the electron mass and terms concerned with small g_{E1},

$$\begin{aligned}
&F(x,y,\phi) \\
&= \frac{8}{3}|g_{IB}|^2 \left\{ \frac{-16\lambda^{1/2}(x,\mu^2,\mu^2)x\mu^2}{x^2(x+y-1)^2 - \lambda(1,x,y)\lambda(x,\mu^2,\mu^2)} \right. \\
&\quad \left. + \frac{4(x-2\mu^2)}{(x+y-1)\lambda^{1/2}(1,x,y)} \ln(L) [\frac{1}{2}(1+2\sin^2\phi)] \right\} \\
&+ \frac{8}{3}|g_{IB}|^2 \left\{ \frac{16x^2y\lambda^{1/2}(x,\mu^2,\mu^2)x\mu^2}{\lambda(1,x,y)[x^2(x+y-1)^2 - \lambda(1,x,y)\lambda(x,\mu^2,\mu^2)]} \right. \\
&\quad \left. - \frac{8x^2y}{(x+y-1)\lambda^{3/2}(1,x,y)} \ln(L) [\frac{1}{2}(1-2\sin^2\phi)] \right\} \\
&+ \frac{8}{3}\mathrm{Re}(g_{M1}g_{IB}^*) \frac{1-x-y}{\lambda^{1/2}(1,x,y)} \\
&\quad \left\{ -2\frac{\mu^2(1-x-y)^2 + y\lambda(x,\mu^2,\mu^2)}{(x+y-1)\lambda^{1/2}(1,x,y)} \ln(L) + \lambda^{1/2}(x,\mu^2,\mu^2) \right\} [\sin\phi\cos\phi] \\
&+ \frac{1}{18}|g_{M1}|^2 \frac{1}{x^2}\lambda(1,x,y)\lambda^{3/2}(x,\mu^2,\mu^2)[\frac{1}{2}(1+2\cos^2\phi)] \\
&+ \frac{1}{3}\frac{|g_{CR}|^2}{(x-1)^2}\frac{y}{x}\lambda(1,x,y)\lambda^{1/2}(x,\mu^2,\mu^2)\ .
\end{aligned} \tag{1.11}$$

The dependence of each term on the angle ϕ is indicated in square brackets. Here, the abbreviations

$$L = \frac{(x+y-1)x + \lambda^{1/2}(1,x,y)\lambda^{1/2}(x,\mu^2,\mu^2)}{(x+y-1)x - \lambda^{1/2}(1,x,y)\lambda^{1/2}(x,\mu^2,\mu^2)}\ ,$$

$$\lambda(x,y,z) = x^2 + y^2 + z^2 - 2(xy + yz + zx)$$

are used. Their resultant total branching ratio is

$$B(K_L \to \pi^+\pi^-e^+e^-) = (1.3 \times 10^{-7})_{IB} + (1.8 \times 10^{-7})_{M1} + (0.04 \times 10^{-7})_{CR} \ .$$

In the formula of the decay rate, ϕ dependence of each term characterizes its property under CP transformation. From the expressions in Equations (1.6)–(1.9), it can be obtained that $\cos\phi$ doesn't changes its sign and $\sin\phi$ changes sign under the sequence of transformation C ($\vec{p}_\pm \to \vec{p}_\mp, \vec{k}_\pm \to \vec{k}_\mp$) and P ($\vec{p}_\pm \to -\vec{p}_\pm, \vec{k}_\pm \to -\vec{k}_\pm$). As can be seen in Eqn.(1.11), the interference term ($g_{M1}g^*_{IB}$) has the ϕ dependence of $\sin\phi\cos\phi$, and then it changes sign under CP transformation and so is the CP violating one. We can see the effect through the asymmetry such as

$$A = \frac{\displaystyle\int_0^{\pi/2} \left(\frac{d\Gamma}{d\phi}\right) d\phi - \int_{\pi/2}^{\pi} \left(\frac{d\Gamma}{d\phi}\right) d\phi}{\displaystyle\int_0^{\pi/2} \left(\frac{d\Gamma}{d\phi}\right) d\phi + \int_{\pi/2}^{\pi} \left(\frac{d\Gamma}{d\phi}\right) d\phi} \ .$$

This asymmetry, integrated over x and y, is calculated as $|A| \approx 15\% \sin\Theta$ [1], where

$$\Theta = arg(g_{M1}g^*_{IB}) = \Phi_{+-} + \delta_0 - \bar{\delta_1} \ ,$$

and $\bar{\delta_1}$ denotes an average phase in the $\pi\pi$ p-wave $I = 1$ channel. Inserting $\Phi_{+-} = 43°$, $\delta_0 = 40°$, and $\bar{\delta_1} \approx 10°$ (assuming an average $\pi\pi$ mass of approximately 0.4 GeV), $|A|$ is estimated to be about 14%. This effect arises from the admixture of CP-even component in the K_L wave function. In this sense, it is an example of indirect CP violation.

In another paper [6], effects of direct CP violation are estimated but are found to be small. In summary, the decay $K_L \to \pi^+\pi^-e^+e^-$ is quite interesting for studying CP violation effect. The observable parameter is relatively large and well calculated. Although our sensitivity for the mode, described in later chapter, does not reach to the level to see CP asymmetry effect, it is important to study for the decay mode $K_L \to \pi^+\pi^-e^+e^-$ and to build up a foundation of new testing field for CP violation.

1.2 Experimental Status

The experimental status of the $K_L \to \pi^+\pi^-e^+e^-$ and its related decay modes is summarized in this section.

In the decay $K \to \pi^+\pi^-\gamma$, the branching ratio was measured separately for a direct emission component (DE) and for a internal bremsstrahlung component

---

[1] A cosine instead of sine factor was used in Ref.[5], but it corrected later in the Erratum [5]

(IB) [4]. In this experiment, both K_L and K_S decays were collected simultaneously. The branching ratio of $K_S \to \pi^+\pi^-\gamma$ was measured:

$$\frac{B(K_S \to \pi^+\pi^-\gamma; E^*_\gamma > 20\mathrm{MeV})}{B(K_S \to \pi^+\pi^-)} = (6.36 \pm 0.09 \pm 0.05) \times 10^{-3} ,$$

where E^*_γ is the energy of photon in the kaon rest frame. Since this mode is dominated by the internal bremsstrahlung process, the energy spectrum of photons from IB contribution could be obtained.

In the measurement of K_L decay, relative strength of two amplitudes was determined by analyzing the energy spectrum of γ. The energy spectrum was fitted to a linear combination of the K_S spectrum, which was assumed to be same as the K_L IB contribution, and a Monte Carlo prediction for the photon energy spectrum resulting from the direct emission (DE) K_L decay. The resultant branching ratios of IB and DE contribution were reported to be

$$\frac{Br(K_L \to \pi^+\pi^-\gamma; IB, E^*_\gamma > 20\mathrm{MeV})}{Br(K_L \to \pi^+\pi^-)} = (6.90 \pm 0.21) \times 10^{-3} ,$$

and

$$\frac{Br(K_L \to \pi^+\pi^-\gamma; DE, E^*_\gamma > 20\mathrm{MeV})}{Br(K_L \to \pi^+\pi^-)} = (15.0 \pm 0.6) \times 10^{-3} ,$$

respectively.

In our target mode $K_L \to \pi^+\pi^-e^+e^-$, an upper limit of the branching ratio has been placed

$$Br(K_L \to \pi^+\pi^-e^+e^-) < 2.5 \times 10^{-6} ,$$

by the experiment which was performed at Institute of Theoretical and Experimental Physics (ITEP) in Moscow in 1983 [7]. In the experiment, the detector was composed of a spectrometer which consisted of an analyzing magnet and wire spark chambers, hodoscopes, a calorimeter and a muon detector. The experiment was aimed to search for K_L decays which contain an e^+e^- pair and two charged particles, such as $K_L \to e^+e^-e^+e^-$, $K_L \to \mu^+\mu^-e^+e^-$, and $K_L \to \pi^+\pi^-e^+e^-$. As the normalization of the branching ratio, 1002 events of the decay $K_L \to \pi^+\pi^-\pi^0$ with $\pi^0 \to e^+e^-\gamma$ were recorded, while no $K_L \to \pi^+\pi^-e^+e^-$ event was observed.

Recently, the observation of about 20 events has been mentioned in the XXVI-th International Conference on High Energy Physics [8], but the branching ratio have not been reported.

Chapter 2

Explanation of the Experiment

The experiment to search for the decay mode $K_L \to \pi^+\pi^-e^+e^-$ was performed at the beam line, called K0 channel, in the East Counter Hall of the Proton Synchrotron at High Energy Accelerator Research Organization (KEK). The experiment E162 started to search for $K_L \to \pi^0e^+e^-$ and other rare decay modes with electromagnetic products (e^+, e^-, γ). To achieve high sensitivities for these decay modes, large amount of data had to be taken and so the experiment had to be performed at very high counting rate. This required the well-defined beam line, the detector which could be operated in an extremely high rate environment, and good background rejection in the early stage of data taking.

In this chapter, descriptions of these items in the E162 experiment are given in order.

2.1 Beam Line

At first, the feature of the K0 beam line is explained. Figure 2.1 shows the side view of the neutral beam line. [1]

The K_L beam was produced by the interactions of 12 GeV/c primary protons with a 60-mm-long, 10-mm-diameter copper target. The primary beam was extracted from the main ring for 2 second during each 4 second cycle and its intensity was typically 1×10^{12} protons per pulse. Before the target, it was bent upward (+2°) by a steering magnet (BS1) and then downward (-4°) by BS2 to strike the target at an angle of 2°. The production angle (2°) was determined taking account of the K_L yield and the ratio of produced K_L to neutrons. Secondary neutral beam had the divergence of ±4 mrad horizontally and ±20 mrad vertically, defined by a series of collimators embedded in sweeping magnets. The rectangular beam with fairly large aspect ratio (1:5) was a compromise between

---

[1] In our experiment, the position was represented in the right-hand coordinate system, where X- and Y-axis denoted the horizontal and vertical direction respectively, and Z-axis was defined as the neutral beam direction. Its origin was set at the center of the target.

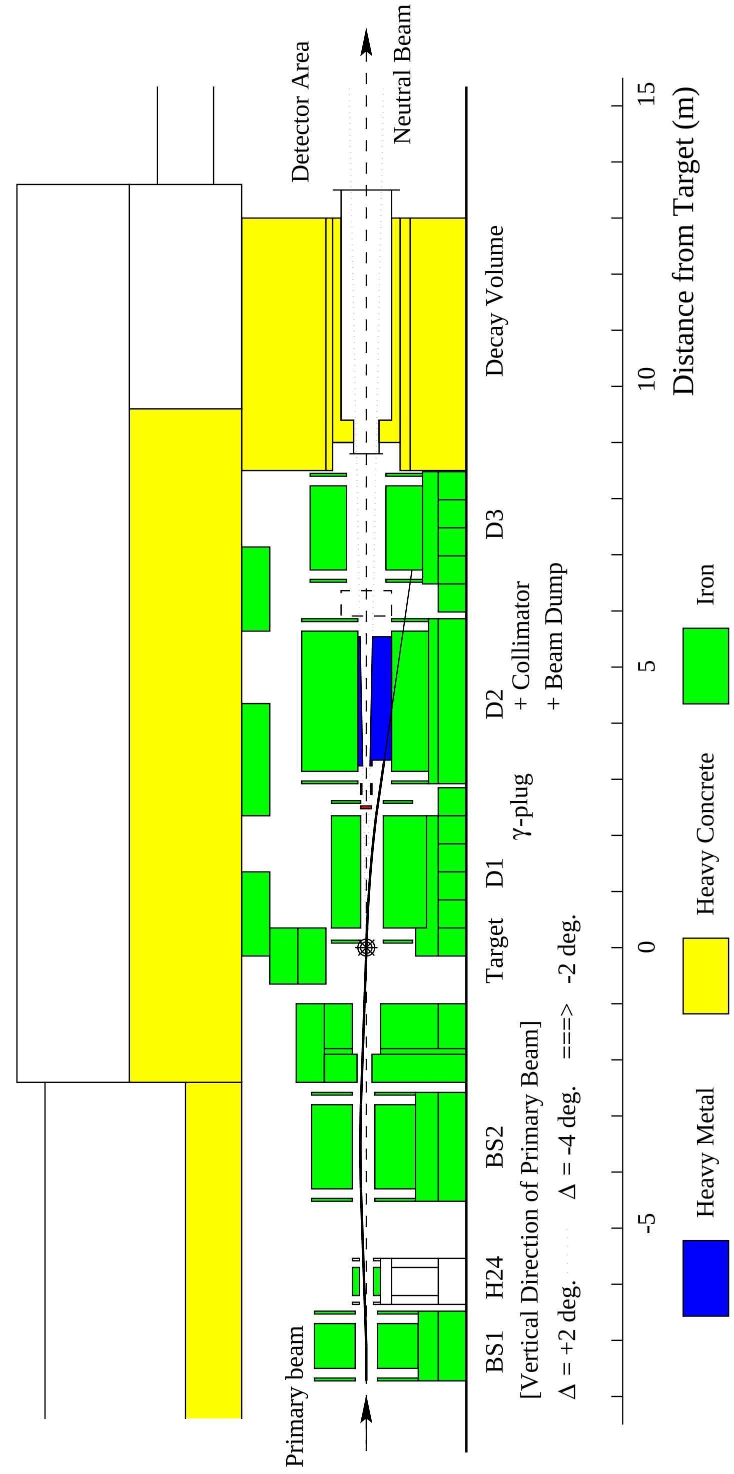

Figure 2.1: Side view of the neutral beam line : K0 line.

large aperture (i.e. many kaons) and narrow width (i.e. small beam hole in detectors).

A 2-m-long magnet immediate downstream of the target (D1) bent down the primary beam to the beam dump and swept out charged particles produced at the target. Near the end of D1 magnet, at 2.5 m downstream of the target where the primary beam was separated from the neutral beam path, a 50-mm-thick lead block (γ-plug) was placed in the neutral beam, to remove photons produced at the target. Photons were converted into a e^+e^- pair and then swept out by the magnetic field. The main collimator, as well as the primary beam dump, was embedded in the second sweeping magnet (D2). They were 2.5-m-long in the beam direction and made of the heavy metal (about 90 % tungsten, density of 17.13 g/cm^3). The third 2-m-long sweeping magnet (D3) was placed at Z=6.5m which also had a brass collimator in it. These sweeping magnets were operated at about 2 Tesla.[2]

The neutral beam after D3 magnet still included not only neutral kaons but also neutrons and photons.[3] They created background events by the interaction with materials in the beam region. Management of these background events at the trigger level as well as offline analysis was one of the hurdles to overcome in the course of the experiment. A 4-m-long decay volume, which followed from Z=9.5m, was pneumatically connected with the beam duct in D3 magnet, and was filled with helium gas at atmospheric pressure[4] to keep unwanted interactions as small as possible. We used a laminated film of Mylar (12μm $\times 2$) and aluminum foils (9μm $\times 2$) for its window which had low gas permeability, to prevent detectors from being damaged by penetrating helium gas.

2.2 Detector

The E162 detector system was originally designed to be optimum for the decay $K_L \to \pi^0 e^+ e^-$, whose final state consists of two electrons and two photons. Figure 2.2 shows the schematic view of E162 detector system. The detector design was done as follows. The system should measure energies and momenta of all components to reconstruct events. We selected the configuration of a spectrometer to determine momenta of charged particles, a calorimeter placed at most downstream position of detectors to measure energies and positions of electrons and gammas. Several sets of trigger scintillators and gas Cherenkov counter were added to notify passages of charged particles and to identify electrons mainly

---

[2] D2 magnet could not be operated due to trouble during the experiment. The influence on the counting rate was examined and found to be small.

[3] The ratio of neutron flux to K_L flux was estimated to be about 20 from the result of a beam line survey.

[4] It was designed to form a vacuum but was not evacuated due to delay of the vacuum window development.

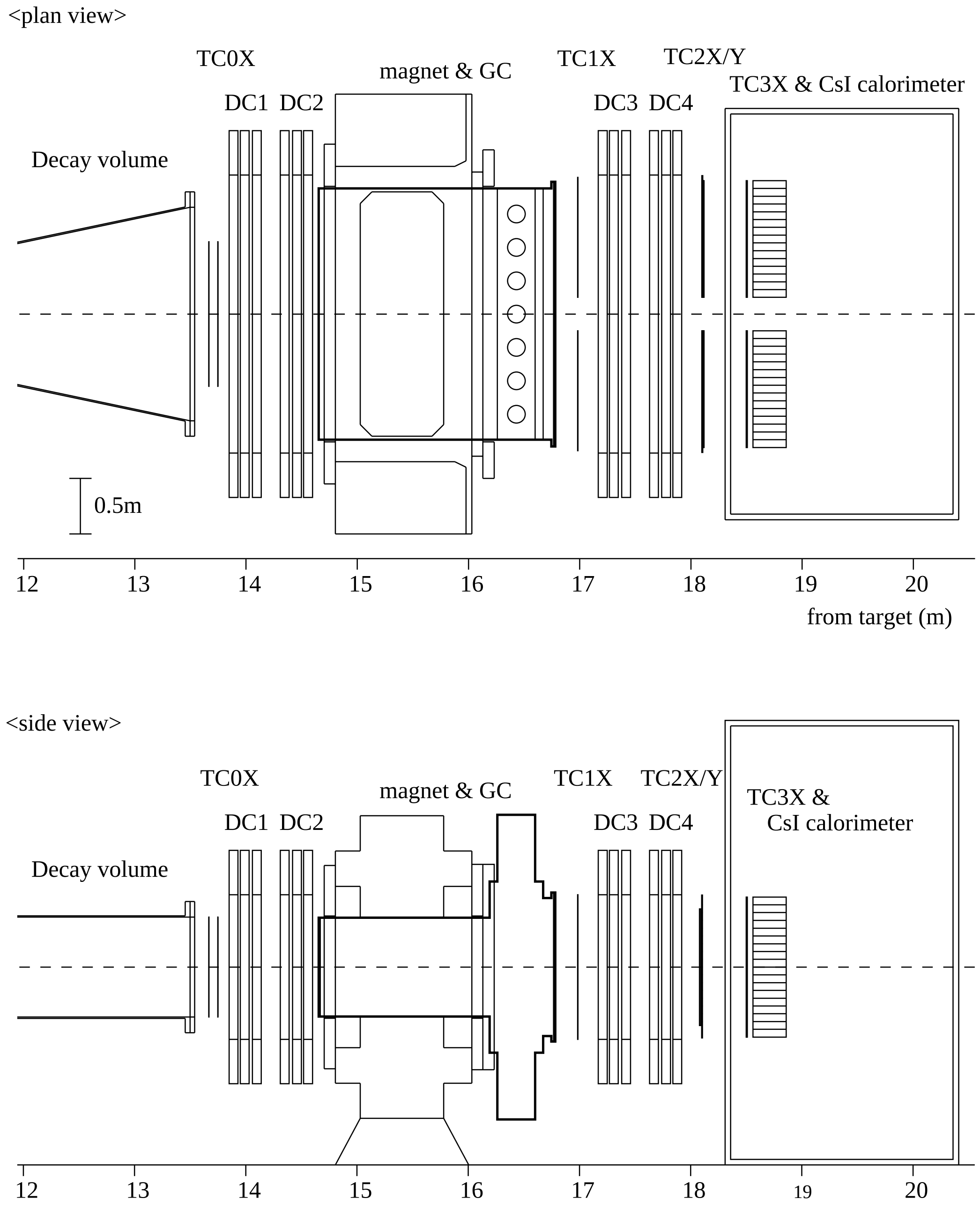

Figure 2.2: Schematic view of E162 detector system.

in data-taking stage. In the arrangement of components above, the design concept was to maximize acceptances for K_L decays: the detectors should have as large active areas as possible and should be put upstream within practical range. Thus, for example, the radiator part of gas Cherenkov counter was located inside an analyzing magnet gap, and there was only minimum vacant space between detectors. Another design philosophy was good performance in high counting rate environments, keeping high efficiencies and good resolutions. This required detectors to have narrow signal width, good time resolving power, and constant gain in any operating conditions. It was one of the most important points to determine structures of detectors and readout systems. In following subsections, each component of detectors is described in detail.

2.2.1 Spectrometer

A spectrometer, which determined momenta of charged particles, consisted of two sets of upstream drift chambers, an analyzing magnet, and two sets of downstream drift chambers.

The structure of the drift chambers is shown in Figure 2.3. Each drift chamber had active area of 2.5 m wide by 1.3 m high, covering the neutral beam region. A gas mixture of 50 % argon and 50 % ethane filled between two thin windows.[5] The window used was 50-μm-thick Mylar aluminized on both surface. Each detecting cell consisted of a sense wire (30 μm diameter gold-plated tungsten with tension of 50 gf) surrounding by field wires (100 μm diameter gold-plated copper-beryllium alloy with tension of 100 gf). The half-cell size was 4 mm, which was a compromise between rate capability of chambers and total number of readout wires. Pitches of sense wires in a plane were measured by an optical sensor in construction process and their deviations from nominal values were kept within 50 μm.

Each drift chamber set consisted of six readout planes, X-X$'$,U-U$'$,V-V$'$, in which wires were strung vertically and obliquely by ± 30°, respectively. A Signal from each wire was amplified and discriminated immediately at the chamber. The amplifier, shown in Fig.2.4, was composed of three stage of common base amplifiers, pole-zero circuits to cancel out 1/t tail of a chamber signal, baseline restorers, and a pulse height limiter which prevented dead time by large (wide) pulses. For the upstream chambers and downstream X-view chambers, the output from the discriminator was then transported to the counting hut and received by a buffer module which supplied power and threshold voltage to the amplifiers and discriminators. To reduce influence by accidental hits, 1 GHz pipelined time-to-digital converter (PLTDC) [11] was used to read hit time information. For the downstream U/V-view chambers, the output from the discriminator was directly

---

[5] Although we had planned to use a gas mixture containing CF_4, for the rate capability, in which the electron drift velocity is fast [9]-[10], we used a standard gas mixture of $Ar(50) - C_2H_6(50)$ for the simplicity of the calibration.

(a) The arrangement of Drift Chambers

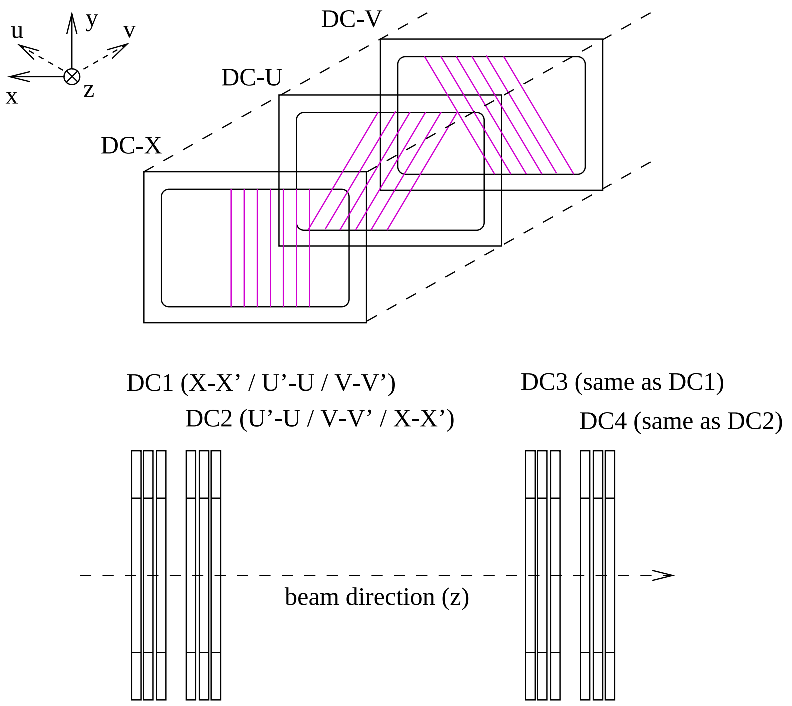

(b) The Cell structure of Drift Chamber

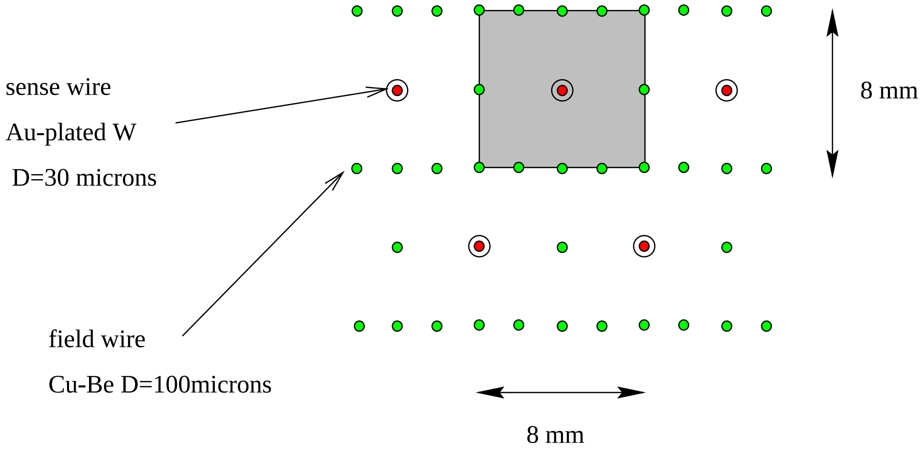

Figure 2.3: The structure of drift chamber, (a) schematic view of the arrangement and (b) the cell structure.

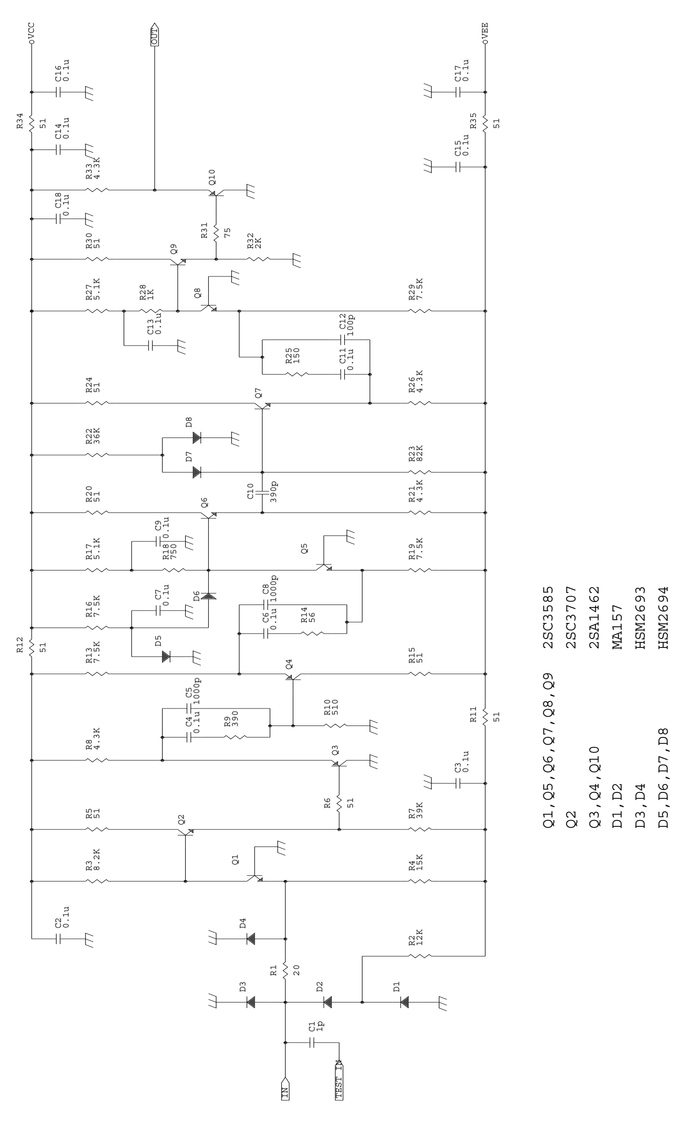

Figure 2.4: The electronic circuit of the pre-amplifier used for drift chambers. It was composed of three stage of common base amplifiers (around Q1,Q5,Q8), three pole-zero circuits (two for 1/t tail of a chamber signal and one for the pole of first stage amplifier), baseline restorers, and a pulse height limiter equipped at second common base amplifiers.

received by a compound module of time-to-analog and analog-to-digital converter (TAC), to save cost.

Efficiencies and position resolutions under typical beam conditions were examined by using straight tracks which were taken in the special run with the analyzing magnet off. Tracks used were reconstructed without hit information of the plane to be examined. The efficiency was evaluated by checking whether corresponding wire had an on-time hit or not, and was found to be more than 98%. The position resolution was defined as the deviation between calculated positions by the track and by hit time of the wire to be inspected. It was found to be about 250 μm; however it was slightly worse (300 μm) in the beam region.

A picture frame dipole magnet was used as an analyzing magnet. The pole piece was 0.5 m long in the beam direction, and its aperture was 2.2 m wide and 0.9 m high. The magnet provided a vertical field of 0.5 Tesla at the center. Its average field integral was 0.454 Tesla·m, corresponding to horizontal momentum kick of 136 MeV/c. The field strength was monitored by NMR probe throughout the experiment.

The momentum resolution of the spectrometer system was found to be 3 % at 1 GeV/c, which will be discussed in the next chapter.

2.2.2 Electromagnetic Calorimeter

In order to measure energies of electrons and photons, two banks of calorimeter were placed at both sides of neutral beam line (apart 300 mm), each consisted of 15(H) × 18(V) undoped Cesium Iodide (CsI) crystal blocks. Each CsI block was 70 mm × 70 mm in cross section and 300 mm in length (about 16 radiation length), and was read out by a photomultiplier (PMT) equipped at the downstream end of the block. The active area of the bank was 1.05 m wide by 1.26 m high. The calorimeter was placed in an air-conditioned housing box, where the temperature was kept constant (25°C) within ±0.2°C and the humidity was less than 30%.

Features of undoped Cesium Iodide scintillator are summarized below.

- High Z materials (Z=53(Cs),55(I)) and thus short radiation length (X_0=1.85 cm)

- Two components (fast and slow) of scintillation light [12]
  The fast component is characterized by short decay time constants (τ=10 and 36 nsec) and relatively narrow emission spectrum at 305 nm. The slow component is emitted over a several μsec with wide spectrum above 400 nm.

- Relatively large light output
  The light yield of the fast component is about 4% of standard NaI(Tl) scintillator, while that of the slow component differs from one crystal to another, which is thought to depend on impurities in crystals.

- Temperature dependence of light yield
  The temperature coefficients for both fast and slow components are similar. They were measured to be -1.5 %/°C.

- Slightly hygroscopic
  Although care should be taken not to expose crystals to humid atmosphere, it is unnecessary to seal them hermetically (like NaI).

Especially, the characteristic of fast scintillation response is suited for our purpose, to achieve high rate capability. Each block was wrapped round by thin Teflon sheet and aluminized Mylar to improve light collection efficiency.

We employed a 2″ head-on type photomultiplier (Hamamatsu R4275-02) to detect a scintillation light. It had a UV-glass window to transmit a fast component light from a CsI crystal, and had a 8-stage linear focus dynodes structure. Voltages between dynodes were supplied by a transistorized base (Hamamatsu E4270), designed by us with Hamamatsu Photonics Co., which stabilized voltage distribution even under high counting rate environment. By using them, a photomultiplier gain was kept constant (within 2% decrease) up to an anode current of 400 μA, which was equivalent to the case when a 1 GeV electron struck a block at the rate of 2 MHz. A pulse linearity was also measured on the bench and found to be within 2% during the current range from 0.7 to 5.5 GeV in the equivalent electron energy. To avoid heat localization, each PMT base was temperature-controlled by air blow.

Several optical elements were equipped, as shown in Figure 2.5, between a CsI crystal and a photomultiplier window. A 30 mm-thick quartz light guide was glued onto a photomultiplier window by the epoxy resin (Epotec-305), whose transmittance at the wavelength of 300 nm was above 80 %. Next, a bandpass optical filter (KENKO U-330) was glued to pass selectively the fast component. It cut off most of the slow component, which could cause a baseline shift by pile-up effects. A silicone “cookie” was put between a crystal and an optical filter to make a photomultiplier detachable from a CsI block.

Each block had two quartz fiber inputs on its downstream end. Through one of them, a light from a Xe flash lamp was injected into a crystal to monitor the light transmittance of a crystal and/or the gain variation of a photomultiplier. The other was reserved for the light from a YAG laser, which, however, was not implemented in the experiment.

An analog signal from each PMT was transported into a buffer module in the electronics hut. It divided the signal into several ways: to an analog-to-digital converter (ADC [13]), to sum-amplifiers, to a time-to-digital converter (TDC [14]) via a discriminator, and to a processor used in the level 2 trigger. The sum-amplifier module produced an analog signal proportional to the energy deposit, summed over 18(15) CsI blocks in each column(row) in the stack. It had a baseline restorer to prevent an output signal from the baseline shift due to the

(a) Schematic view of the pure CsI array
15(X) x 18(Y) x 2(L/R) blocks

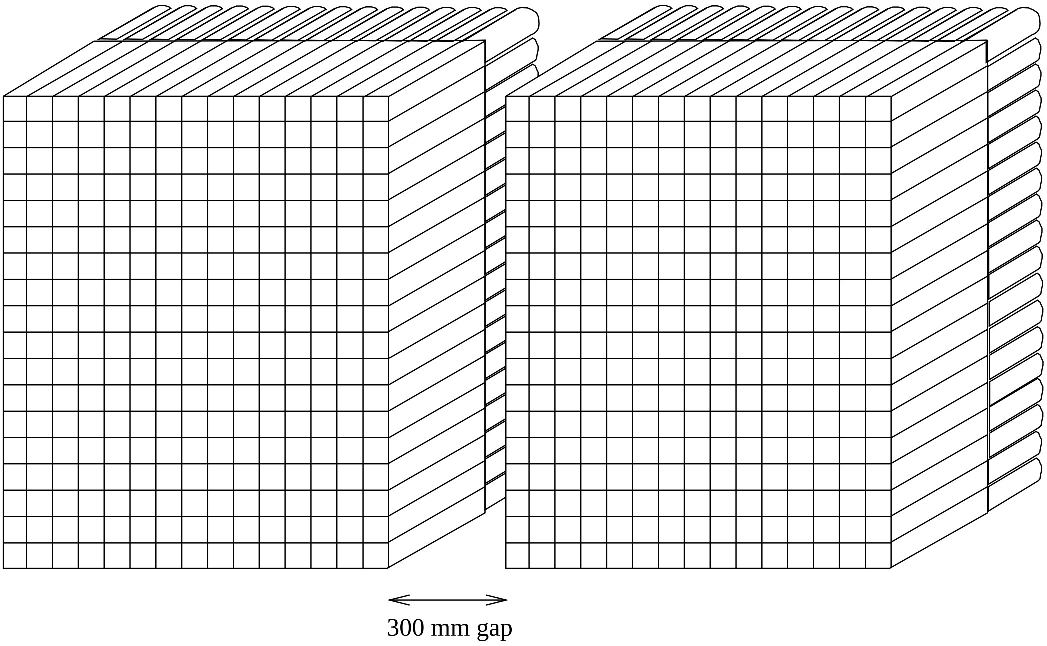

(b) A module of the CsI calorimeter

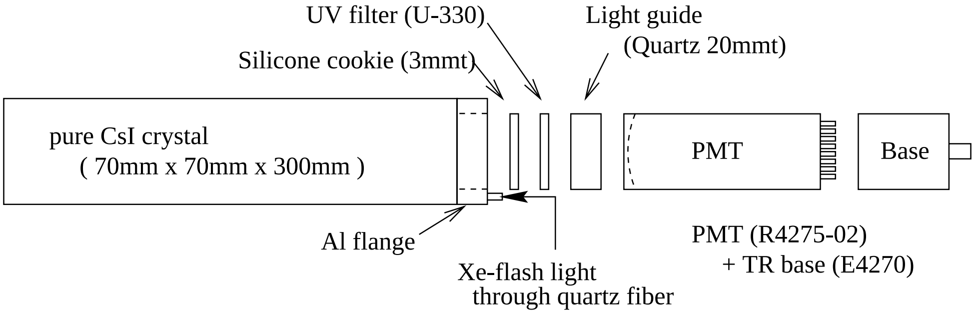

Figure 2.5: Schematic drawing of the calorimeter.

pile-up. This output, called column(row)-sum, was discriminated and then used in the level 1 trigger.

The energy and position resolutions were found to be about 3 % and 7 mm; the experimental procedure to determine these values will be described in next chapter.

2.2.3 Gas Cherenkov Counter

A 1.4m-long threshold gas Cherenkov counter (GC) was used to identify electrons. It was placed inside the gap of the analyzing magnet and filled with pure nitrogen at atmospheric pressure. It had 7(horizontal) × 2(vertical) optical cells, each consisted of a reflecting mirror, a light collecting funnel and a photomultiplier. Figure 2.6 shows the side view of GC sliced at X=0.

Since the emission spectrum of Cherenkov light obeys $1/\lambda^2$ distribution, where λ indicates its wavelength, we made efforts to detect ultra-violet lights (down to 160 nm), to achieve good efficiency for electrons.

A reflecting mirror was made of 2 mm-thick acrylic substrate, coated with aluminum (Al) and magnesium fluoride (MgF_2) by vacuum evaporation. It had parabolic shape to focus Cherenkov lights onto the PMT cathode. It was produced as follows. An acrylic sheet was heat-formed in an oven by pressing a substrate to a convex model made of wood. Then it was trimmed by a laser cutting machine into an appropriate size (300 mm×800 mm). Supporting ribs were glued onto its backside. After that, its front surface was coated with 1000Å Al and 400Å MgF_2 in a vacuum chamber (1.5×10^{-6}Torr). Reflectivity of the mirror was monitored by a small sample which was coated together, and was found to be 80 % or greater in the wavelength region between 160 nm to 200 nm and more than 85 % above 200 nm.

A light funnel was the Winston type light collector [15], equipped in front of a photomultiplier to increase the effective detecting area. It was press-formed from a 1.5 mm-thick aluminum plate. Its inside surface was coated with Al and MgF_2, same as above.

A 5″ photomultiplier (Hamamatsu R1251) was used to detect Cherenkov light. It has a quartz window to detect ultra-violet lights down to the wavelength of 160 nm. A gain of each photomultiplier was monitored throughout the experiment. Actually, it was carried out by observing a pulse height corresponding to single photo-electron emission, provoked by a green LED light.

To study performance of the counter, we used the $K_L \to \pi e \nu$ (K_{e3}) data which was taken by a special trigger; hit information from the gas Cherenkov counter was not used in any form in the trigger. Efficiency for e^+/e^- and pion rejection factor are shown in Figure 2.7 as a function of the threshold for light output, in units of ADC counts. For the actual trigger, we set the threshold level at about 30 ADC counts, where the pion rejection of 1/50 was achieved with the electron efficiency of 98%. In the offline stage, we could get better pion rejection

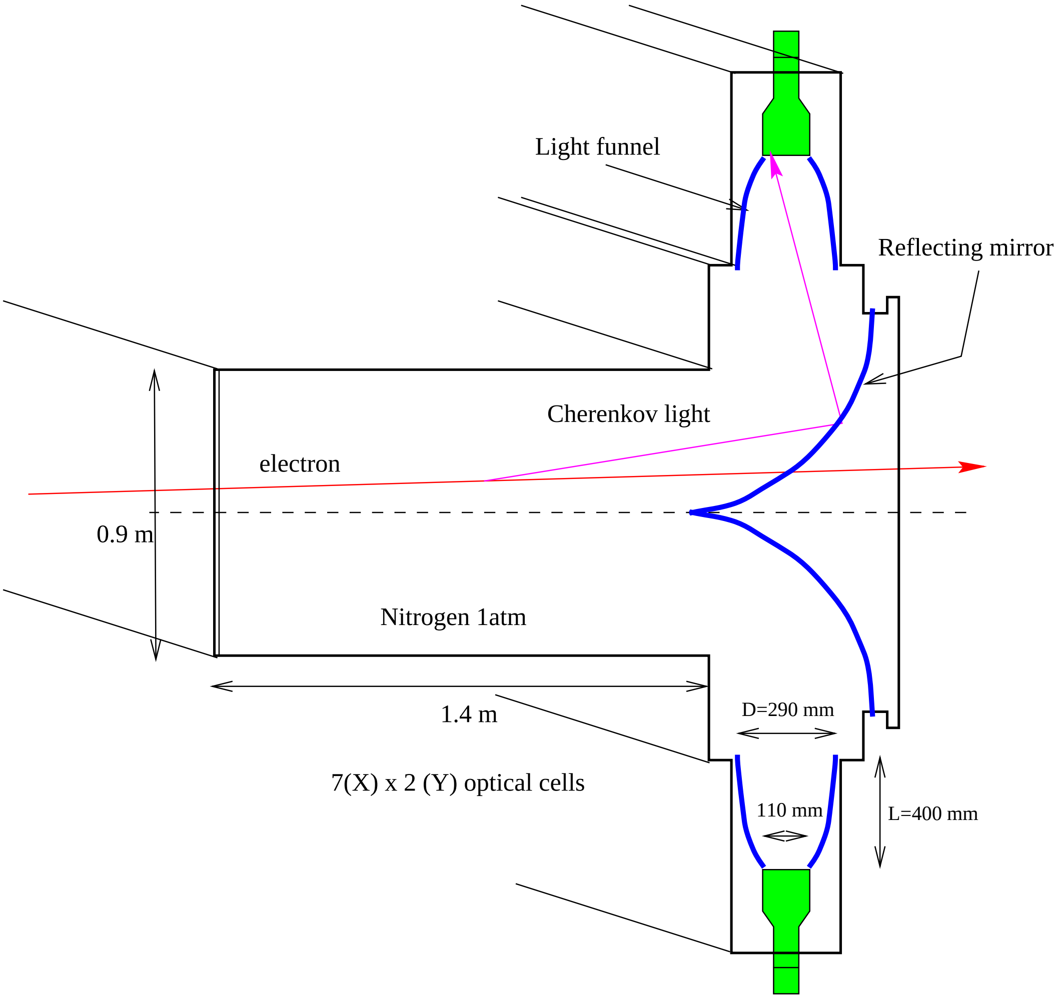

Figure 2.6: The side view of GC sliced at X=0. The arrangement of mirrors, light funnels and PMTs are shown in the figure.

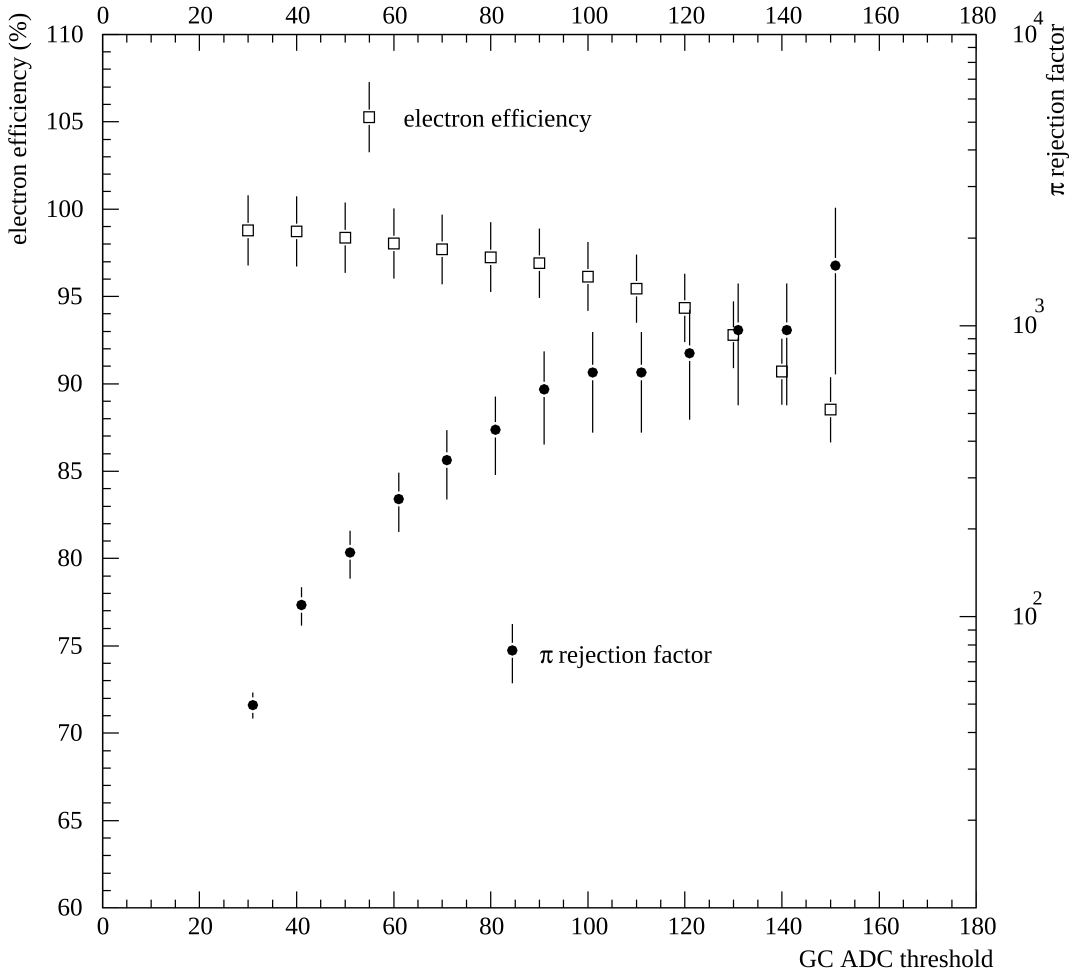

Figure 2.7: Efficiency for electrons and pion rejection factor of GC as a function of the threshold for light output. The threshold is represented in ADC counts of GC signal.

factor by raising the threshold value with slight loss of the electron efficiency, if necessary.[6]

2.2.4 Trigger Scintillation counters

There were four sets of trigger scintillation counters (see Fig.2.2), named TC0X, TC1X, TC2X/2Y and TC3X, where X(Y) represented a horizontally(vertically)-segmented hodoscope.

One set (TC0X) was located immediate downstream of the decay volume. Requirement of the hits in this counter enhanced the existence of charged particles coming from the decay volume. It reduced background events which were originated from photon conversions in the detector materials, both at the trigger stage and in the offline analysis.

It consisted of two layers of plastic scintillation counters, named TC0F and TC0R, which were placed 90 mm apart in the beam direction. Its active area included the neutral beam region to avoid the loss of acceptance. The dimensions of the individual counters were 900 mm in height and 1.5 mm in thickness. As for the width, there were two kinds, 25 mm and 50 mm. The narrow counters were placed inside/near the beam region to reduce counting rate of each counter. The arrangement of the counter is schematically shown in Fig.2.8. Each component was read by two 1-1/8″ photomultipliers (Hamamatsu R1398) from top and bottom end of a scintillator, equipped with transistorized base [16] and pre-amplifiers. Signals were processed by base-line restorers, discriminators. Then, coincidence was required between one TC0F counter and one of the two TC0R counters right behind it. Finally, a mean-timer module was used to produce a coincidence signal between the top and bottom ends of the scintillator. It reduced the timing jitter due to the variation of hit positions.

The other sets were located downstream of the analyzing magnet. Their dimensions were schematically shown in Fig.2.9–2.11. Each plane had a 300-mm-wide gap at the center for the neutral beam to pass through. TC1X and TC2X/Y were located in front of and behind drift chamber sets, respectively. TC1X(2X) consisted of 13(16) counters in each arm, with the thickness of 2.6(10) mm and the width of 45(35) mm for most inside two counters and 90(70) mm for others. TC2Y, segmented vertically, had 18 counters in each arm with the thickness of 10 mm and the width of 70 mm. TC3X was set immediate upstream of CsI calorimeter in its housing box. It was composed of 15 counters in each arm, with the thickness of 10 mm and the width of 70 mm. Each counter was read by a 2″ photomultiplier (Hamamatsu R329-02) equipped with a transistorized base (E4524) similar to the type for the calorimeter. Counters in horizontally-segmented hodoscopes were viewed from both top and bottom ends of scintillators, and those in vertically-segmented one (TC2Y) were viewed from one side,

---

[6] It was not done in the analysis for the mode described in this thesis.

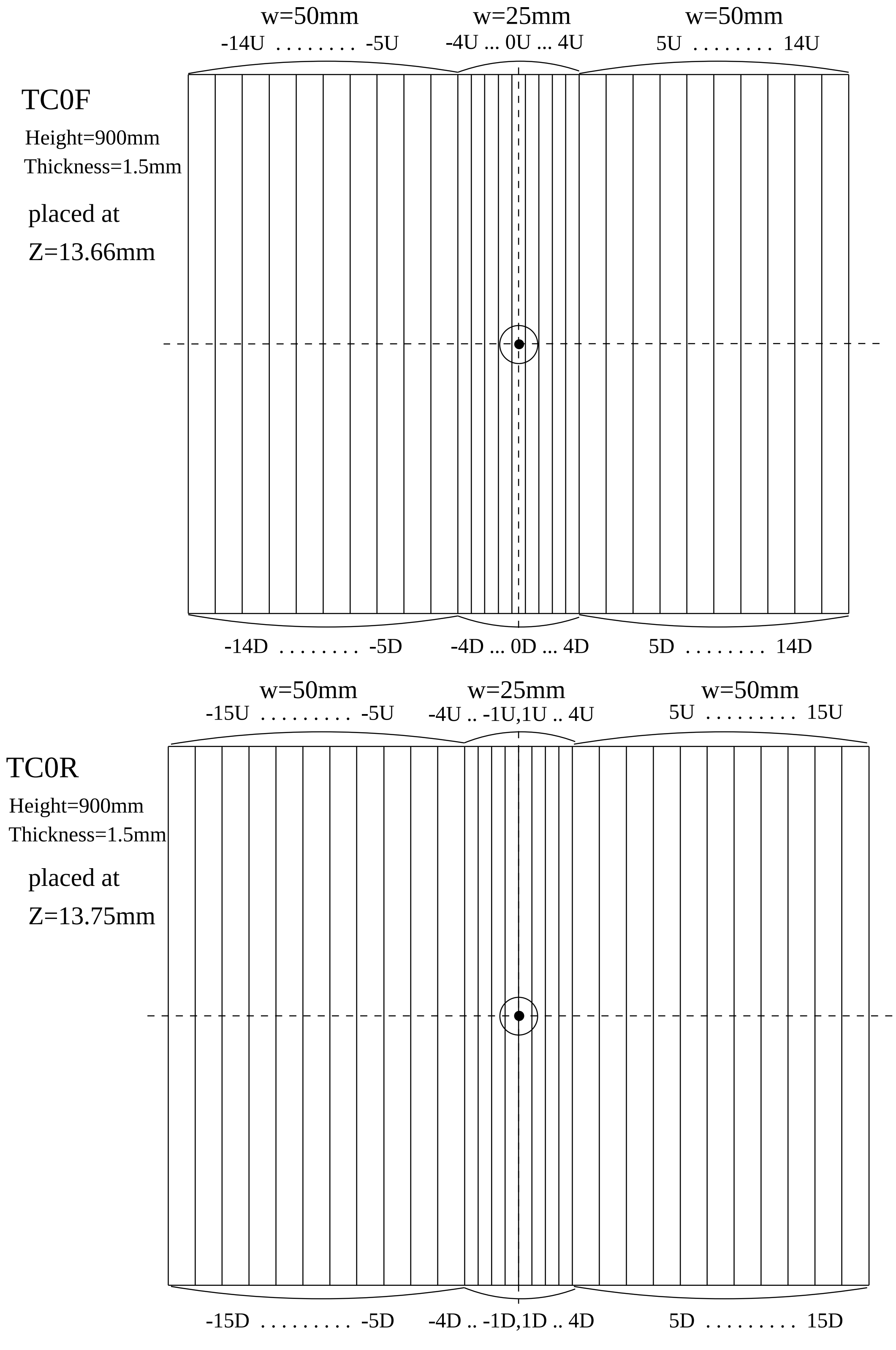

Figure 2.8: The trigger counter plane TC0X. It consisted of two layers: TC0F and TC0R, and its active area included the beam region.

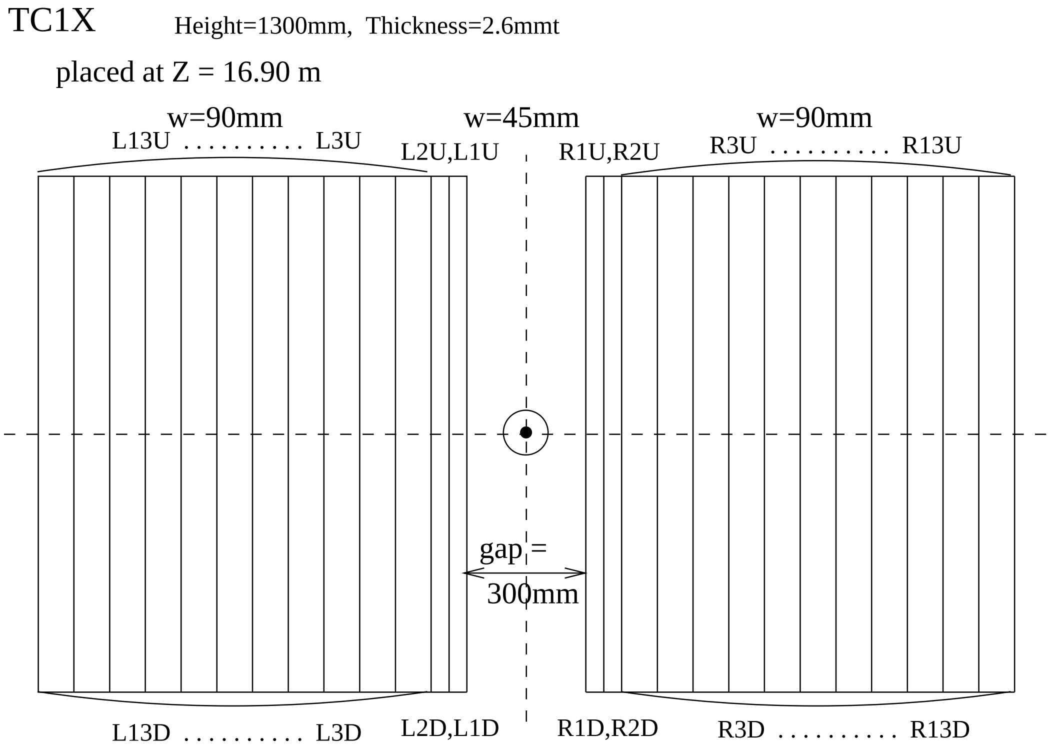

Figure 2.9: The trigger counter plane TC1X.

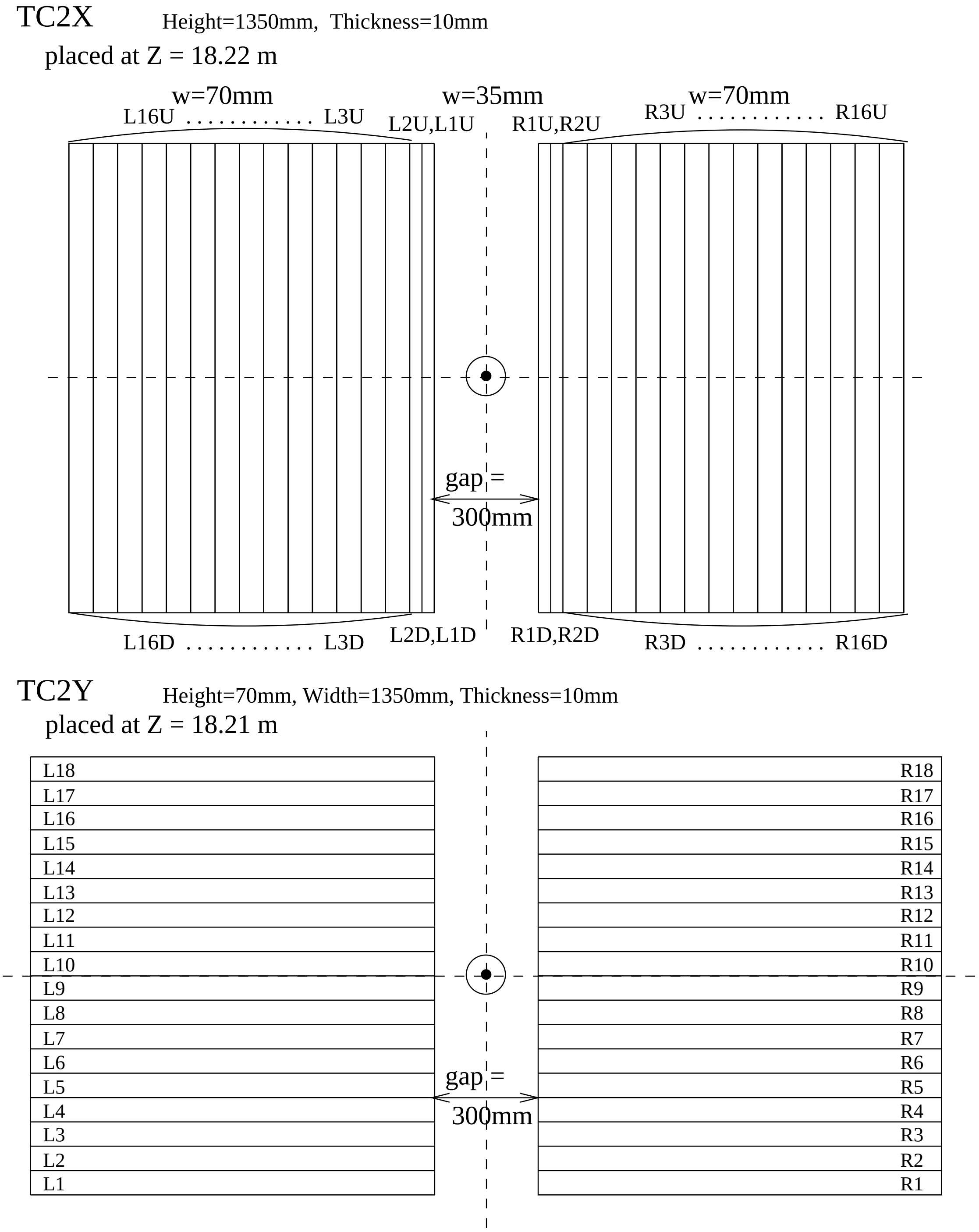

Figure 2.10: The trigger counter plane TC2X and 2Y.

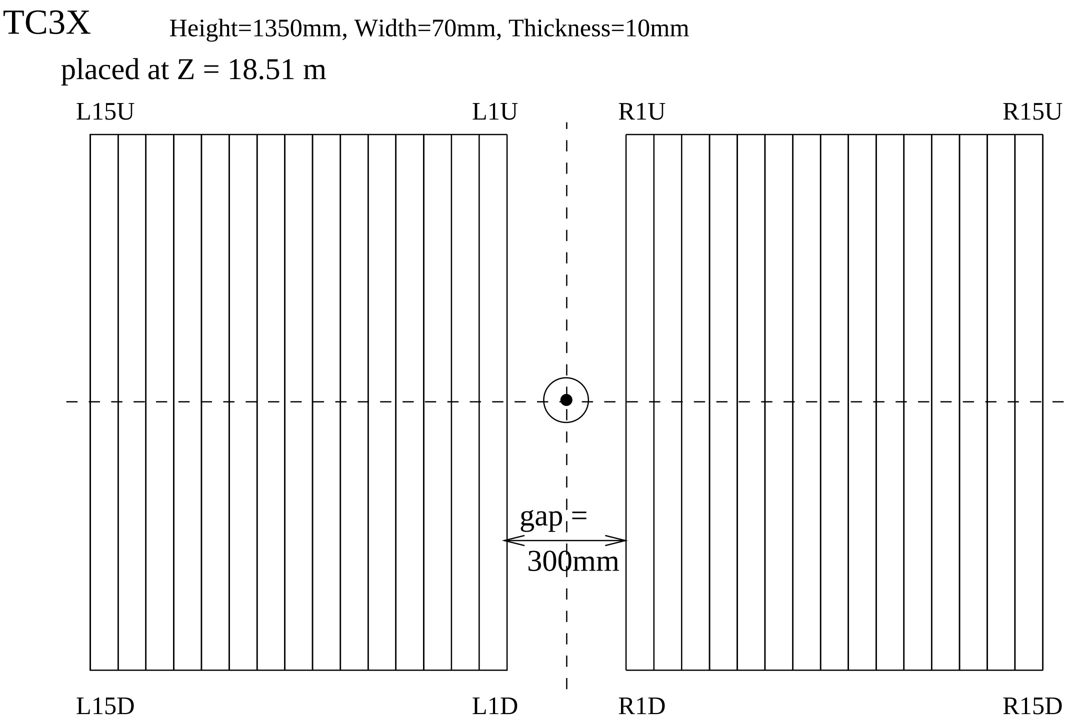

Figure 2.11: The trigger counter plane TC3X. It was placed in the housing box of the calorimeter.

Table 2.1: List of trigger modes for physics and calibration.

Trigger mode		Target
Physics	Trig.0	$K_L \to \pi^0 e^+ e^-$ $K_L \to e^+ e^- \gamma$
	Trig.1	$K_L \to \pi^+ \pi^- \pi^0$
	Trig.2	$K_L \to e^+ e^- e^+ e^-$
	Trig.3	$K_L \to \pi^+ \pi^- e^+ e^-$
Calibration	Trig.4	random trigger [a]
	Trig.5	energy calibration (K_{e3}) GC efficiency (K_{e3}) TC0/DC efficiency (no magnetic field)
	Trig.6	pedestal run GC LED run
	Trig.7	Xe flash lamp

[a] created by the coincidence of unrelated two counters.

opposite to the beam region. Signals were discriminated in the counting room and were used to make up trigger information.

2.3 Trigger

The trigger system in this experiment was designed to take data for various K_L decay modes simultaneously. There were four types of trigger logic for physics modes (Trig.0,1,2,3), one type to study beam-associated backgrounds (Trig.4), and three types for calibrations of detectors and electronics (Trig.5,6,7), listed in Table.2.1. Each logic for physics modes was composed of two levels. The level 1 trigger was produced by fast NIM logics within 100 nsec of particle passage through the detector. The level 2 trigger was made by a set of hardware processors within 10 μsec.

The information used at the level 1 was the number of counter hits and their coincidences. The logical requirements imposed on the counter hits at the level 1 are listed in Table 2.2. A logic "TC23" in the table denotes the coincidence of one counter in TC2X with immediate downstream counters (three or four counters) in TC3X. A logic "TC0" represents the coincidence of one counter in TC0F and one of the two counters right behind it in TC0R. A logic "CSIX(Y)" is a discriminated signal of column(row)-sum, described in Section 2.2.2, with the threshold voltage equivalent to 300 MeV.

Once one of the level 1 logics was satisfied, gate signals were provided into ADCs, TDCs and processors in the level 2 logic.

Table 2.2: List of hit requirements at the level 1.

Source	Trigger mode			
	Trig.0	Trig.1	Trig.2	Trig.3
N(TC23)[1]	≥ 2	≥ 2	≥ 3	≥ 3
N(TC0X)	≥ 2	≥ 2	≥ 2	≥ 3
N(TC1X)	≥ 1	≥ 1	≥ 2 [a]	≥ 2 [a]
N(TC2Y)	≥ 1	≥ 1	≥ 2 [a]	≥ 2 [a]
N(GC)	≥ 2	-	≥ 2	≥ 3
N(CSIX)[2]	≥ 3 [a]	≥ 2 [a]	≥ 3 [a]	≥ 2 [a]
N(CSIY)[3]	≥ 3 [a]	≥ 2 [a]	≥ 3 [a]	≥ 2 [a]

[1] Number of the coincidence signal between TC2X and TC3X. See the text for detail.

[2] Number of the column-sum hits in the calorimeter.

[3] Number of the row-sum hits in the calorimeter.

[a] At least 1 in both arm.

The level 2 trigger had two objects. One was to count the number of track candidates; this task was done by a coarse tracking processor (CTP), by looking for the correlated hits in downstream trigger hodoscopes. The other was to search for clusters on the calorimeter; it was done by a cluster finding processor (CFP), using the hit positions of the CsI blocks.

The CTP was composed of a sequencer part and a lookup memory in which possible track patterns had been pre-recorded. There were four CTPs, two for left arm and two for right arm. Modules in one arm had different patterns for positive and negative charged tracks. A track to be searched was defined as specific combinations of TC1X, TC2X and TC3X. The CTP also searched electron candidates among the found tracks, by matching the hit pattern in GC and CSIX. Each module produced an encoded output, containing the number of charged tracks and the number of electrons. The information was sent to the decision modules, which will be described below.

The CFP consisted of 16 modules (8 for each arm) and a sequence controller. Each module received analog signals of CsI blocks from two adjacent columns. It then discriminated them with a threshold equivalent to 250 MeV, which was determined to be higher than the energy deposit of a minimum ionizing particle. The information of hits was latched and converted to a bit pattern. Then the modules tried to find clusters by matching the actual hit pattern with prescribed patterns. The pattern recognition was carried out sequentially from the bottom row to the top row under the instruction of the controller. Using the information of hits in TC3X and TC2Y, the modules also examined whether or not the found cluster was associated with a charged particle. Since the threshold was set higher

Table 2.3: Logics in the level 2 trigger

Logic		Trigger mode			
		Trig.0	Trig.1	Trig.2	Trig.3
N(tracks)[1]	by CTP	$(\geq 2)^{\mathrm{a}}$	$\geq 2^{\mathrm{b}}$	$(\geq 3)^{\mathrm{a}}$	≥ 3
N(clusters)[2]	by CFP	≥ 3	$\geq 2^{\mathrm{b}}$	≥ 3	$\geq 2^{\mathrm{b}}$
N(e-TRK)[3]	by CTP and CFP	≥ 2	–	≥ 3	$\geq 2^{\mathrm{b}}$

[1] Number of charged track candidates.

[2] Number of clusters in the calorimeter.

[3] Number of electron candidates.

[a] Effective constraint through the requirement of N(e-TRK).

[b] ≥ 1 in both arm.

than the energy deposit by minimum ionizing particles, the cluster associated with a charged particle was considered as an electron cluster. After the finding sequence, the number of clusters and that of electron clusters in each arm were sent to corresponding decision modules.

Two decision modules with XILINX XC3190 logic cell arrays (XLP/XRP) received the information from the CTP and the CFP system. Their task was to distinguish electron candidates (e-TRK) more exactly by combining track and cluster information.

Finally, a master decision module (XDM), which was the same module as XLP/XRP but loaded different logic program, produced “accept” signals for various trigger types. Trigger logics for four physics modes were summarized in Table 2.3.

If no accept signal was asserted within 10 μsec from the gate signal by the level 1 trigger, conversion processes in ADCs and TDCs were stopped and the event was discarded.

The trigger rates under a typical running condition were summarized in Table 2.4. The dead time was about 10% and 30% at the level 1 and 2, respectively.

2.4 Data Acquisition

If an event was accepted by one of the trigger modes, the information from detectors was read out and recorded by the data acquisition (DAQ) system. Contents of the recorded data, which included digitized data from ADCs and TDCs, latched hit patterns of hodoscope planes, are summarized in Table 2.5.

The composition of DAQ system is shown schematically in Figure.2.12. A

Table 2.4: Trigger rates at each stage.

Stage	Trigger rate (counts/spill)						
	Trig.0	Trig.1	Trig.2	Trig.3	Trig.4	Trig.7	total
At the level 1	2.6K	30K	230	640	50	40	2.2K
Prescale	1/3	1/80	1/1	1/1	-	-	
After the level 2	450	230	100	300	50	40	1000 [a]

[a] Since an event was counted in several modes, total rate was not the sum of rates of individual mode.

sequence of data processing is described below.[7]

At first, when an event was accepted by the level 1 trigger, front-end electronics modules began processing the information from various detectors. The most of the front-end modules were controlled on the basis of TKO standard which had been developed at KEK [18]. Analog signals from CsI blocks were digitized by charge-sensitive ADCs with 110-nsec-wide gate. Discriminated signals from drift chambers were processed by 1GHz pipelined TDCs. Discriminated signals from hodoscopes were latched with 60-nsec-wide gate by strobed coincidence (SC) modules, and then digitized by TDCs.

Each front-end module in TKO boxes performed three steps of data processing: sample-and-hold, digitization, and readout. If these processes were executed in series, modules had been busy for a long time. To avoid this type of dead time in data processing, we adopted a pipeline operation between these stages. Once a gate signal was received, a module started the sample-and-hold and the digitization process. The digitized data were transfered to a register where they were held until the readout cycle. After the transfer, the sample-and-hold part of the module became free to process the next event even before the readout process for the previous data. This parallel processing reduced the dead time substantially.

If an accept signal by the level 2 trigger was asserted, a controller (SCH) in each TKO crate scanned modules sequentially and examined whether or not data existed in the registers. If existed, digitized data were read out by SCH and transfered to a corresponding memory module (MP) in a VME crate through a twisted flat cable. Data had been stored in the MPs during one beam extraction cycle.

After a beam extraction period, all the data in the MPs were transfered into memories on CPU boards via the VME bus.[8] The role of these CPUs was to build up the event data. The event-building task was shared by three CPUs

---

[7] Detailed description can be found in Ref.[17].

[8] One CPU was operated on OS-9 68020 system (CPU-B in the figure) that is a real-time operating system for Motorola 68000 family. Other CPUs including master event-builder (CPU-M) had SPARC architecture and worked on SunOS.

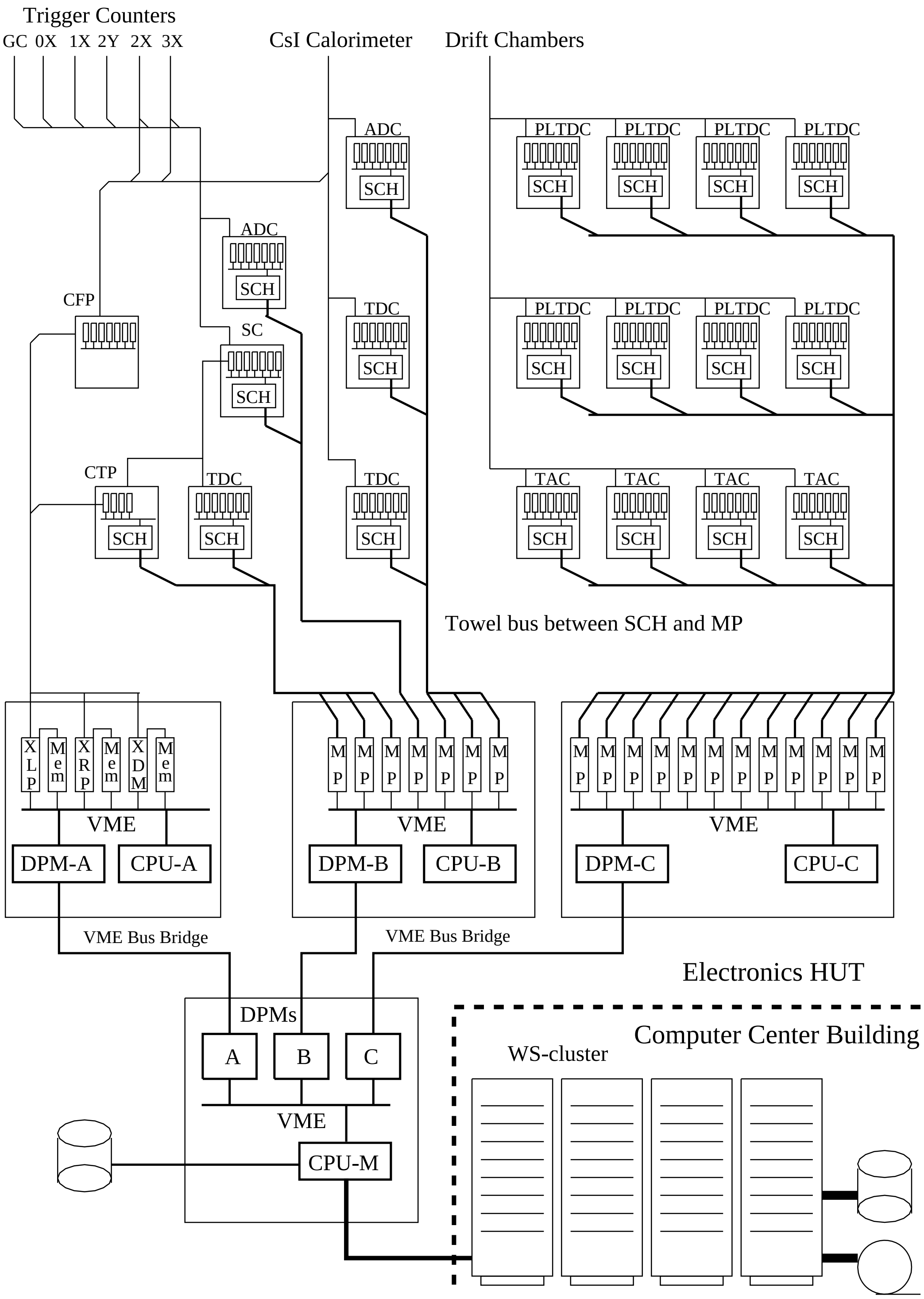

Figure 2.12: The composition of DAQ system in E162 experiment.

Table 2.5: The contents of data. There were digitized data from ADCs and TDCs, latched hit patterns of hodoscope planes, and so on.

Source		Sort
Detectors	TC0X	SC[a],PLTDC[b]
	TC1X	SC,TDC
	TC2X/Y	SC,TDC,ADC[c]
	TC3	SC,TDC,ADC[c]
	GC	SC,TDC,ADC
	calorimeter	TDC,ADC
	drift chamber	TAC (DC3U/V,DC4U/V) PLTDC (others)
Logic	TC23	SC,TDC
	CSIX/Y	SC,TDC
Trigger info.	CTP	track info. (encoded)
	CFP	block hit pattern (latched) cluster info. (encoded)
Scaler	beam condition	spill count, clock target monitor (TM) intensitiy monitor (SEC)
	live-time monitor	w/ and w/o BUSY [d]

[a] The latched information by the strobed coincidence module.

[b] Of individual PMTs (TC0F:U/D,TC0R:U/D) and of logic "TC0X".

[c] Of individual PMTs (TC2X:U/D,TC3X:U/D).

[d] BUSY signal was asserted by trigger control module.

(CPU-A/B/C) to speed up processing at the first stage. Then the data built by each CPU were sent to another CPU (CPU-M) via dual port memories, and were integrated by a master event-builder.

After the event-building procedure was finished, integrated data were transfered to a local disk for quick analysis, to a local DAT via a SCSI bus, and also to the workstation cluster via FDDI LAN for main analysis.

Chapter 3

Computing of Physical Quantities

In this chapter, basic methods to compute physical quantities, such as trajectory of a charged track, its momentum, hit position and energy of photons, and decay vertex, are described.

3.1 Reconstruction of Charged Tracks

Reconstruction of charged particle tracks was done using hit position information from drift chambers. At first, local pattern recognition in each drift chamber was performed. Next, they were combined each other to form a track. Then, track parameters were evaluated by track fitting. In the following, these procedure will be explained in detail including the drift chamber calibration.

3.1.1 Calibration of Drift Chambers

In order to evaluate track positions, we must know precise relationship between drift time and drift length (R-t relation), as well as precise position of chambers in the detector coordinate.

Before the calibration of R-t relation, we first determined TDC counts corresponding to zero drift time ($T0$) of each wire. Figure 3.1(a) shows a typical example of a TDC distribution. The distribution shows sharp rise near $T0$. Extrapolating the tangent of this edge, we defined $T0$ as the position to cross with the base line.

We employed the following method to establish the R-t relation. Hit time distribution of a drift chamber can be represented by

$$\frac{dN}{dt} = \frac{dN}{dR} \times \frac{dR}{dt} , \tag{3.1}$$

where N denotes the number of events and R denotes the minimum distance from a wire to a track. Suppose distribution of track positions in a cell is uniform,

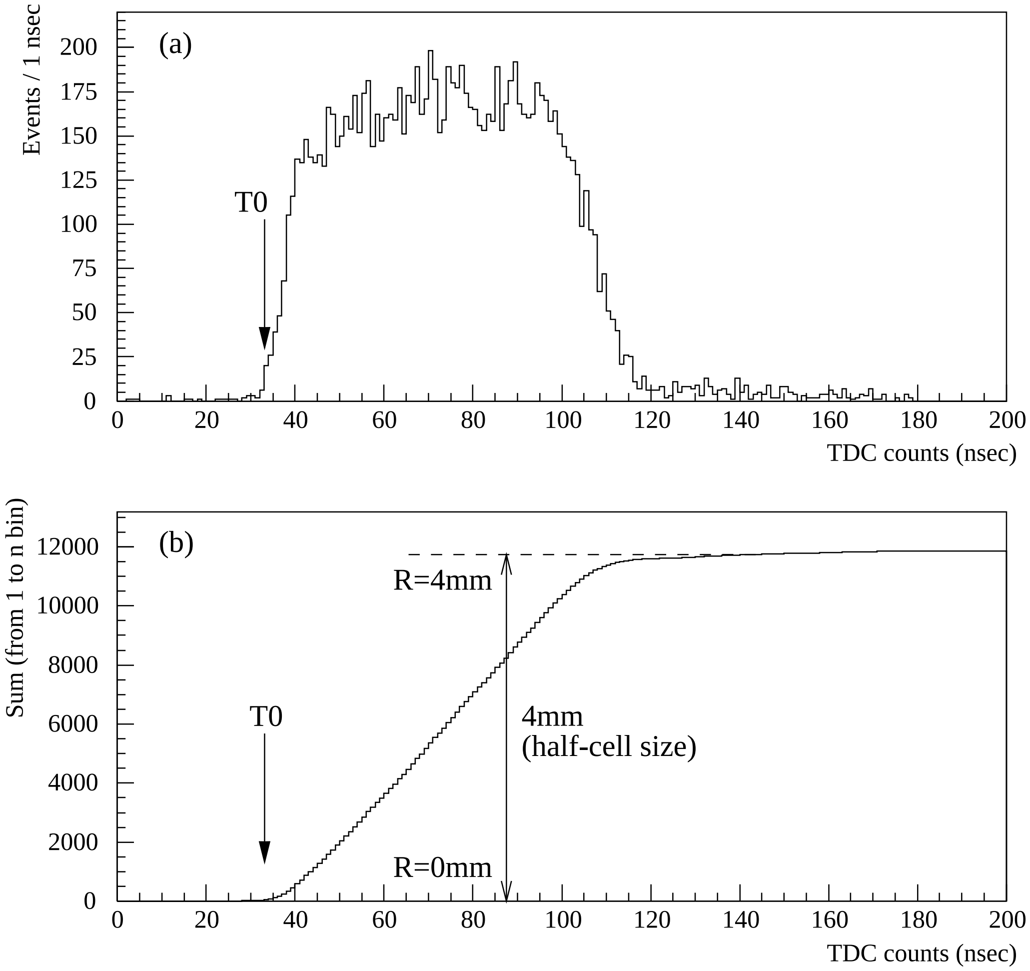

Figure 3.1: (a) A typical TDC distribution of drift chamber and (b) its integrated distribution. Actually, TDC data of all wires in DC3X were used in these samples.

i.e. $dN/dR = C$(=constant). The assumption was met very well for our drift chambers if tracks passing normal to the chamber plane were selected. Integrating over both sides of Eqn.(3.1), we get

$$\int_{T0}^{T} \frac{dN}{dt} dt = C \times [R(T) - R(T0)] = C \times R(T) \ , \tag{3.2}$$

where $R(T0)$ equals to zero as a definition. Fig.3.1(b) shows an example of the integrated distribution as a function of T i.e. the left hand side of Eqn.(3.2). The variable C was set so that the maximum value of $R(T)$ was equal to be a half cell size (4 mm), corresponding to the place where the distributions levels off. The curve in Fig.3.1(b) now enabled to relate T and $R(T)$.

After installing all detectors including drift chambers, we positioned them with levels and optical transit instruments. These measurements were performed with a nominal accuracy of 1 mm. However, more precise wire positions must be known to realize a good momentum resolution as a spectrometer. Determination of wire positions, down to the level of the chamber position resolution itself, was carried out with real track data in the following way.

We started to determine relative positions among the chambers. The calibration data were taken with the analyzing magnet being turned off. At first, we assumed that most upstream and downstream chambers (i.e. DC1X and DC4X) were set at the correct position. We calculated the hit position distribution of DC2X and DC3X for the straight track. If the distribution showed any offsets relative to the axis defined by DC1X and DC4X, then the chamber position of DC2X and/or DC3X was adjusted. In the case of U/V-view chambers, projected positions onto the X-axis were calculated by combining DC1U with 1V, 2U with 2V, and so on, and then offset values were adjusted. Note that over all positions of chamber coordinates were still arbitrary in this procedure.

The absolute coordinates in this experiment was defined by the target position and the calorimeter position. The target position was defined as an origin. Two sets of data were used to adjust the chamber coordinates to the absolute coordinates. One was the data for energy calibration of the calorimeter, involving mainly K_{e3}. By comparing positions of electrons determined by the chambers with cluster positions (see Section 3.3.2), offsets of the chamber coordinate system to the absolute position were obtained. The other was the events which were reconstructed as $K_L \to \pi^+\pi^-\pi^0$. The mean position of kaons at the target, calculated by extrapolating reconstructed directions, should be zero. Using these data set, we adjusted the offset and the direction of the chamber coordinates to be conformed with the absolute coordinates.

3.1.2 Tracking

In our spectrometer system, a track was approximately straight in both upstream and downstream of the magnet and it was bent horizontally by the magnetic field.

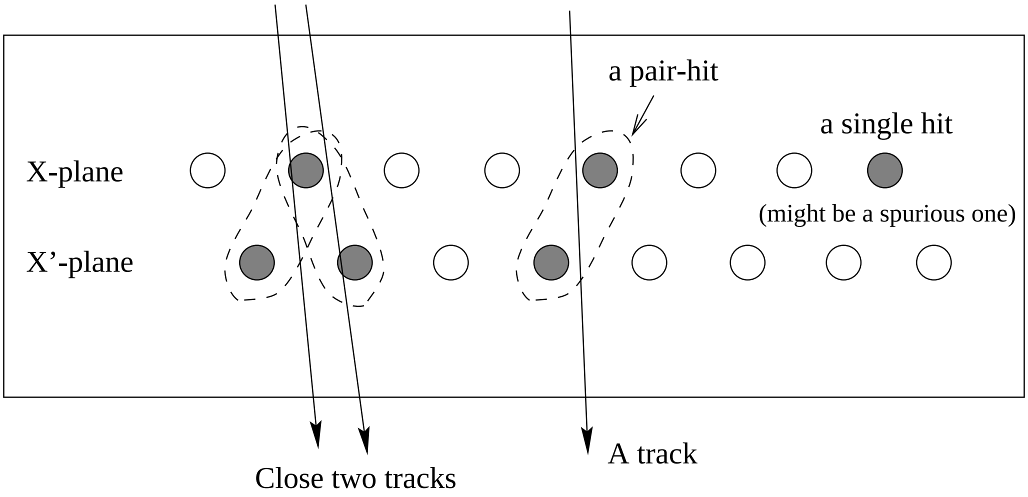

Figure 3.2: Schematic explanation of pair hit

The procedure we had to do was to reconstruct straight tracks separately in both sides of the magnet, and to match with each other.

As described in previous chapter, a drift chamber consisted of two planes staggered by a half-cell, which were called, for example, X- and X′-plane. If a track passed through a chamber, there should be a hit in both planes. We considered one hit as a "real" hit when a corresponding hit was found on the other plane, otherwise it was assumed to be a spurious hit. This procedure that we called pair-hit search is schematically shown in Figure 3.2. A hit time had to be within a window, from T0-10ns to T0+120ns, whose width was determined by the drift time corresponding to a half cell size with a margin. Also note that we used a first hit within the window if there were plural hits on one wire. If there were two adjacent hits in one plane and only one in the other, as shown in Fig.3.2, we considered them as two pair-hits at this stage, though they might belong to one track.

Among many hits in drift chamber planes, a set of pair-hits belonging to a single track had to be selected out. We started this task with the downstream X-view chambers (DC3X,4X) due to two reasons. One was that there were in general fewer hits than in upstream chambers because background particles with low momentum were swept out by the analyzing magnet. The other was that they were sandwiched between two trigger hodoscopes (TC1X and TC2X). Requirement of hits at these hodoscopes drastically reduced possible track candidates. Practically, we first determined a "road", which was a band spanned by a pair of the hits in TC1X and TC2X,[1] as shown schematically in Fig.3.3(a). Hit wires

---

[1] Since we allowed tracks to pass through the central gap of TC1X, we treated the beam hole of TC1X as a counter which was always fired in the tracking procedure.

outside these roads were masked off and were put aside from the analysis.

Once we selected a set of pair-hits, an approximate incident angle of the track could be determined. Then we defined a quantity named $ADEF$:

$$ADEF = \left[(-1)^i \cdot \frac{R}{\cos\theta} + (-1)^j \cdot \frac{R'}{\cos\theta} + \Delta Z \cdot \tan\theta\right] - (\text{the half cell size})\ , \tag{3.3}$$

as illustrated in Figure 3.4. Here, R and R' denote the drift length of the hits in each plane, ΔZ represents the gap between planes (8 mm), and θ is an incident angle of the track. The exponents i and j represents left ($i = 1$ or $j = 1$) and right ($i = 0$ or $j = 0$) side of the wire. Let's consider, for simplicity, a pair-hit marked by a track incident normal to the X- and X$'$-planes ($\theta = 0$). For these hits, the sum of the drift distances should add up to the half cell size (i.e. 4 mm). The quantity $ADEF$ was defined as a deviation of the sum of distances from the half cell size. In reality, there were two facts which changed the simple situation above; tracks incident with an angle and the left-right ambiguity of hit positions. The former was corrected according to Eqn.(3.3). For the latter, $ADEF$ values were calculated for all possible combinations of i and j. Figure 3.5 shows an example of $ADEF$ distribution. We chose the left-right combination with a minimum $ADEF$ value. Also $ADEF$ was required to be less than 4 mm.[2] With the combination determined above, track parameters in X-Z plane were calculated by fitting to a line, represented by $X = aZ + b$. Resultant reduced χ^2 in the fit was required to be less than 500, which was quite loose cut. For those passed the cut, the track parameters were retained for further analysis.

The procedure of track finding in upstream X-view chambers was same as that in downstream chambers except for definition of a road. At first, we calculated the X position extrapolated from a downstream track candidate determined above to the magnet center. Then the road was defined as a sector spanned by the beam region in the decay volume from the X position, as shown in Fig.3.3(b). The existence of corresponding TC0X hit was also checked. We performed the same procedure as before to get the track parameters. With the track candidates both in upstream and downstream of the magnet we calculated the difference in X positions of the two extrapolated to the magnet center. The difference was called $DXMAG$, and was required to be within ±20 mm.

Then, track finding in upstream U- and V-view chambers followed. Since we had no device to define a road in those views, all combinations of hits were examined. The only requirement was that a track had to come from, or pass through the beam region in the decay volume. We determined all the track candidates for both U-Z and V-Z planes, and then combined them one by one. A good track had to meet following two conditions. One was the condition about extrapolated Y positions of the track at various locations. It had to pass through the magnet aperture, to fire one of TC2Y, and to go into the calorimeter. The

---

[2] As can be seen in Fig.3.5, this requirement amounted to be very loose.

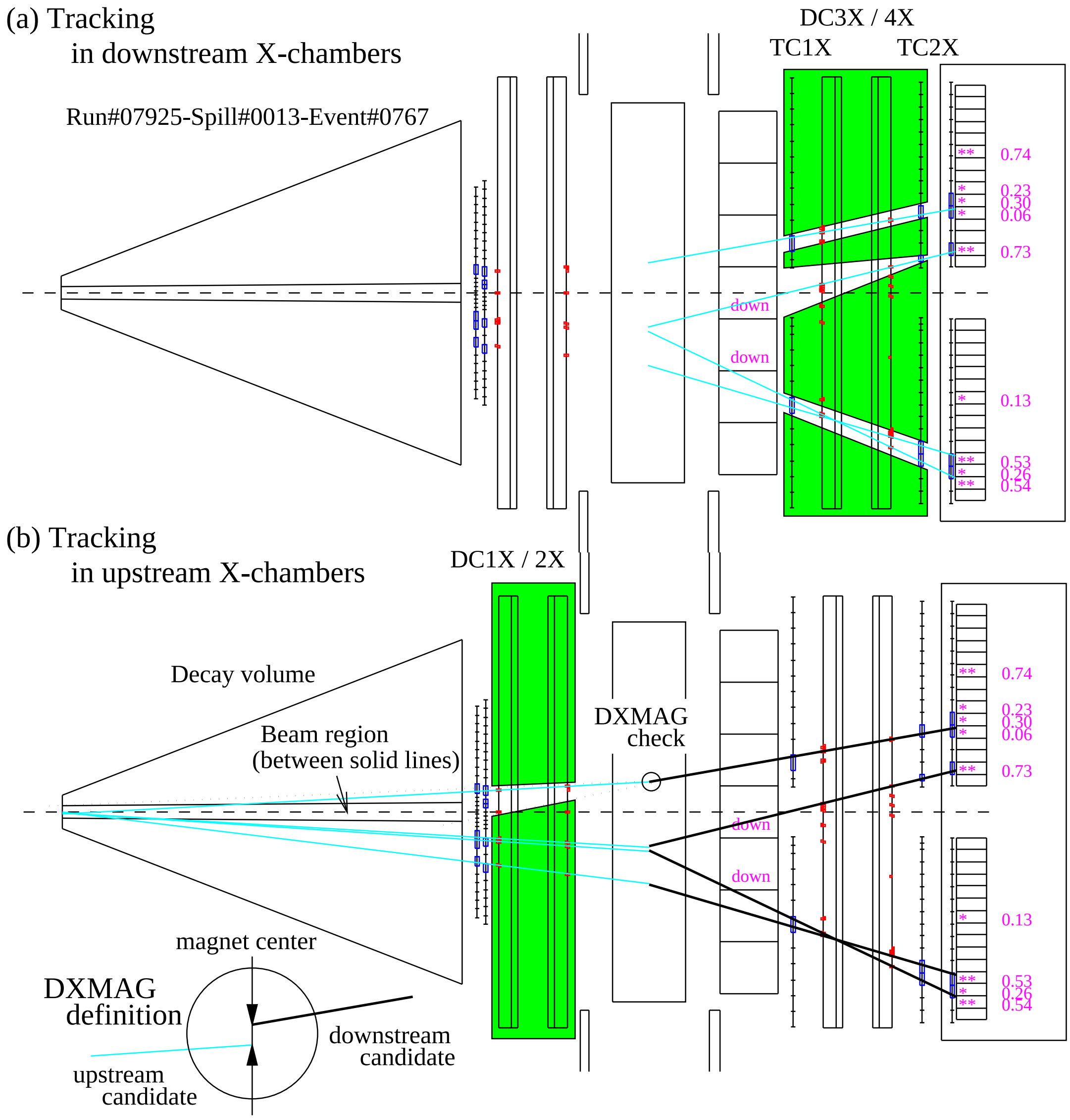

Figure 3.3: Schematic explanation of tracking procedure in X-view chambers. (a) Track finding in downstream X-view chamber. Hits in TC1X and TC2X defined roads, shown as unshaded area. Four track candidates were found in this example. (b) Track finding in upstream X-view chamber. A road was defined by the information of downstream track candidates and the beam region in the decay volume. One of roads is schematically shown as unshaded area. Consistency of the upstream and downstream track candidates was represented by a quantity $DXMAG$, which was the distance between the two at the center of the magnet.

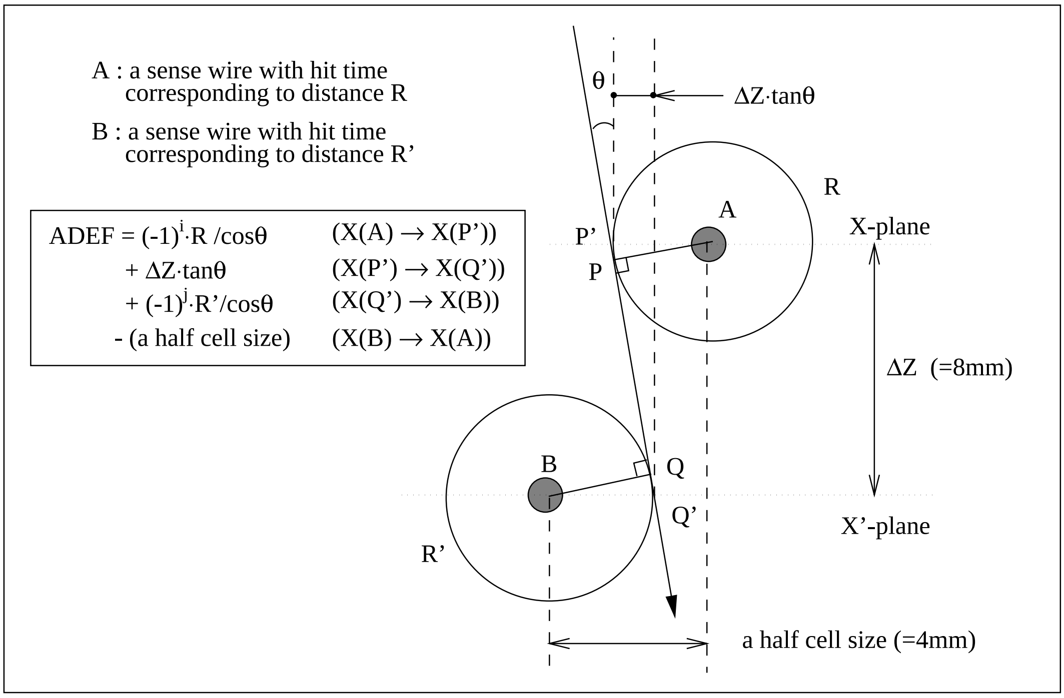

Figure 3.4: Sum of distances corrected by incident angle of a track. *ADEF* was defined as its deviation from a half cell size.

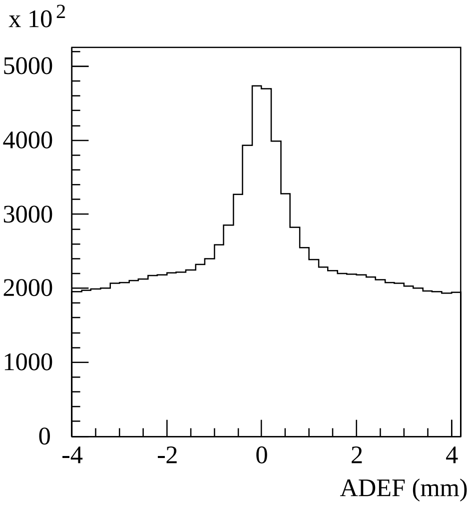

Figure 3.5: An example of *ADEF* distribution. Since *ADEF* values calculated for all possible combinations, there exists a flat background from many incorrect combinations below a narrow peak at $ADEF = 0$.

other was that the trajectory projected onto the X-Z plane had to be consistent with one of the track candidates formed with DC1X and DC2X. It was checked by comparing calculated X positions at DC1X and DC2X; differences between them were required to lie within 2 mm. Using the hit wires in X/U/V-view chambers belonging to one track candidate, re-fitting to a straight line was performed, not in a plane but in a space.

To establish correspondence between upstream and downstream candidates, we first sorted all possible combinations in order of the magnitude of $DXMAG$. We started the matching with the combination that had the smallest $DXMAG$. If the corresponding hit in TC2Y existed in the expected arm, the combination was adopted as a continuous track from upstream to downstream of the magnet. If either upstream or downstream candidate was already used in the adopted tracks, the combination was discarded. This procedure was repeated for all combinations. Now, we established a set of tracks, continuous from upstream to downstream of the magnet; they were the basis for momentum measurement and particle identification, etc.

3.2 Momentum Analysis for Charged Particles

After the track reconstruction described in previous section, the momentum calculation of charged tracks was performed. In this analysis, we used an effective field approximation. We assumed a uniform magnetic field inside the magnet gap. The momentum of a charged particle is represented in the form,

$$p = 0.3qBR/\cos\lambda \ , \tag{3.4}$$

where p is a momentum in GeV/c, q is the charge of the track, B is the field strength in Tesla, R is radius of curvature in meter and λ is pitch angle.

The effective field B was determined in the following way. Prior to the experiment, we measured actual magnetic fields inside and outside the magnet gap. Given particle's momentum and incident trajectory, we traced it with the actual magnetic field.[3] We could now calculate the radius R from the kick angle between upstream and downstream track directions. With R and p (and λ), we determined a value for B from Eqn.(3.4). We averaged such B's over many trajectories and momenta generated by a Monte Carlo simulation for the $K_L \rightarrow \pi^+\pi^-\pi^0$ decay.

Having determined the effective B, we could calculate momentum p for each track. The pitch angle of upstream track was adopted as λ.

The momentum resolution was affected by position resolutions of chambers, multiple scattering, and also the precision of the effective field approximation. Figure 3.6 shows the momentum resolution as a function of track momentum. Results in the figure were obtained by the Monte Carlo simulation, in which

---

[3] Actually, a Runge-Kutta method was employed to trace them.

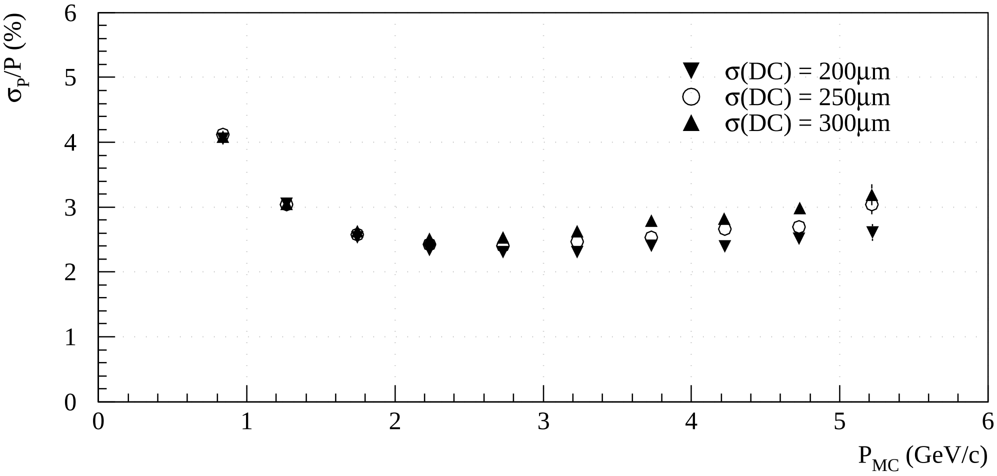

Figure 3.6: Momentum resolution as a function of track momentum. It was obtained by Monte Carlo simulation. Three symbols show the result from cases with different position resolution of drift chambers set in the simulation.

the resolution of chambers were set to be 200, 250 and 300 μm, respectively. We considered that poor resolution in low momentum region was caused by the inaccuracy of the effective field approximation. The influence of the chamber position resolution on momentum resolution is found not large, although a slight deterioration can be seen in the high momentum region. It suggests that the decline of the position resolution in the beam region might cause the drop of the momentum resolution up to about 0.2% at 4 GeV/c.

3.3 Calorimetry

The energy and position of electrons and photons were measured by electromagnetic calorimeter, which was composed of CsI scintillation crystals. The light output of each crystal, read by a photomultiplier and recorded as ADC counts, was proportional to the energy deposit by a particle. An electron or photon incident on a crystal caused an electromagnetic shower and deposited almost all energy to crystals around the incident position. In order to get their energies, we had to know, at first, the coefficients to convert an ADC count to a energy, which are called "calibration constant" below. We also had to identify a group of crystals, called "cluster", which belonged to a passage of one particle. These were realized by the energy calibration and the cluster finding procedures presented in this section. The position measurement of electromagnetic particles was also done using the cluster information. The method was checked by electron tracks, whose position could be measured both by the calorimeter and by drift chambers.

3.3.1 Energy Calibration

Before any precise calibration of the calorimeter, the gain of photomultipliers were adjusted so as to get uniform pulse height to the same energy deposit. Actually, the number we made uniform was the ADC count to the passage by a minimum ionizing particle such as a muon and a pion. The deviation of each photomultiplier gain was adjusted within ±10% at the beginning of the entire experiment.

The gain change, for example, due to the decrease of scintillation lights, which was caused mainly by the radiation damage, was treated by the precise energy calibration. It was performed using electron tracks in the $K_L \to \pi e \nu$ decay (K_{e3}). To obtain enriched K_{e3} events, we prepared a special trigger which required two tracks, one in each arm, with a vertex in the decay volume, and Cherenkov counter hits corresponding to one of the two tracks. The momentum of the electron and its incident position on the calorimeter were obtained by the spectrometer, as described in the previous section. At first, we chose one block to be calibrated. we requested this block to have more than 60% of the summed energy which included energy deposits in the surrounding 8 blocks. We note here that energy leakage from 9 blocks was found to be negligibly small according to shower simulation based on the GEANT Monte Carlo package [19]. In case of the peripheral blocks, additional cuts on the incident position were imposed to avoid the influence of shower leakage. Now, the ratio of the summed energy (E) to the momentum (p) measured by the spectrometer was defined as E/p. Since electrons lost its all energy in the calorimeter by creating a shower, E/p should be unity within the resolution. We fitted the E/p distribution to the Gaussian shape and adjusted the calibration constant of the target block so that the mean of E/p became one. We applied this process to all blocks and then repeated this entire procedure again with new constants. After third attempt, changes in the calibration constants were found to be within 1%, thus the process was terminated after the second iteration. Figure 3.7 shows an E/p distribution of all blocks into one histogram. The resolution of E/p was found to be about 3 % over all blocks.[4]

3.3.2 Cluster Finding

The method of the cluster finding we adopted was to find a block which contained larger energy deposit than any of the surrounding blocks. Figure 3.8(a) shows the schematics of the cluster finding procedure. When such a block had an energy of 10 MeV or more, and the summed energy including its surrounding blocks was more than 25 MeV, we considered it as a cluster. Note that if there were two clusters nearby, shown in Fig.3.8(b), the energy and position of both clusters might be incorrectly calculated. It caused the inefficiency in the analysis of physics modes. The influence of this effect will be discussed in Section 4.4.

---

[4] The average momentum of electrons used in the calibration was about 1.5 GeV/c.

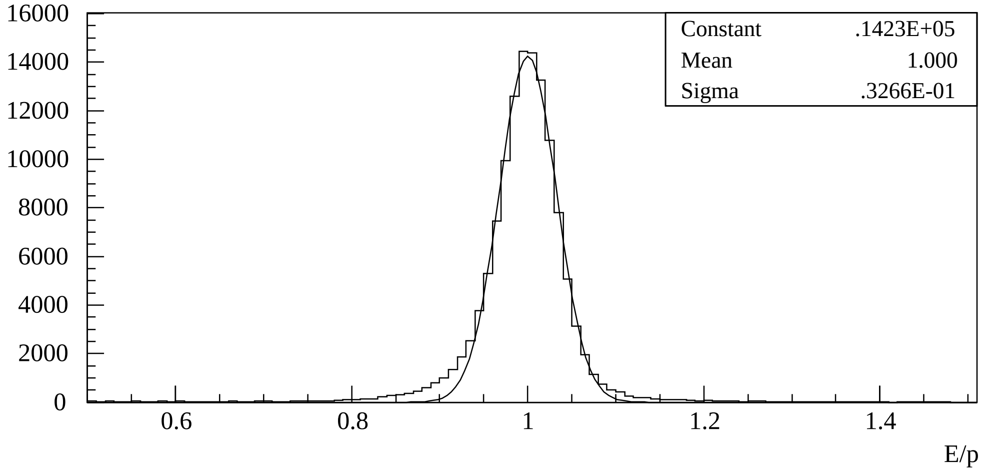

Figure 3.7: E/p distribution of all blocks for electrons. The curve indicates the best fit to the Gaussian form. The deviation at lower tail was considered to be the effect due to the radiation from electrons.

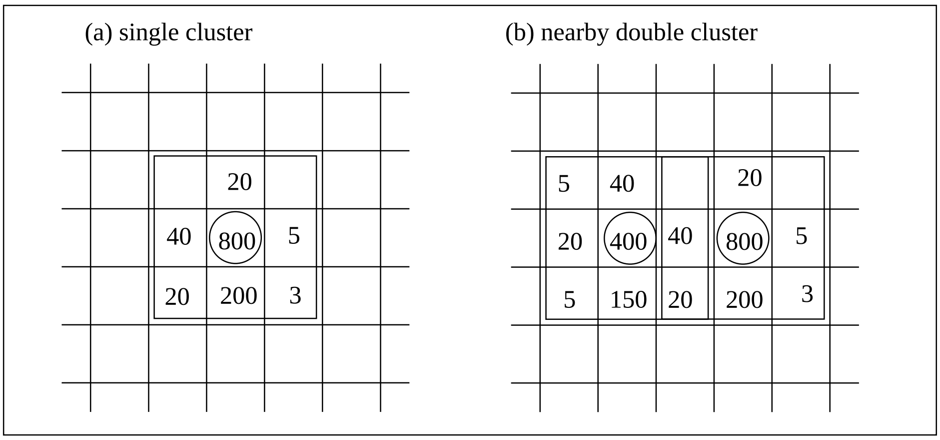

Figure 3.8: Schematic drawings of the cluster finding procedure. A number in each box indicates an energy deposit in MeV. The blocks marked with a circle were identified as a center of a cluster. Each figure represents (a) a typical case, and (b) a case in which there were two particle incident nearby and their showers merged each other. In this case, the energy of both clusters were incorrectly calculated. It caused the inefficiency in the analysis of physics modes, as will be discussed in Section 4.4.

3.3.3 Determination of Cluster Position

Once a cluster was defined, the sum of energy (E), the center of gravity weighted by energy deposit (X_G, Y_G) were calculated. The point (X_G, Y_G) was used as the cluster position, in case that the incident particle was neither an electron nor a photon. In case of an electromagnetic component ($e^{\pm}$ or γ), whose shower profile was well described by an exponential form, another calculation method was employed. Figure 3.9 shows the relation between X position of electrons measured by drift chambers (X_{DC}) and that by the calorimeter (X_G). X'_{DC} and X'_G in the figure are the local coordinates in which the center of the block was defined as the origin. It was found that the relation between X'_{DC} and X'_G also depended on the incident angle (θ) to the block, in addition to the well-know "S-curve" behavior [20]. We calculated the position X'_{calc}, as a function of X'_G and θ, by

$$X'_{calc} = b \cdot \sinh^{-1}\left[(X'_G/\Delta)\sinh(\Delta/b)\right] + A_1\theta + A_3\theta^3 \ , \qquad (3.5)$$

where Δ is a half width of a block, i.e. 35 mm. The coefficient b is a measure of the shower shape in the calorimeter while parameters A_1 and A_3 are the correction coefficients for the incident angle. These parameters (A_1, A_3 and b) were obtained by fitting the actual data to the function of Eqn.(3.5). The position resolution, shown in Figure 3.10, was defined as difference between X'_{DC} and X'_{calc}, and was found to be about 7 mm.

3.3.4 Timing Requirement

To reduce accidental clusters, a timing requirement was imposed on signals from blocks, which were discriminated with a threshold voltage equivalent to about 50 MeV. Since the energy of incident particles extended a wide range, the timing jitter due to the pulse height variation was a serious matter. Figure 3.11(a) shows a scatter plot of TDC vs ADC counts in K_{e3} events. As can be seen in the figure, there existed obvious correlation between the hit time and the pulse height of blocks. To alleviate the timing jitter, we made a correction to TDC counts with ADC counts; the correction function was obtained by fitting the plot to the polynomials. Fig.3.11(b) and (c) show a scatter plot of TDC vs ADC after the correction and its projection onto TDC axis, respectively. Fitting to the Gaussian shape, as shown in Fig.3.11(c), we found the timing resolution to be about 700 psec.[5] We required a cluster to occur within ± 7.5 nsec (which is $\pm 5\sigma$ cut) of the event time. Actually, the corrected TDC of a center block of the cluster was examined. Note that in the region below 100 counts of ADC (equivalent to about 150 MeV), the dependence of TDC upon ADC value was too steep, as can be seen in Fig.3.11(a), to make a reliable correction. In the actual analysis, no timing cut was applied to the clusters with less than 200 MeV.

---

[5] About 25 psec per count in the TDC we used.

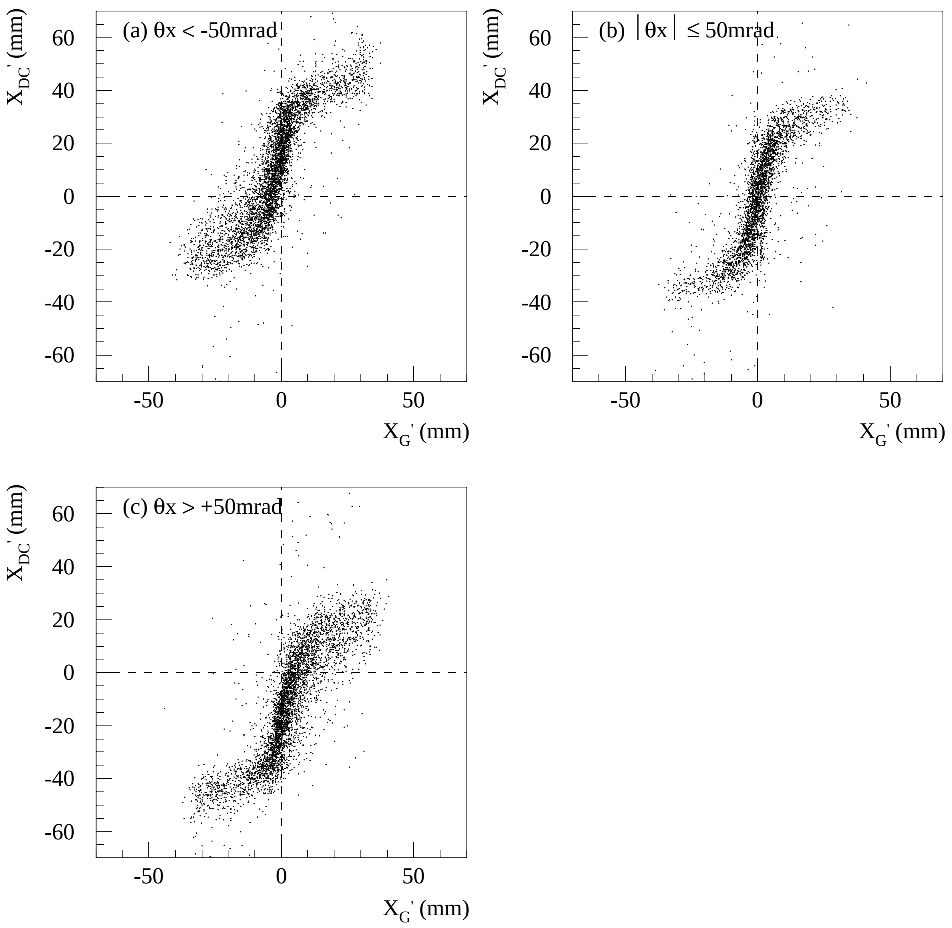

Figure 3.9: X position of electrons measured by drift chambers vs that by the center of gravity of a cluster in the calorimeter. The positions in both axes were represented in the local coordinate, explained in the text. Incident angles of electrons to the calorimeter were (a) -50 mrad or smaller, (b) within ±50 mrad, and (c) +50 mrad or larger.

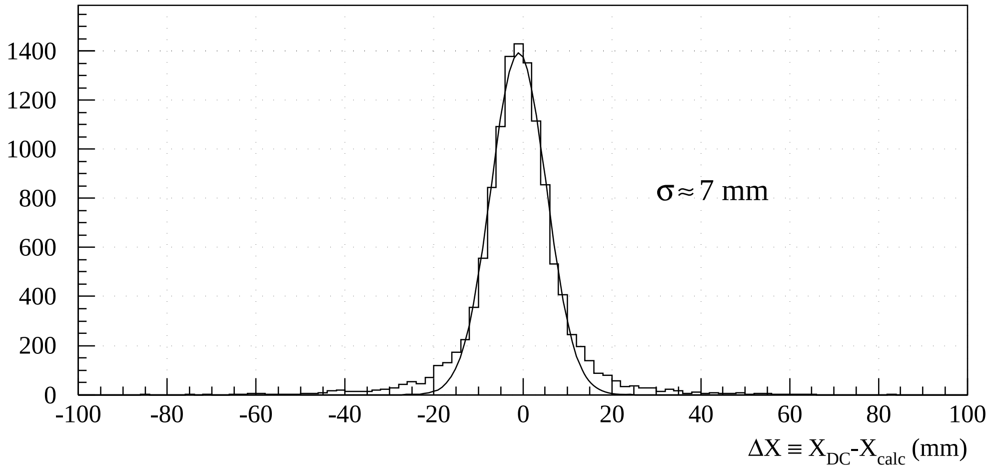

Figure 3.10: Position resolution of the calorimeter for electrons in the X-view.

3.4 Track and Cluster Matching

Any charged particles, either electrons and pions, should have both tracks and clusters. We defined a "matched track" as the track whose projection onto the calorimeter was within 70 mm from a certain cluster. Figure 3.12 shows the distributions of the distance between track and cluster positions; (a) Monte Carlo events for $K_L \to \pi^+\pi^-\pi^0_D$ and (b) an example of experimental data, respectively. $\Delta X(\Delta Y)$ in the figures were defined as $X_{DC} - X_G(Y_{DC} - Y_G)$, the distance between X(Y) position measured by drift chambers and that by the calorimeter. The cut value of 70 mm, represented as a circle in the plot, was determined from the distributions with some margins.

3.5 Particle Identification

To identify species of charged particles, we used the information of their energy deposit in the calorimeter (E), their momentum measured by the spectrometer (p) and hits of gas Cherenkov counter. An electron was identified as a matched track with its energy deposit in the calorimeter to be at least 200 MeV, the energy-to-momentum ratio (E/p) within the range of $0.9 \leq E/p \leq 1.1$, and gas Cherenkov counter hits in corresponding cells. It can be seen in Fig.3.7, the E/p distribution for electrons, that the range was equivalent to $\pm 3\sigma$ cut.

A pion was identified as a matched track with $E/p < 0.7$, Figure 3.13 shows the E/p distribution for pions, which was obtained by pions in reconstructed $K_L \to \pi^+\pi^-\pi^0$ events, without particle identification by E/p. Note that we could not distinguish pions from protons or muons, thus what we called a pion might be a proton or a muon.

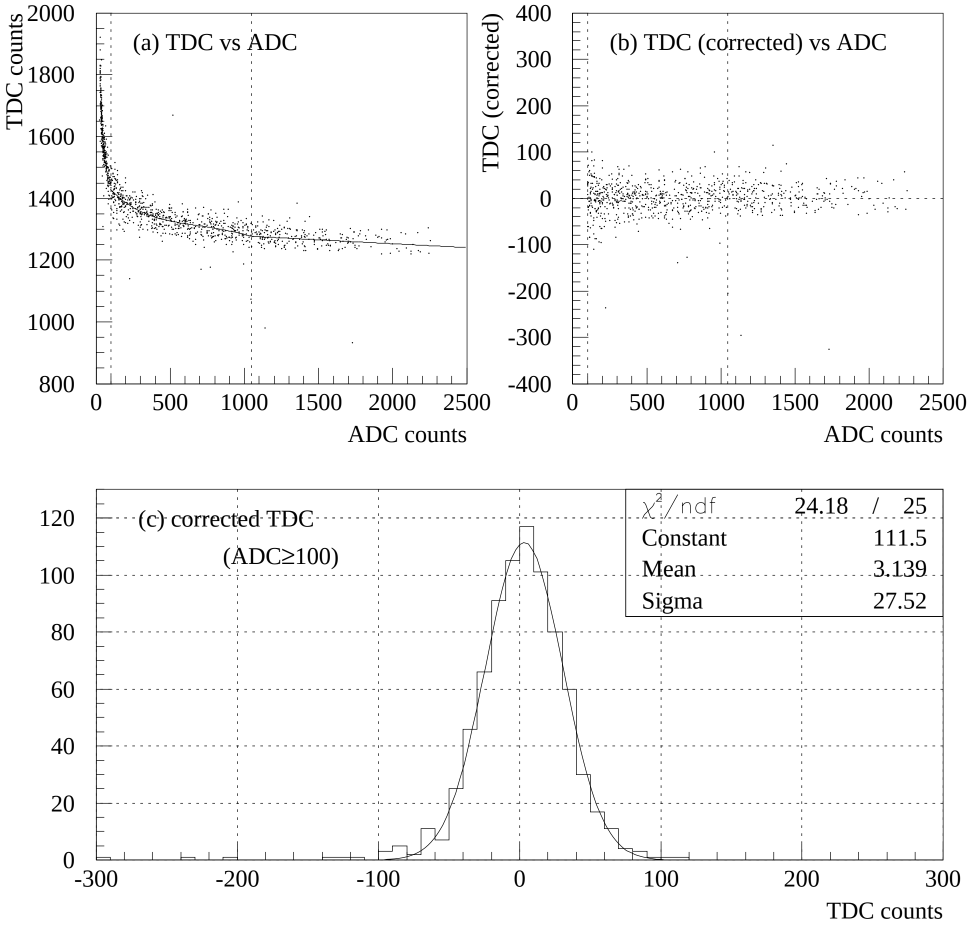

Figure 3.11: TDC distributions of the block in the calorimeter. (a) A scatter plot of TDC vs ADC counts. As can be seen in the plot, there existed obvious correlation between the hit time and the pulse height of blocks. A curve in the plot represents a function, with which the correction of TDC was made. (b) The relation between ADC and TDC counts after the pulse height correction. In the region below 100 counts of ADC (equivalent to about 150 MeV), the dependence of TDC upon ADC value was too steep to make a reliable correction. (c) The distribution of corrected TDC counts. It is a projection of (b) onto TDC axis.

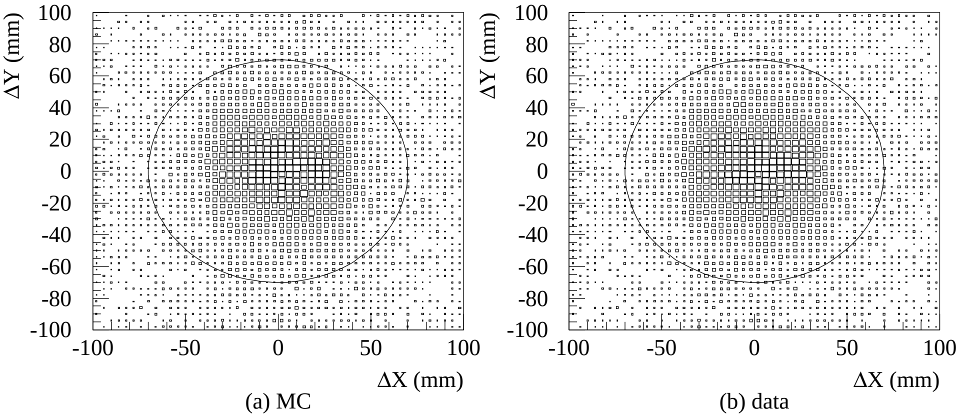

Figure 3.12: Scatter plots which indicate distance between track position and cluster position for (a) MC and (b) one set of data. They are drawn with proportional boxes. In both cases, the cluster position is represented by the center of gravity of a cluster.

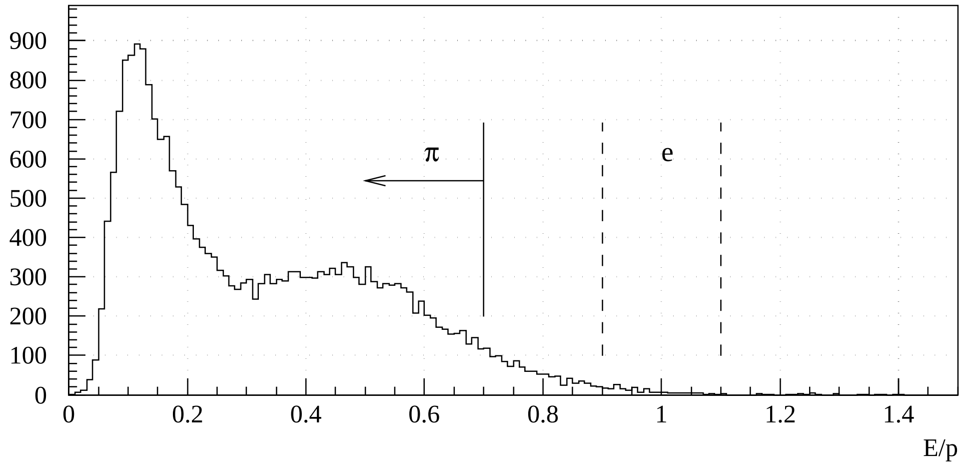

Figure 3.13: E/p distribution for pions in $K_L \to \pi^+\pi^-\pi^0$ events. Events in the histogram were required to have no GC hit. The particle identification by E/p was not performed. Pions in the region of $0.9 \leq E/p \leq 1.1$ would be misidentified as electrons.

The probability to misidentify a pion as an electron was estimated to be about 7×10^{-3}, by the number of pions in the region of $0.9 \leq E/p \leq 1.1$ in Fig.3.13. Combined with pion rejection factor of GC ($\sim$1/50), the probability of misidentification $\pi \to e$ was expected to be about 10^{-4}. The probability of misidentification $e \to \pi$ was estimated by fitting the lower tail of E/p distribution for electrons, shown in Fig.3.7, to an exponential function. It was found to be less than 10^{-5} in average and order of 10^{-4} in the peripheral blocks where the influence of shower leakage became a problem.

Photons were defined as clusters which could not relate to any tracks. It was also required to have an energy of 200 MeV or more.

Although we considered unmatched tracks as photons, it might be other neutrals, for example neutrons. These misidentification ($\pi \leftrightarrow e$, $\mu \to \pi$, $n \to \gamma$, etc.) would be the source of potential backgrounds in the analysis. These backgrounds could be eliminated only by kinematical constraints. Detailed consideration will be described in next chapter.

3.6 Calculation of Decay Vertex

We employed two different methods in the calculation of vertex point. In both cases, a vertex was calculated using the information of only upstream tracks. In case of a vertex with two tracks, we attempted to find a pair of points on each track which were closest to each other. The mid point of them was defined as a vertex. If there existed more than two tracks, we adopted the other method; it searched for the Z plane in which the projection points of all tracks focused each other. In the actual analysis, varying Z plane, we minimized a quantity called χ_v^2, which is defined by

$$\chi_v^2 = \sum_{i=1}^{n} \{(w_x(X_i - X_v))^2 + (w_y(Y_i - Y_v))^2\} , \tag{3.6}$$

where n denotes the number of tracks in a given event, (X_v, Y_v, Z_v) is the vertex position, $X_i(Y_i)$ denotes X(Y) position of i-th track in the specified Z plane (Z_v), and $w_{x(y)}$ denotes the weight associated with the resolution of X(Y) position, respectively. As a starting position of the search, a vertex of first two tracks, calculated by the former method, was taken. For example, in the analysis of $K_L \to \pi^+\pi^-e^+e^-$, an initial value was calculated by two pions and then a vertex of four tracks, adding two electrons, was calculated.

Chapter 4

Analysis of the Physics Mode

In this chapter, procedures of the analysis for the physics modes, $K_L \to \pi^+\pi^-\pi^0_D$ and $K_L \to \pi^+\pi^-e^+e^-$, are described. Here, $K_L \to \pi^+\pi^-\pi^0_D$ denotes the decay $K_L \to \pi^+\pi^-\pi^0$ with π^0 dalitz decay ($\pi^0 \to e^+e^-\gamma$). In the first section, the sequence of event selection, which was common to both modes, is explained. Next, the description of the analysis for the normalization process $K_L \to \pi^+\pi^-\pi^0_D$ follows. And then the analysis for the target mode $K_L \to \pi^+\pi^-e^+e^-$ is described. Finally, the calculation of the branching ratio will be performed and the results of the experiment will be given.

4.1 General Event Selections

In the offline analysis, event selections, which were common to both the target mode and the normalization mode, were performed by taking several steps. At first, the pre-selection was performed immediately after data taking, mainly to reduce the size of raw data sample. Secondly, basic selections were imposed on data; this step included particle identification, vertex calculation of four tracks, and application of cuts against backgrounds. Finally, the preparation of separate analysis for each mode followed.

4.1.1 Pre-selection and Basic Selections

As is mentioned, the pre-selection was performed immediately after data taking. Because we set the trigger conditions loose enough not to lose any genuine events, background events accounted for much of the raw data. The purpose of the pre-selection was to reduce event samples by simple track requirements.

The pre-selection started with reconstruction of all possible tracks. The number of tracks was required to be at least 3. Then, vertex positions were calculated for all possible combination of tracks. If none of resultant vertex positions were inside the beam region in the decay volume, the event was discarded. For ex-

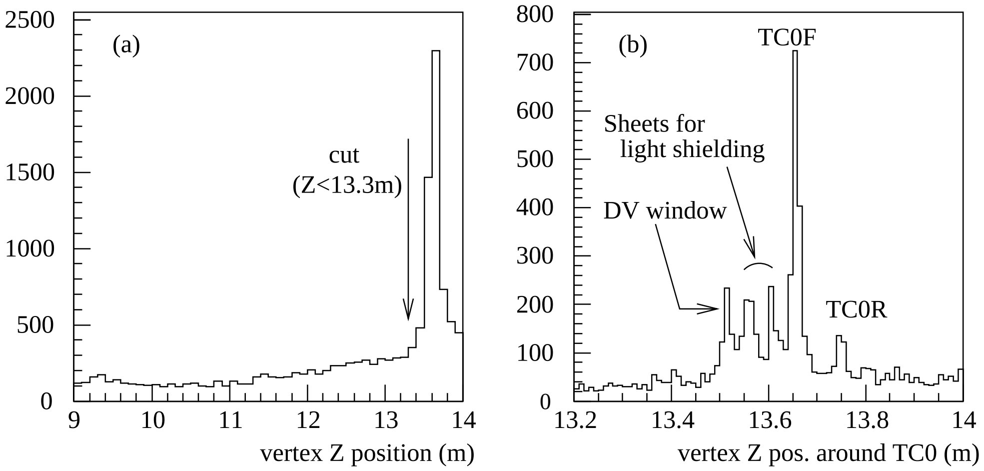

Figure 4.1: The distribution of reconstructed vertex Z position of any two track candidates; (a) overview of the whole decay volume region and (b) magnified view around TC0. Events in the histogram were required to have at least 3 tracks.

ample, background events originating from TC0 by interactions with the neutral beam were removed by this condition. Figure 4.1 shows the distribution of reconstructed vertex position along the beam line before the cut. Clear peaks exist at the position corresponding to the window of the decay volume, TC0F/R, and their light shielding sheets. (See Fig.4.1(b).) Next, clusters in the calorimeter were searched. We demanded events to have at least 4 clusters with their energy greater than 25 MeV. Then, momenta of charged tracks were calculated at this stage, and were retained for further analysis, though no cut was applied.

The next step in the analysis was the basic selection. Its main purpose was to select out events consistent with $\pi^+\pi^-e^+e^-$ topology. At first, each event was required to have at least 4 track candidates, in which the number of matched tracks was required to be exactly 4. Then, using E/p value and the hit information from the gas Cherenkov counter, the particle species were identified. Figure 4.2 shows an example of E/p distribution at this step. With the information of the electric charge of tracks, obtained by the bending direction, an event was required to contain $\pi^+\pi^-e^+e^-$.

Then the vertex position was calculated with these four tracks, and was requested to be within the beam region in the decay volume. The quality of the vertex was also examined. Figure 4.3 shows the χ^2_v distribution (see Eqn.(3.6) for the definition), of the data sample remained at this stage. We applied a cut at $\chi^2_v = 6$, which was determined from the distribution.

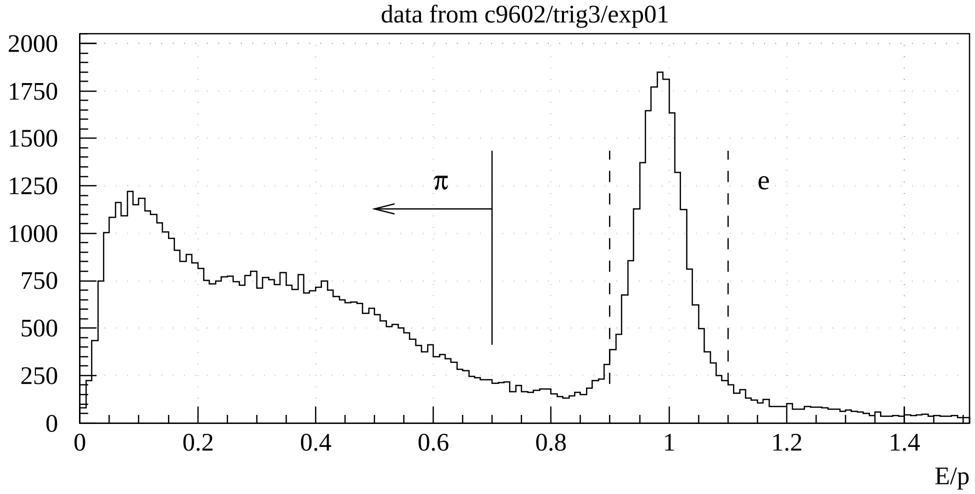

Figure 4.2: E/p distribution from one set of data. A track was defined as pions below the arrow in the figure and as electrons between fence lines on E/p=0.9 and 1.1.

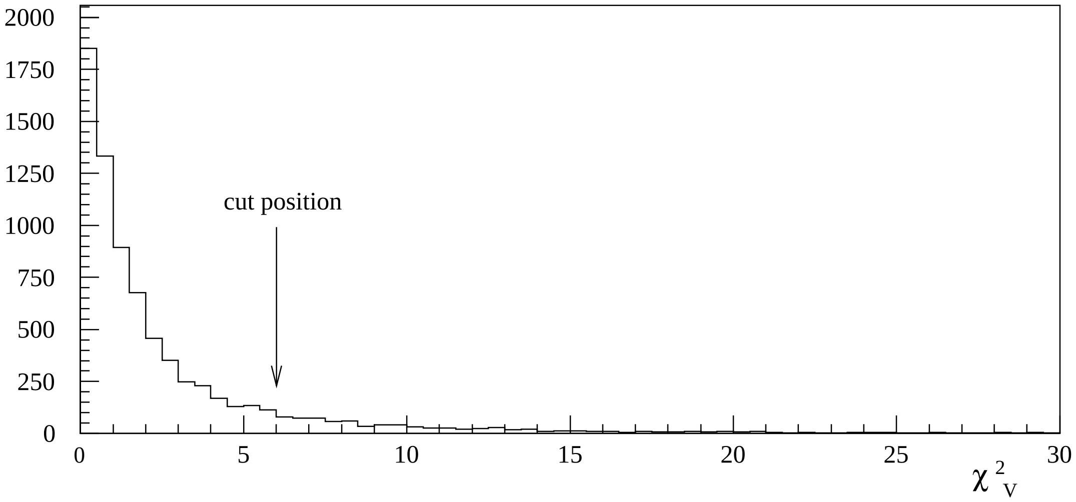

Figure 4.3: The distribution of χ^2_v value which represents vertex quality. The cut value is shown as an arrow in the figure.

4.1.2 Background Rejection

Among the background rejection procedure, we first dealt with accidental backgrounds. In order to eliminate events with many accidental activities, number of hit clusters[1] on each upstream chamber should be less than 14.[2]

Two major sources of background events common to both normalization and signal modes were nuclear interactions and photon conversions. The description of the methods to remove them follows. Effects of applied cuts on the signal and/or the normalization modes, will be discussed in Section 4.4.

Backgrounds from Nuclear Interactions

Backgrounds from nuclear interactions were one of the serious problems for our experiment. They were generated by the interactions of neutrons in the beam with, for example, gas atoms in the decay volume. If they produced two charged particles, such as protons and/or $\pi^{\pm}$, and a π^0 which decayed into $e^+e^-\gamma$, they might be identified as $\pi^+\pi^-e^+e^-$ candidates. Note that we could only distinguish pions from electrons, i.e. what we call a pion here might be a muon or a proton. In this case, the distribution of invariant mass of secondary particles was expected to be almost uniform, and thus they might spread inside the signal region. To reduce this kind of backgrounds, we required charged pion candidates to fulfill the following two conditions. One was the condition about the magnitude of momenta and the other was their asymmetry. Interactions such as $nN \to \pi^- pX$ tend to produce fast protons and to create charge asymmetry in momentum. Figure 4.4(a) shows the momentum distribution of pions with each charge and (b) shows their asymmetry, defined as $A_{+-} = (p_{\pi^+} - p_{\pi^-})/(p_{\pi^+} + p_{\pi^-})$. As explained, they show quite asymmetric distributions due to nuclear interactions.[3] Figure 4.5 shows the same distributions obtained by a Monte Carlo simulation for $K_L \to \pi^+\pi^-e^+e^-$ and $K_L \to \pi^+\pi^-\pi^0_D$ modes. In the actual analysis, pion momenta was required to be less than 4 GeV/c and their asymmetry A_{+-} was limited within ± 0.5. These cuts removed effectively the background events due to the nuclear interactions.

Backgrounds from Photon Conversions

One of the basic processes which could constitute background events was the photon converting into an e^+e^- pair in various materials (photon conversion). For example, the decay mode $K_L \to \pi^+\pi^-\pi^0(2\gamma)$ with the photon conversion could

---

[1] The hit cluster was defined as the continuous hits on one chamber plane. In usual, it consisted of one or two hits.

[2] The loss of signals by this condition was examined with reconstructed $K_L \to \pi^+\pi^-\pi^0_D$ data and found to be negligible.

[3] To contrast the problem clearly, events in these plots are required to have the invariant mass of $\pi^+\pi^-e^+e^-$ above 480MeV/c^2

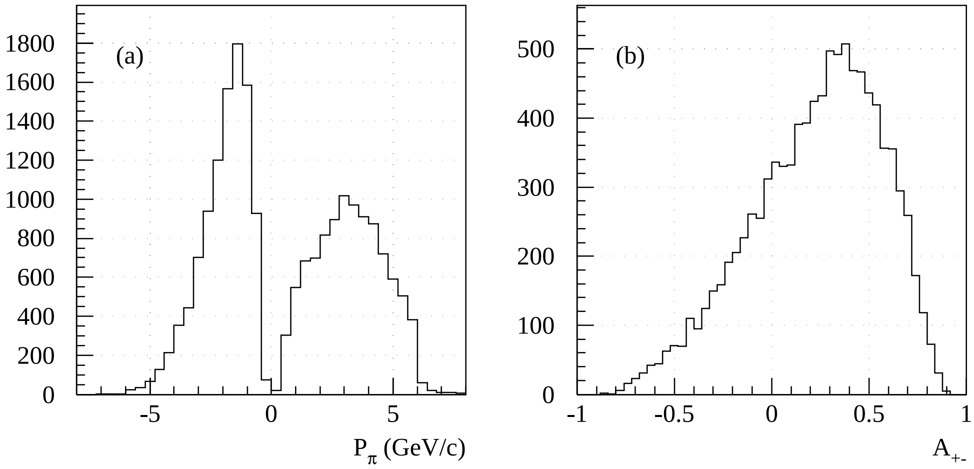

Figure 4.4: (a) The distribution of reconstructed momentum of pions with each charge. Sign of the value represents the charge. (b) The distribution of momentum asymmetry of pions: A_{+-}, defined in the text. To contrast the problem clearly, events in these plot are required to have the invariant mass of $\pi^+\pi^-e^+e^-$ above 480MeV/c^2, where the effect from K_L decay events is small.

mimic the $K_L \to \pi^+\pi^-\pi^0_D$ process, and thus should be distinguished. There are two distinct features in the photon conversion process; the e^+e^- pair has nearby zero invariant mass, and the tracks by the pair tend to trace almost same trajectory before the magnet. Thus, exploiting the former feature, we imposed a cut on the e^+e^- invariant mass (M_{ee}). Figure 4.6 shows the M_{ee} distributions for three different data sets; (a) a Monte Carlo simulation for the $K_L \to \pi^+\pi^-\pi^0(2\gamma)$ with one photon conversion at the window material of the decay volume, (b) a Monte Carlo simulation for the $K_L \to \pi^+\pi^-\pi^0_D$ mode, and (c) the experimental data identified as the $K_L \to \pi^+\pi^-\pi^0_D$ mode without the M_{ee} and N_{shared} (see below) cuts. The actual cut on M_{ee} was set to be 4 MeV/c^2.

As mentioned, the e^+e^- tracks by the photon conversion trace almost same trajectory upstream of the magnet. At the stage of track finding, each trajectory was required to have a hit on every DC planes, allowing common use of a hit to other tracks. If two trajectories were close to each other, many hit cells would be shared. We counted the number of shared cells (N_{shared}) separately for DC1 (composed of 6 planes) and DC2. Figures 4.7 shows the N_{shared} distribution for DC1 and DC2; the three different data sets (a)-(c) are the same for Fig.4.6. We required N_{shared} to be 4 or less for both DC1 and DC2. The cuts imposed on M_{ee} and N_{shared} excluded about 96% of e^+e^- pairs originating from the photon conversion.

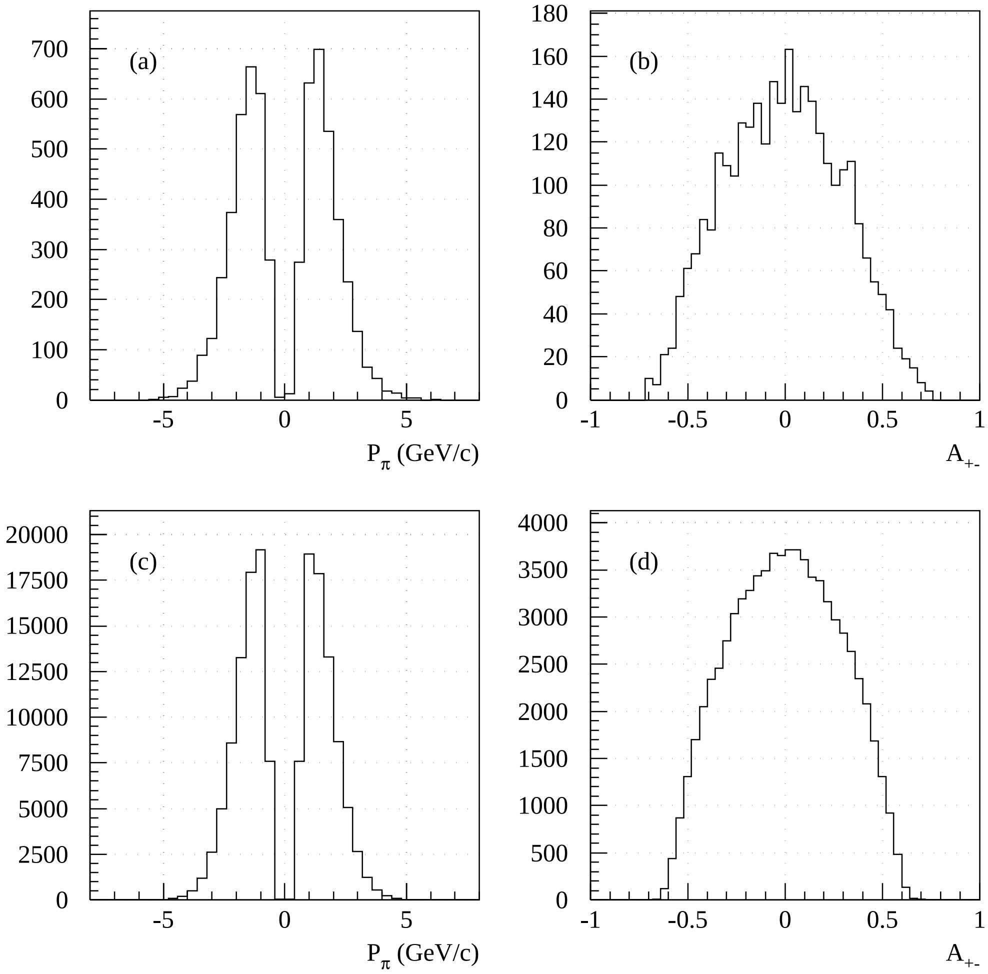

Figure 4.5: The distributions of (a)(c) pion momentum and (b)(d) their asymmetry of simulated $K_L \to \pi^+\pi^-e^+e^-$ and $K_L \to \pi^+\pi^-\pi^0_D$, respectively.

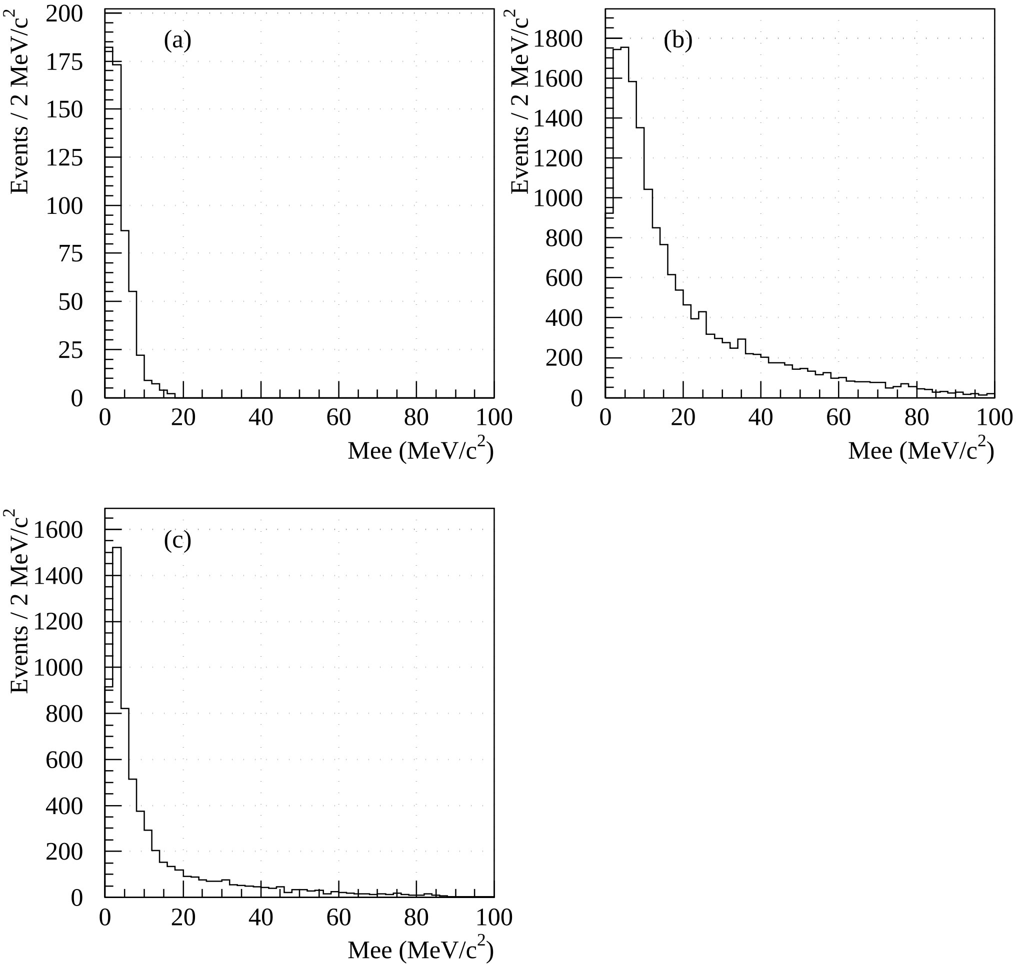

Figure 4.6: The distribution of the invariant mass M_{ee}. The three data sets presented are (a) a Monte Carlo simulation for $K_L \to \pi^+\pi^-\pi^0(2\gamma)$ with the photon conversion, (b) a Monte Carlo simulation for $K_L \to \pi^+\pi^-\pi^0_D$, (c) the experimental data of the $K_L \to \pi^+\pi^-\pi^0_D$ events without M_{ee} and $N_{\rm shared}$ cuts.

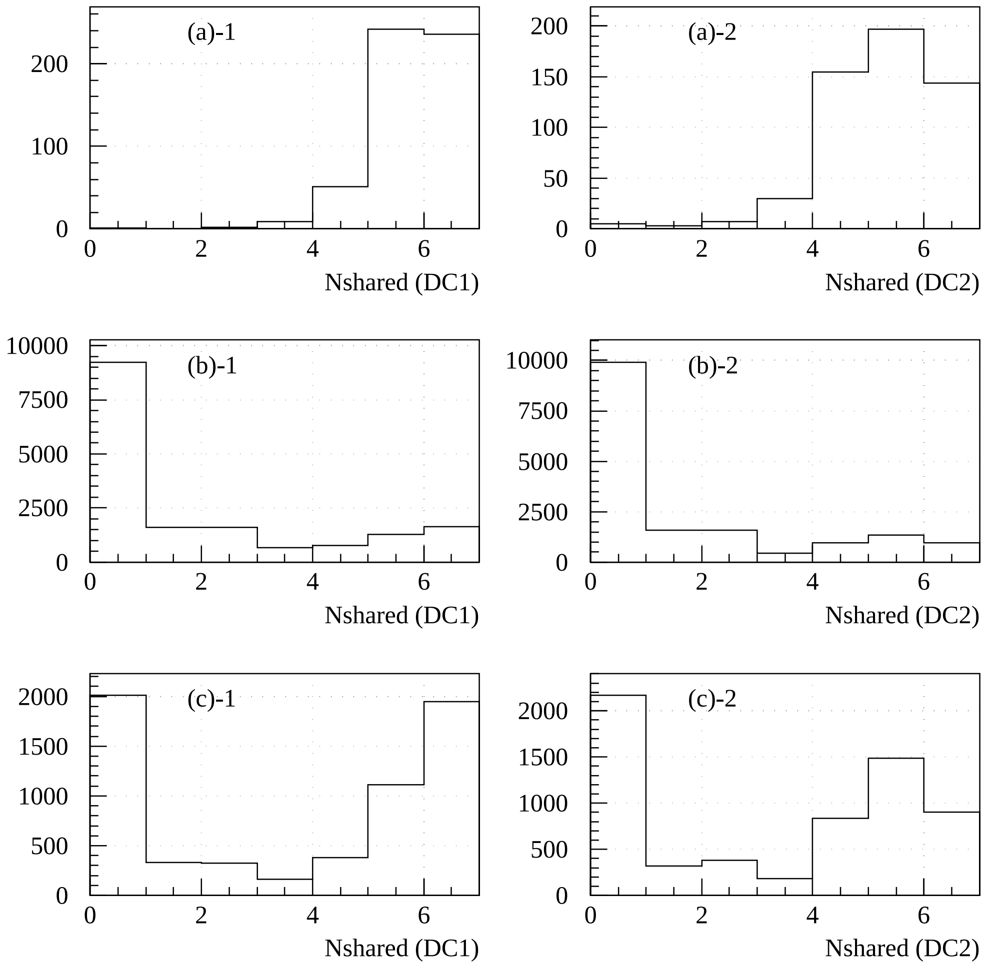

Figure 4.7: The distribution of number of shared hits by e^+e^- trajectories on DC1 and DC2. The three data sets presented are (a) a Monte Carlo simulation for $K_L \to \pi^+\pi^-\pi^0(2\gamma)$ with the photon conversion, (b) a Monte Carlo simulation for $K_L \to \pi^+\pi^-\pi^0_D$, (c) the experimental data of the $K_L \to \pi^+\pi^-\pi^0_D$ events without M_{ee} and $\mathrm{N_{shared}}$ cuts.

Table 4.1: Summary of the event sample for the physics analysis.

Cuts	$K_L \to \pi^+\pi^-e^+e^-$ candidates	$K_L \to \pi^+\pi^-\pi^0_D$ candidates
Topological	$\pi^+\pi^-e^+e^-$	
Nuclear int.	$p_\pi < 4GeV/c$ and $\lvert A_{+-}\rvert \leq 0.5$	
Photon conv.	$M_{ee} \geq 4MeV/c^2$ and $\mathrm{N}_{shared} \leq 4$	
Photon	Not required	Required
Loose θ^2 cut	$\theta^2_{\pi\pi ee} \leq 100\mathrm{mrad}^2$	$\theta^2_{\pi\pi ee\gamma} \leq 100\mathrm{mrad}^2$
Loose mass cut	$\lvert M_{\pi\pi ee} - M_{K_L}\rvert \leq 100MeV/c^2$	$\lvert M_{\pi\pi ee\gamma} - M_{K_L}\rvert \leq 100MeV/c^2$

4.1.3 Event Sample for the Physics Analysis

Before going to the analysis for the physics modes, we summarize the event sample remaining at this stage.

So far, general requirements were imposed on events for both the signal mode and the normalization mode. At first, events were required to be consistent with $\pi^+\pi^-e^+e^-$ topology in the basic selections. Next, the cuts were imposed to eliminate two types of backgrounds. To reduce backgrounds from nuclear interactions, pion momenta and their asymmetry A_{+-} were required to be less than 4 GeV/c and within ±0.5, respectively. To eliminate backgrounds containing the photon conversion, the invariant mass of e^+e^- was required to be at least 4 MeV/c^2, and the number of cells shared with e^+e^- was demanded to be less than 4 for both DC1 and DC2.

In addition to these requirements, separate cuts were imposed on event candidates in each mode, to reduce the number of samples.

Actually, these were rather loose conditions on the invariant mass and θ^2 of $\pi^+\pi^-e^+e^-(\gamma)$, where θ denotes the angle of the reconstructed total momentum with respect to the line connecting the production target and decay vertex. In case of the signal mode $K_L \to \pi^+\pi^-e^+e^-$, the invariant mass and θ^2 of $\pi^+\pi^-e^+e^-$ was required to be within ±100 MeV/c^2 of the K_L mass and to be 100 mrad^2 or smaller, respectively. We call the remaining events "$\pi^+\pi^-e^+e^-$ candidates".

In case of the normalization mode $K_L \to \pi^+\pi^-\pi^0_D$, whose final state contains $\pi^+\pi^-e^+e^-\gamma$, we also required the existence of photon candidates.[4] Then, the invariant mass and θ^2 of $\pi^+\pi^-e^+e^-\gamma$ was required to be within ±100 MeV/c^2 of the K_L mass and to be 100 mrad^2 or smaller, respectively, which were same conditions as for the signal mode. We call the remaining events "$\pi^+\pi^-\pi^0_D$ candidates".

These two event samples, summarized in Table 4.1, are the basic ingredients to the physics analysis described in the following sections.

---

[4] If there were two or more photon candidates, we selected the one with which the invariant mass of $e^+e^-\gamma$ was closest to the π^0 mass.

4.2 Analysis for the Normalization Process $K_L \to \pi^+\pi^-\pi^0_D$

In this section, the analysis for the normalization mode $K_L \to \pi^+\pi^-\pi^0_D$ ($K_L \to \pi^+\pi^-\pi^0$ with $\pi^0 \to e^+e^-\gamma$) is described. The mode $K_L \to \pi^+\pi^-\pi^0_D$ was suitable for the normalization. Since it has the same decay products as the signal mode, except for a photon, we could cancel out most of uncertainties in the track reconstruction and particle identification. Also, its effective branching ratio is so large that we could check in detail various properties of our system and could compare with the Monte Carlo simulation. The description of the event reconstruction, consideration of backgrounds, and the resultant number of detected $K_L \to \pi^+\pi^-\pi^0_D$ events, are given in order.

4.2.1 Event Selection and Reconstruction of $K_L \to \pi^+\pi^-\pi^0_D$

We started with the $\pi^+\pi^-\pi^0_D$ candidate sample defined in Section 4.1.3. First of all, we attempted to reconstruct π^0 from e^+, e^- and γ candidates. If there were more than one photon candidates, we selected the one with which the invariant mass of $e^+e^-\gamma$ ($M_{ee\gamma}$) was closest to the π^0 mass (M_{π^0}). Figure 4.8 shows the $M_{ee\gamma}$ distribution. The mass resolution of π^0 was obtained by fitting the distribution to the Gaussian form and was found to be about 5 MeV/c^2. We demanded $M_{ee\gamma}$ to be within ± 15 MeV/c^2 of M_{π^0} (π^0 mass cut). We then calculated the invariant mass ($M_{\pi\pi ee\gamma}$) and θ^2 of $\pi^+\pi^-e^+e^-\gamma$, where θ denotes the angle of the reconstructed total momentum with respect to the line connecting the production target and the decay vertex. If the parent particle came from the target, θ^2 should be zero within the resolution. Figure 4.9 shows the $M_{\pi\pi ee\gamma}$ distribution after the π^0 mass cut. It was found that the mass resolution for K_L to be about 6 MeV/c^2. We requested $M_{\pi\pi ee\gamma}$ to be within ± 18 MeV/c^2 of the K_L mass M_{K_L} (K_L mass cut). Figure 4.10 shows the distribution of θ^2 after both π^0 and K_L mass cuts. The cut position was determined from the figure as $\theta^2 \leq 20$ mrad^2. Figure 4.11 shows a scatter plot of $M_{\pi\pi ee\gamma}$ and θ^2 after the π^0 mass cut. The box in the figure, which represents the K_L mass cut and θ^2 cut, was defined as the signal box. The events left inside the signal box were identified as $\pi^+\pi^-\pi^0_D$ events.

4.2.2 Background from $K_L \to \pi^+\pi^-\pi^0(2\gamma)$ with Photon Conversion

Background events in $K_L \to \pi^+\pi^-\pi^0_D$ came mainly from the decay $K_L \to \pi^+\pi^-\pi^0$ in which π^0 went into two photons and either photon converted to e^+e^- pair. Since this background has the same decay products as the normalization mode, the only way to discriminate it was to utilize the special features of the photon conversion. As mentioned in previous section, we already imposed the cuts on

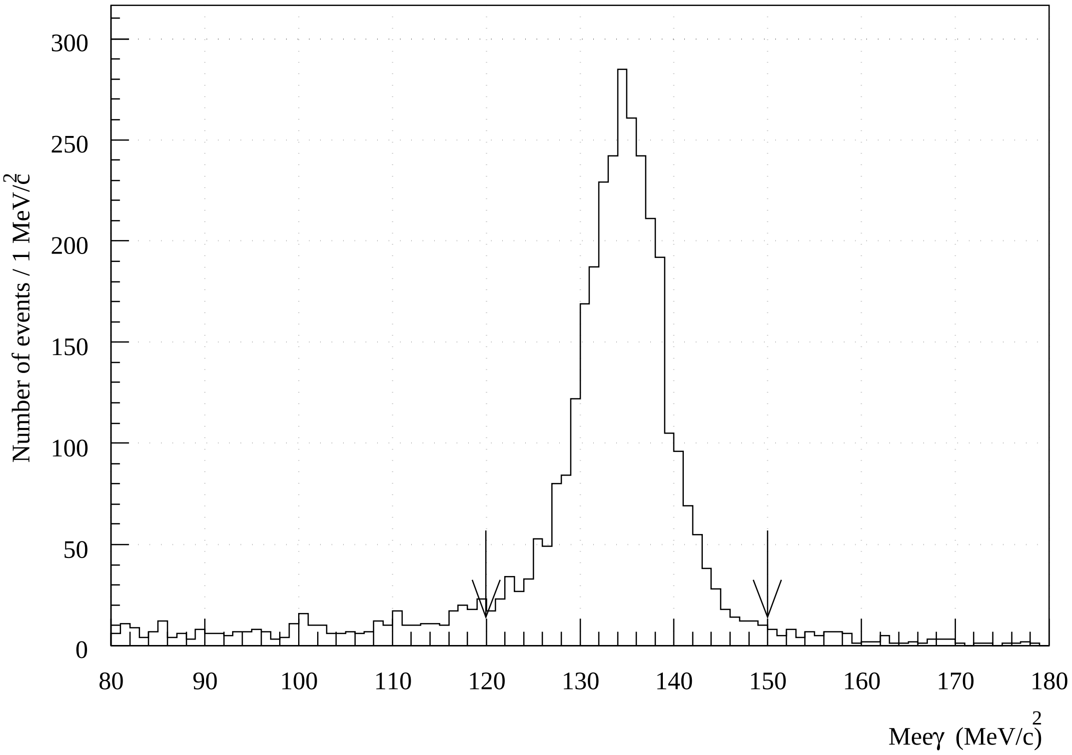

Figure 4.8: The distribution of the invariant mass of $e^+e^-\gamma$. The $\pi^+\pi^-\pi^0_D$ candidate events (see Section 4.1.3) are plotted.

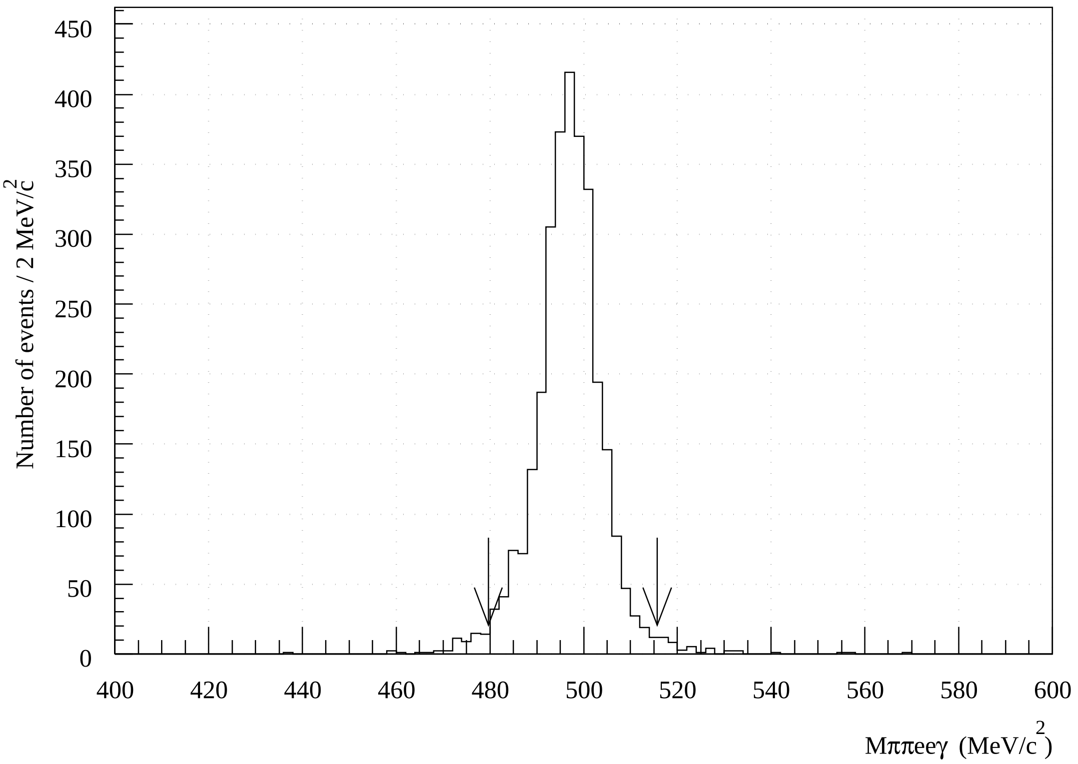

Figure 4.9: The distribution of the $\pi^+\pi^-e^+e^-\gamma$ invariant mass ($M_{\pi\pi ee\gamma}$). The π^0 mass cut was imposed on the $\pi^+\pi^-\pi^0_D$ candidate events.

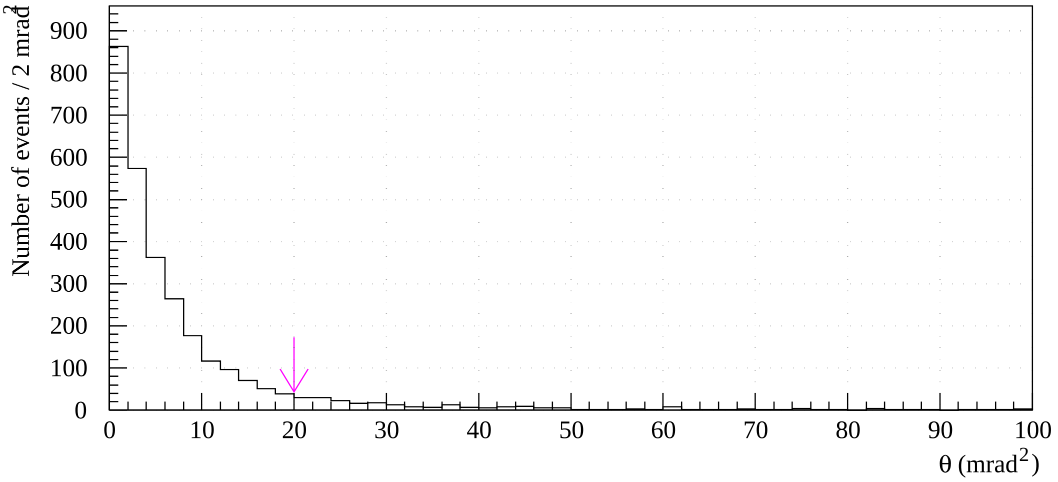

Figure 4.10: The distribution of θ^2 after both π^0 and K_L mass cuts.

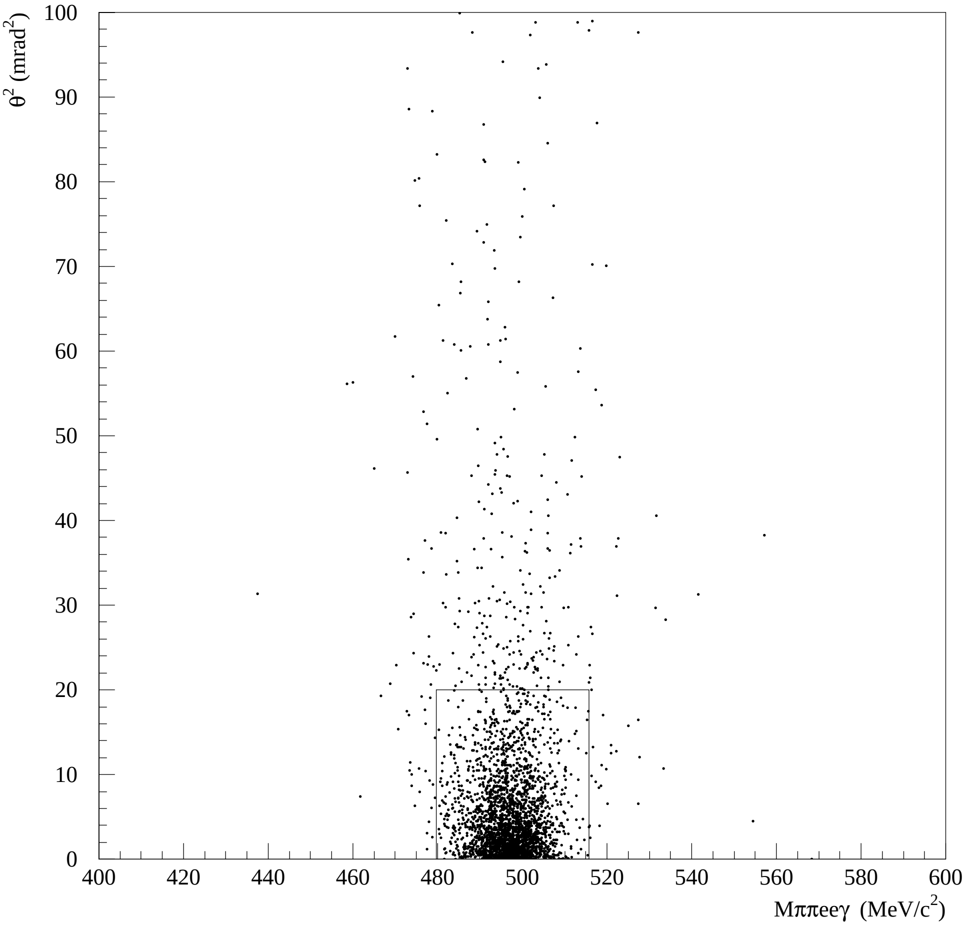

Figure 4.11: A scatter plot of $M_{\pi\pi ee\gamma}$ and θ^2 after the M_{π^0} cut. The box in the figure represents the M_{K_L} and θ^2 cuts.

Table 4.2: Estimation of the background contamination from $K_L \to \pi^+\pi^-\pi^0(2\gamma)$ with the photon conversion in $K_L \to \pi^+\pi^-\pi^0_D$ events.

	$K_L \to \pi^+\pi^-\pi^0_D$	$K_L \to \pi^+\pi^-\pi^0(2\gamma)$	Ratio
Effective B.R.	1.2×10^{-2} [a]	$(4.4 \times 10^{-3}) \times 2$ [b]	0.73
Efficiency of the cuts [c]	0.79	4×10^{-2}	5×10^{-2}
Total contamination ratio ⇒			$\sim 4\%$

[a] Branching ratio of $\pi^0 \to e^+e^-\gamma$.

[b] Probability of the photon conversion by 2. The factor of 2 accounts for the two γ from π^0.

[c] The cuts on N_{shared} and M_{ee}.

M_{ee} and N_{shared} for this purpose.

Here we will estimate the contamination in the signal box by this background. We first estimated the photon conversion probability. By the trigger condition which requested at least 3 hits in TC0, we had only to consider the photon conversion occurring in TC0F or further upstream materials. The probability was estimated to be about 4.4×10^{-3}. Then, we employed Monte Carlo simulation to study the efficiency of the M_{ee} and/or N_{shared} cuts. It was found that the combined reduction factor of the M_{ee} and N_{shared} cuts was 4×10^{-2} while the signal efficiency was 0.79. The results are summarized in Table 4.2. Combining these results, we finally found that the contamination of the photon conversion events inside the signal box was less than 4%.

4.2.3 Number of Remaining $K_L \to \pi^+\pi^-\pi^0_D$ Events

After all the cuts described in previous sections, there remained 2618 $K_L \to \pi^+\pi^-\pi^0_D$ events in the signal box. Distributions of various kinematical variables were calculated and compared with equivalents by a Monte Carlo simulation.[5] Figures 4.12–4.17 show examples of such distributions; they are the K_L, $\pi^\pm$ and $e^\pm$ momentum distributions, the $\pi^+\pi^-$ and e^+e^- invariant mass distributions and the vertex position distribution. As can be seen from these plots, the experimental data and the Monte Carlo simulation agreed well with each other.

---

[5] $K_L \to \pi^+\pi^-\pi^0$ events were generated obeying the energy dependence of Dalitz plot with the parameters summarized in [21]. See Appendix A in detail.

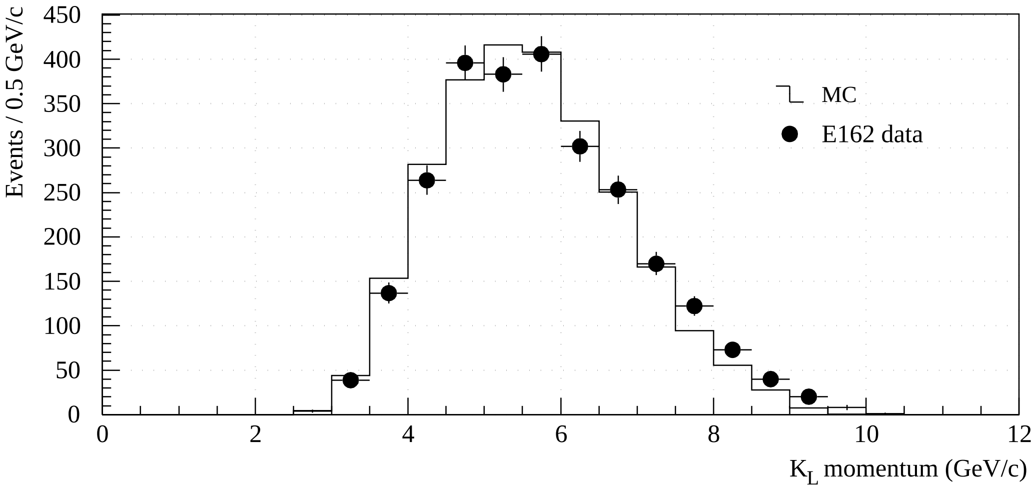

Figure 4.12: The distribution of K_L momentum for the $K_L \to \pi^+\pi^-\pi^0_D$ events. The circles with bar shows the distribution of experimental data and the histogram represents that of simulated events by Monte Carlo program.

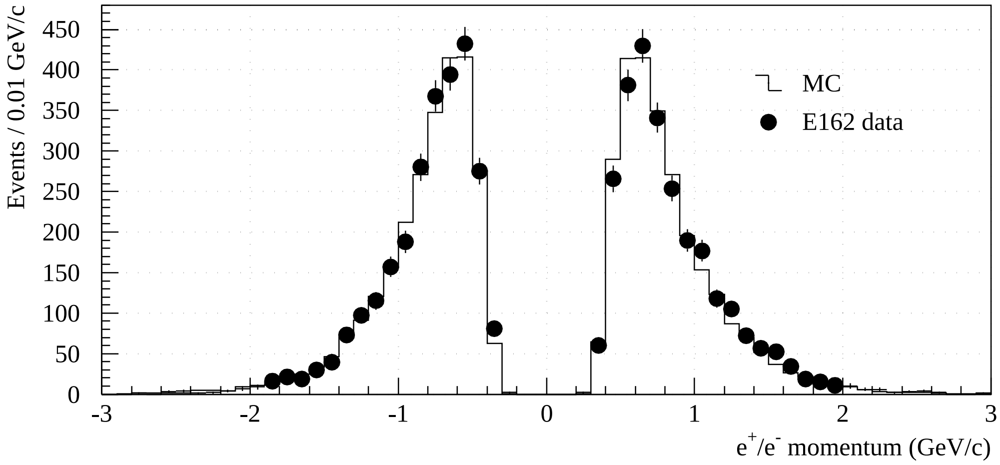

Figure 4.13: The distribution of e^+ and e^- momentum for the $K_L \to \pi^+\pi^-\pi^0_D$ events. The sign of the momentum represents the charge of $e^\pm$.

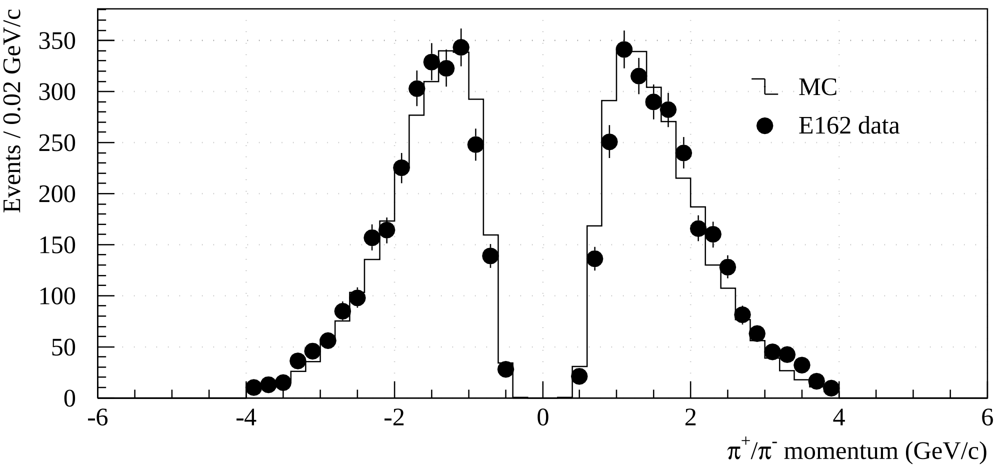

Figure 4.14: The momentum distribution of π^+ and π^- for the $K_L \to \pi^+\pi^-\pi^0_D$ events. The sign of the momentum represents the charge of pions.

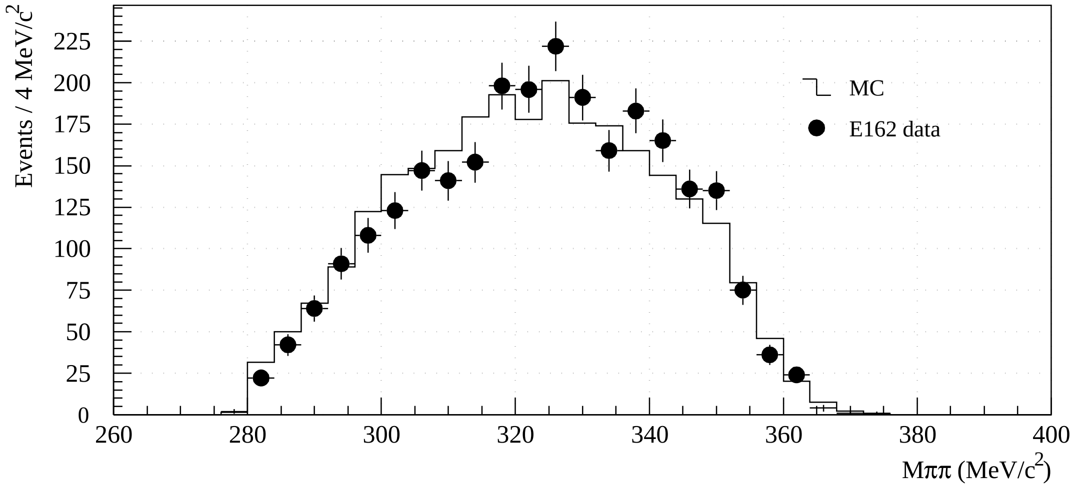

Figure 4.15: The distribution of $\pi^+\pi^-$ invariant mass for the $K_L \to \pi^+\pi^-\pi^0_D$ events.

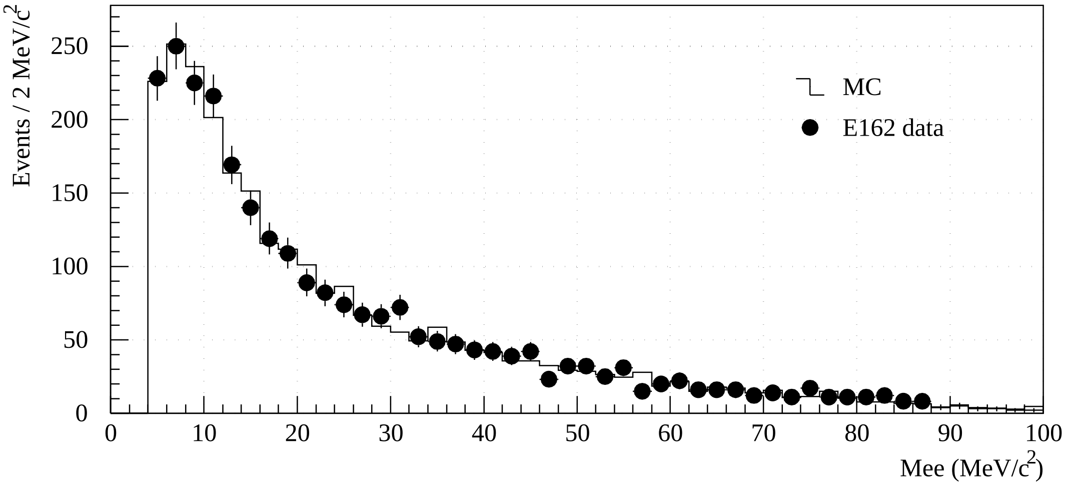

Figure 4.16: The distribution of e^+e^- invariant mass for the $K_L \to \pi^+\pi^-\pi^0_D$ events.

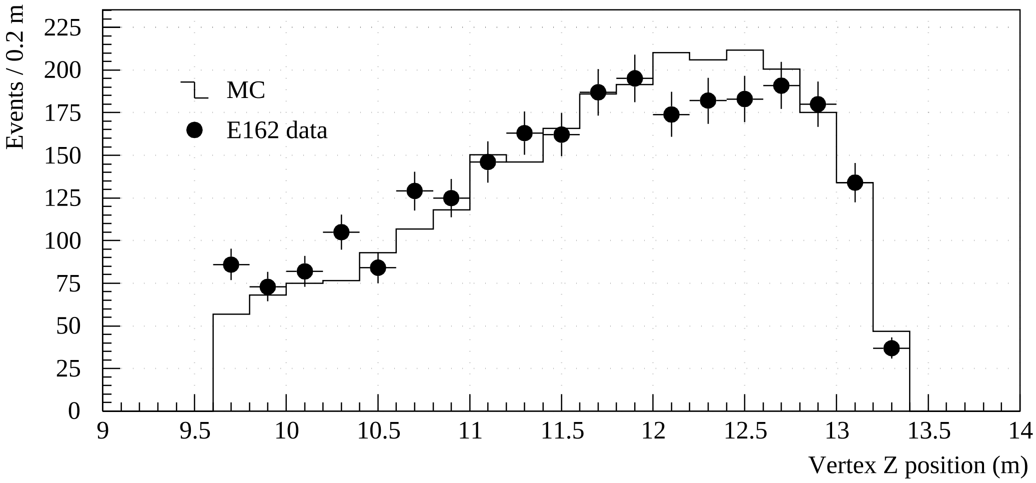

Figure 4.17: The distribution of decay vertex Z position for the $K_L \to \pi^+\pi^-\pi^0_D$ events.

4.3 Analysis for $K_L \to \pi^+\pi^-e^+e^-$

The analysis for $K_L \to \pi^+\pi^-e^+e^-$ is explained in this section. As will be explained in detail below, the main task here is to remove background events. Thus, we start with the discussion of possible background sources. Figure 4.18 shows a scatter plot of $M_{\pi\pi ee}$ vs θ^2. The event sample in the plot is the $\pi^+\pi^-e^+e^-$ candidates, obtained in Section 4.1.3. We remind that the events were allowed to have neutral clusters, on-time or off-time, in the calorimeter. From Fig.4.18, it can be seen that the most of the events lay in the low mass region ($M_{\pi\pi ee} < M_{K_L}$). This suggests that the origin of the backgrounds is K_L decay. It can easily be understood that the main source was the $K_L \to \pi^+\pi^-\pi^0_D$ mode with the photon being missed from detection. We will present an efficient cut to remove this background.

In addition to this, we will consider two other decay modes as a background source; $K_L \to \pi^+\pi^-\gamma$ and $K_L \to \pi e\nu\gamma$. Looking at Fig.4.18, we also notice that there exist some background events scattered uniformly in the high mass region ($M_{\pi\pi ee} > M_{K_L}$). Although the number of such events is not large, there is a chance for this type of the background to invade the signal box. It turned out that the background was produced by nuclear interactions.

Below, we will describe the methods to get rid of these background events, the estimation of the remaining backgrounds inside the signal box, and the final results.

4.3.1 Backgrounds from Nuclear Interactions

Although we applied the cuts to eliminate backgrounds from nuclear interactions, a few of them still remained around the signal region. Figure 4.19(a) shows a scatter plot of $M_{ee\gamma}$ vs $M_{\pi\pi ee}$ for the $\pi^+\pi^-e^+e^-$ candidates with a photon(s). As expected, the events in the plot are dominated by the $K_L \to \pi^+\pi^-\pi^0_D$ mode; they cluster around $M_{\pi\pi ee} \simeq 430 MeV/c^2$ and $M_{ee\gamma} \simeq M_{\pi^0}$. Figure 4.19(b) shows the same scatter plot as (a). In this case, however, the events were requested to pass much looser θ^2 cut; actually $\theta^2 < 1000\text{mrad}^2$ was required instead of $\theta^2 < 100\text{mrad}^2$. Now the π^0 inclusive events can be seen clearly. We thus examined the $e^+e^-\gamma$ invariant mass if an event had a photon(s). We excluded it from the $\pi^+\pi^-e^+e^-$ candidates if $M_{ee\gamma}$ was within ±15 MeV/c^2 of M_{π^0}.[6] Note that $\pi^+\pi^-\pi^0_D$ events were excluded by this cut from the $\pi^+\pi^-e^+e^-$ analysis.

This cut might cause over-veto against signal events if they had an accidental photon. The efficiency loss was examined by imposing a similar condition to the $K_L \to \pi^+\pi^-\pi^0_D$ events. If the invariant mass of e^+e^- and one of extra photons, except the one used in the reconstruction of $K_L \to \pi^+\pi^-\pi^0_D$, was consistent with

---

[6] If the event had several photons, we examined all combinations. It was excluded once π^0 was found.

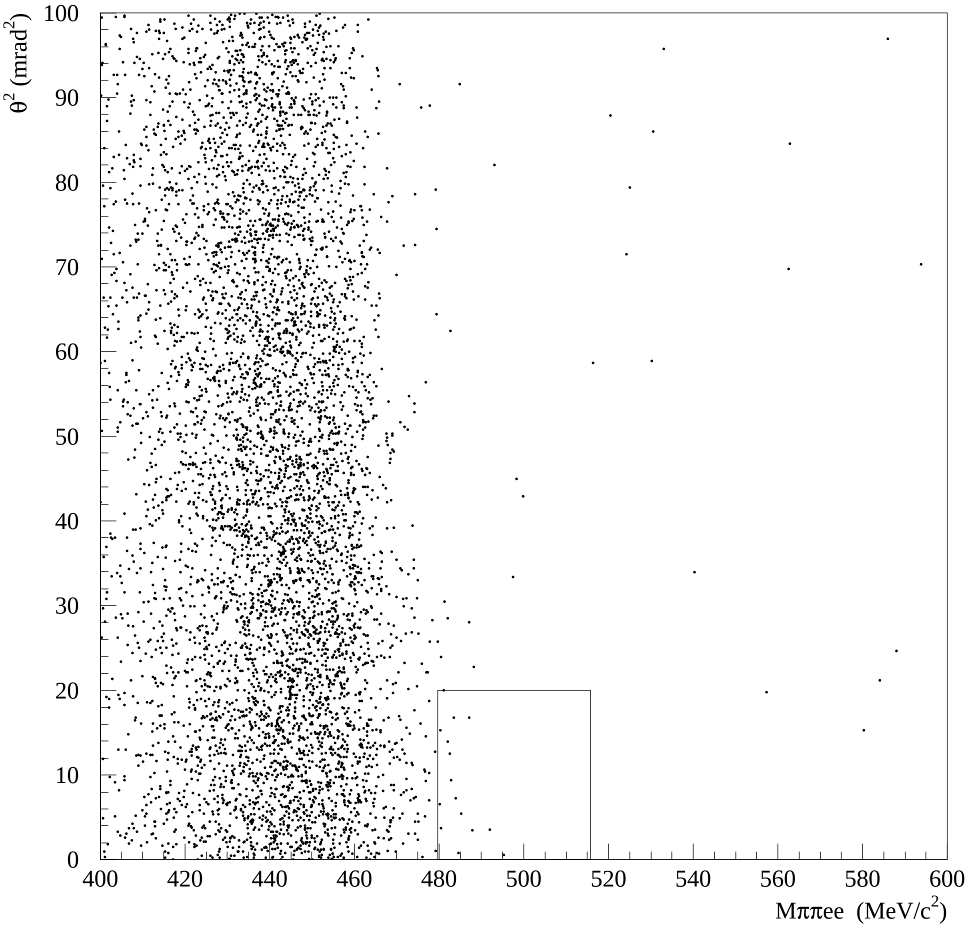

Figure 4.18: A scatter plot of $M_{\pi\pi ee}$ vs θ^2 for the $\pi^+\pi^-e^+e^-$ candidates obtained in Section 4.1.3.

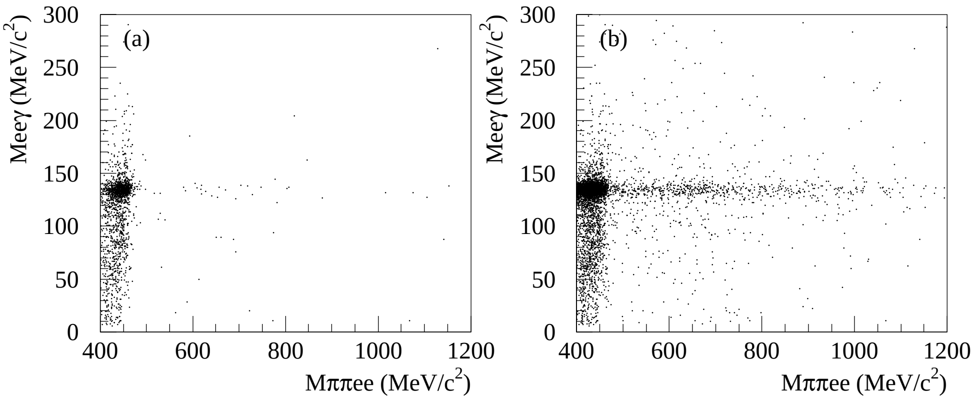

Figure 4.19: A scatter plot of $M_{ee\gamma}$ vs $M_{\pi\pi ee}$; (a) for the $\pi^+\pi^-e^+e^-$ candidates with a photon(s), and (b) for the events which are required to pass much looser θ^2 cut ($\theta^2 < 1000\mathrm{mrad}^2$). There exists a cluster around $M_{\pi\pi ee} \simeq 430MeV/c^2$ and $M_{ee\gamma} \simeq M_{\pi^0}$, which originated from the $K_L \to \pi^+\pi^-\pi^0_D$ mode. Also a clear band of $M_{ee\gamma}$ near the M_{π^0} is seen in (b).

M_{π^0}, it was the case of over-veto by the accidental activities. We found the loss to be less than a few per cent (see Section 4.4).

4.3.2 Backgrounds from K_L decay

Backgrounds from K_L decay could well be simulated by the Monte Carlo program from the viewpoint of their acceptance and efficiency of kinematical cuts. The estimation for each background source is discussed in order.

(a) $K_L \to \pi^+\pi^-\gamma$ with Photon Conversion A photon conversion following the decay $K_L \to \pi^+\pi^-\gamma$ could be misidentified as the $K_L \to \pi^+\pi^-e^+e^-$ events. Backgrounds from this sequence had the same decay products ($\pi^+\pi^-e^+e^-$) and invariant mass as the signal mode. These backgrounds, however, had features characteristic to the external photon conversion. Thus the cuts applied to M_{ee} and N_{shared} were expected to be effective, as discussed in the previous section. These cuts reduced photon conversion to the level of about 4%, as summarized in Table 4.2. Using the photon conversion probability (4.4×10^{-3}) and the known branching ratio of $K_L \to \pi^+\pi^-\gamma$ (4.6×10^{-5})[21], the effective branching ratio of this background mode was estimated to be less than 10^{-8}. Comparing with the expected single event sensitivity for the signal mode ($O(10^{-7})$), we concluded

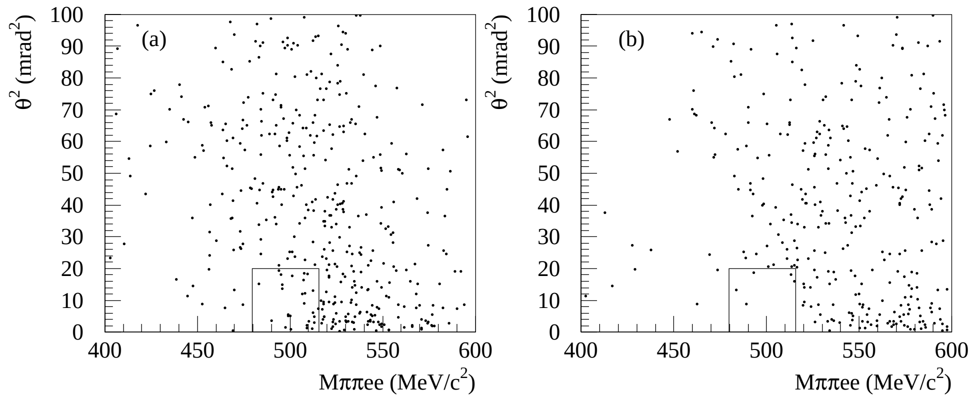

Figure 4.20: Scatter plots of θ^2 vs $M_{\pi\pi ee}$ for radiative K_{e3} events by the Monte Carlo simulation with the photon conversion and $e \to \pi$ misidentification. Events in the plots are not imposed the cuts on M_{ee} and N_{shared}. (a) In the case that a decayed electron was misidentified. (b) In the case that a converted electron was misidentified.

that the number of background events from $K_L \to \pi^+\pi^-\gamma$ was negligible in the signal box.

(b) Radiative K_{e3} with Photon Conversion and Misidentification $e \to \pi$
The number of backgrounds from radiative K_{e3} ($K_L \to \pi e\nu\gamma$), with internal or external photon conversion and $e \to \pi$ misidentification was estimated in the following procedure. We generated radiative K_{e3} events with a photon being converted into an e^+e^- pair by a Monte Carlo simulation. Then, one electron was intentionally misidentified as a pion in the analysis. We calculated kinematical quantities such as the invariant mass and θ^2 of $\pi\pi' ee$, where π' being a faked pion. Two cases were examined; (a) a decayed electron was misidentified and (b) a converted electron was misidentified. Resultant scatter plots of θ^2 vs $M_{\pi\pi ee}$ without the cuts on M_{ee} and N_{shared} are shown in Figure 4.20. Effective branching ratio of this type of backgrounds was roughly estimated as follows. The branching ratio of radiative K_{e3} is known to be 1.3% [21] and the photon conversion probability was 4.4×10^{-3}. The probability that an event fell into the signal box was found to be about 3% in (a) and 0.5% in (b), respectively. Furthermore, M_{ee} and N_{shared} cuts could reduce events in the plot (a) to the level of 4%. Finally, taking the misidentification ($e \to \pi$) probability to be 10^{-4} in the worst case, we estimated that the effective branching ratio of the background was $O(10^{-11})$. We could neglect this type of background completely.

(c) $K_L \to \pi^+\pi^-\pi^0_D$ Most events in the region $M_{\pi\pi ee} < M_{K_L}$ were expected to stem from the $K_L \to \pi^+\pi^-\pi^0_D$ mode with the photon being missed from detection. To reduce the contamination from $K_L \to \pi^+\pi^-\pi^0_D$, we chose the following method.

At first, assuming an existence of a photon, we defined the parameter χ^2_D:

$$\chi^2_D(\vec{p}_\gamma) = \left(\frac{M_{ee\gamma} - M_{\pi^0}}{\sigma_{M_{\pi^0}}}\right)^2 + \left(\frac{M_{\pi\pi ee\gamma} - M_{K_L}}{\sigma_{M_{K_L}}}\right)^2 + \left(\frac{\theta^2}{\sigma_{\theta^2}}\right)^2,$$

for an arbitrary photon momentum $\vec{p}_\gamma$. Here the standard deviations, $\sigma_{M_{\pi^0}}$, $\sigma_{M_{K_L}}$, and σ_{θ^2} were taken from the experimental distributions for M_{π^0}, M_{K_L} and θ^2, respectively. This parameter was a measure of consistency for the event to the $K_L \to \pi^+\pi^-\pi^0_D$ process. We determined $\vec{p}_\gamma$ by minimizing χ^2_D. Figure 4.21 shows χ^2_D distributions obtained by a Monte Carlo simulation and for the experimental data; (a) the simulated events for the $K_L \to \pi^+\pi^-e^+e^-$ mode through the M1 amplitude, (b) the same for the IB amplitude, (c) the simulated events for the $K_L \to \pi^+\pi^-\pi^0_D$ mode, and (d) the $\pi^+\pi^-e^+e^-$ candidates. The distributions in Fig.4.21(c) and (d) are similar to each other, confirming that the remaining backgrounds were mostly originated from this process. If resultant χ^2_D was less than 14 (equivalent to 3σ cut), we identified the event as $\pi^+\pi^-\pi^0_D$ and then rejected it. The background reduction factor of the method was estimated to be about 200 by using events from the Monte Carlo simulation.[7] The efficiency for the signal mode was also obtained by the simulation, and was found to be more than 90%. After this cut, the number of background events from $K_L \to \pi^+\pi^-\pi^0_D$ in the signal box was expected to be less than 1.

Two comments are in order here. We also applied this χ^2_D cut to the events identified as the $K_L \to \pi^+\pi^-\pi^0_D$ mode with the reconstructed photon being removed intentionally. Figure 4.22 shows the resultant χ^2_D distribution, indicating effectiveness of the method although the events in this case were distributed inside the phase space slightly different from the actual events.

The other comment was to point out the influence of the χ^2_D cut on the e^+e^- invariant mass distribution. Figure 4.23 shows the distribution of M_{ee} for the $K_L \to \pi^+\pi^-e^+e^-$ mode by a Monte Carlo simulation and that for the events rejected by the χ^2_D cut (represented by shaded histogram). The cut preferentially reduced the high M_{ee} events.

4.3.3 Result from $K_L \to \pi^+\pi^-e^+e^-$ Analysis

We have introduced the π^0 inclusive cut to remove backgrounds from the nuclear interactions and the χ^2_D cut to eliminate the $K_L \to \pi^+\pi^-\pi^0_D$ decay. We now

---

[7] The event sample studied was the $\pi^+\pi^-\pi^0_D$ events generated by the Monte Carlo simulation. They were analyzed as a $\pi^+\pi^-e^+e^-$ candidate; all the cuts described in Section 4.1.3 as well as the π^0 inclusive cut were imposed on them.

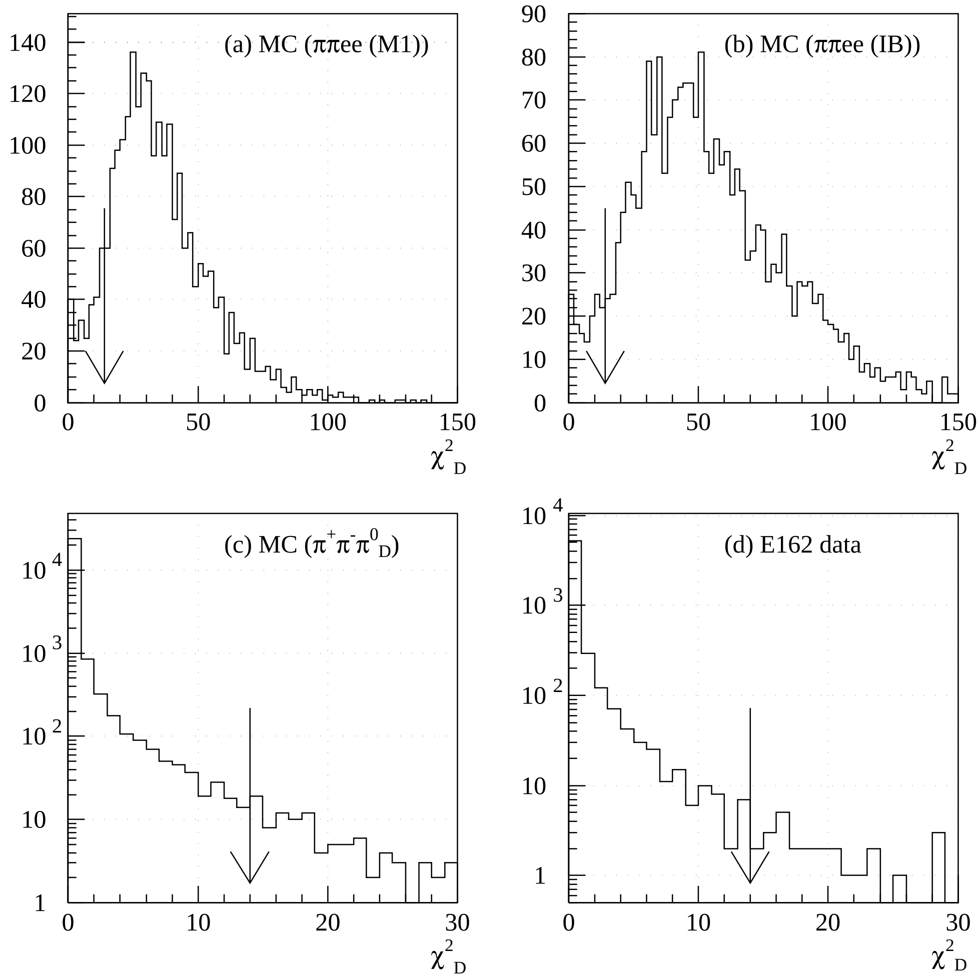

Figure 4.21: Distributions of χ^2_D, defined in the text; (a) the simulated events for $K_L \rightarrow \pi^+\pi^-e^+e^-$ through the M1 amplitude, (b) the same for the IB amplitude, (c) the simulated events for the $K_L \rightarrow \pi^+\pi^-\pi^0_D$ mode, and (d) the $\pi^+\pi^-e^+e^-$ candidates. The arrows in the figures represent the actual cut value.

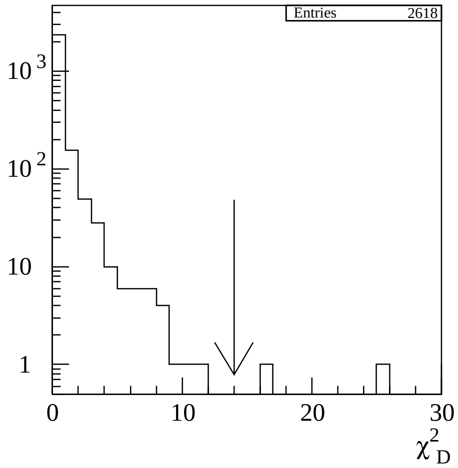

Figure 4.22: The χ^2_D distribution of reconstructed $K_L \to \pi^+\pi^-\pi^0_D$ events. The photon used in the reconstruction was removed intentionally and χ^2_D was calculated.

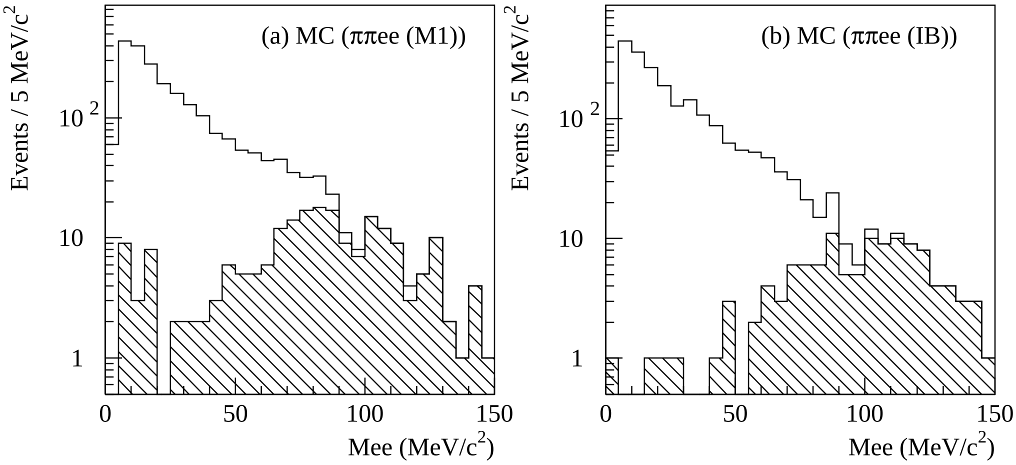

Figure 4.23: The distribution of M_{ee} for the $K_L \to \pi^+\pi^-e^+e^-$ mode by a Monte Carlo simulation. Events rejected by the χ^2_D cut are represented by shaded histogram. It is clear that this cut suppresses preferentially the high M_{ee} events.

appeal to our final cuts; the K_L mass cut and θ^2 cut. Figure 4.24 shows a scatter plot of $M_{\pi\pi ee}$ vs θ^2; there is no event left in the signal region.

We considered nuclear interactions and $K_L \rightarrow \pi^+\pi^-\pi^0_D$ as two major background sources. In the figure, the backgrounds, which distributed almost uniformly in the mass region above the K_L mass, are considered to originate from nuclear interactions. The number of backgrounds in the signal box was estimated as follows. In the area of $520MeV/c^2 \leq M_{\pi\pi ee} \leq 700MeV/c^2$ and $\theta^2 < 1000\text{mrad}^2$, there were 160 backgrounds. Assuming the same density, we found the expected number of backgrounds in the signal region to be 0.6.

Below the K_L mass, we considered that backgrounds were dominated by the $K_L \rightarrow \pi^+\pi^-\pi^0_D$ mode. We estimated by a Monte Carlo simulation that the number of this background was less than 1.

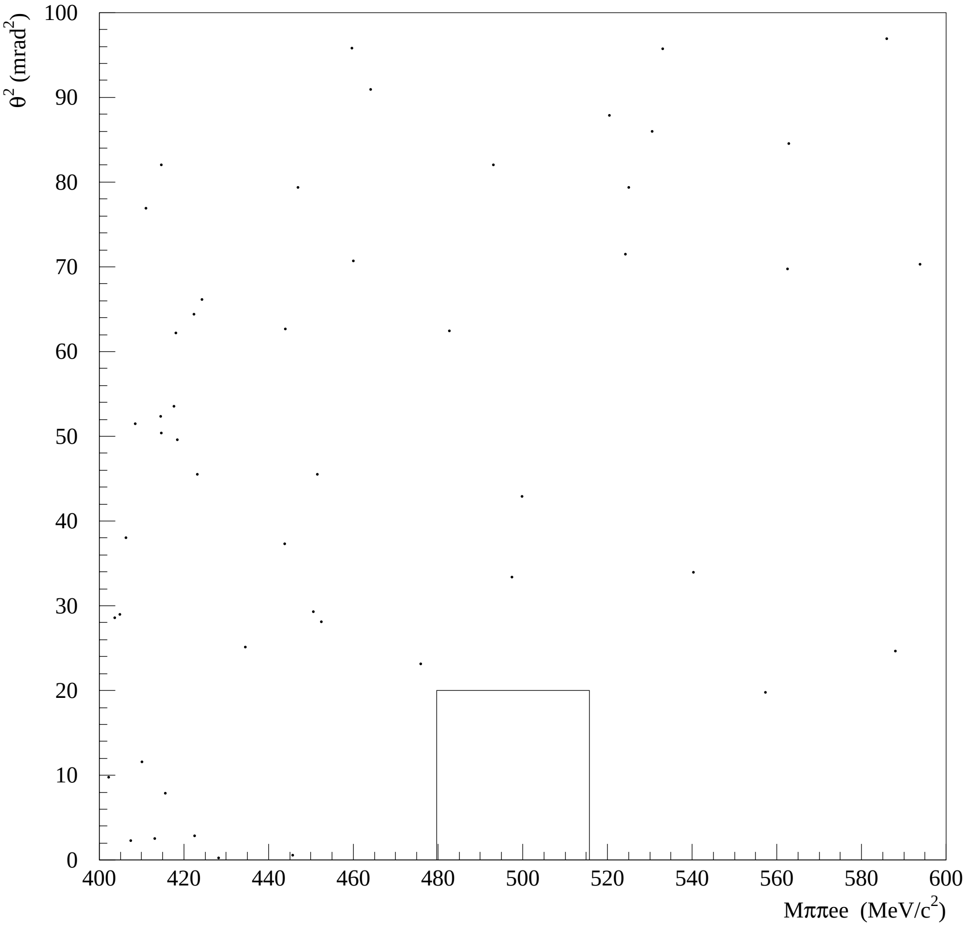

Figure 4.24: A scatter plot of $M_{\pi\pi ee}$ vs θ^2 after all the cuts. There is no event left in the signal box.

4.4 The Calculation of the Branching Ratio

The branching ratio of the decay $K_L \to \pi^+\pi^-e^+e^-$ was calculated by

$$Br(K_L \to \pi^+\pi^-e^+e^-) = Br(K_L \to \pi^+\pi^-\pi^0) \times Br(\pi^0 \to e^+e^-\gamma)$$
$$\times \frac{A(\pi^+\pi^-\pi^0_D)}{A(\pi^+\pi^-e^+e^-)} \cdot \frac{\eta(\pi^+\pi^-\pi^0_D)}{\eta(\pi^+\pi^-e^+e^-)} \cdot \frac{N(\pi^+\pi^-e^+e^-)}{N(\pi^+\pi^-\pi^0_D)}$$

where A, η and N denote acceptance, efficiency and observed number of events, respectively. We employed Monte Carlo simulations to determine acceptances. Since the acceptance for the $\pi^+\pi^-e^+e^-$ mode depended upon the amplitude assumed, the M1 and IB amplitudes were treated separately in the following calculations. The resultant values for acceptance and efficiency are summarized in Table 4.3.

We obtained the acceptance of 0.64×10^{-3} for $\pi^+\pi^-\pi^0_D$ [8] and $2.6 \times 10^{-3}(0.58 \times 10^{-3})$ for the M1(IB) amplitude.

Differences in efficiency between $\pi^+\pi^-e^+e^-$ and $\pi^+\pi^-\pi^0_D$ originated from the detector response as well as kinematical cuts. As to the detector response, most of the efficiencies were common to the two modes. The exception was the efficiency related to the photon for $K_L \to \pi^+\pi^-\pi^0_D$. If the position of a photon was close to other decay products in the calorimeter, two (or more) clusters might merge into one (cluster-merge). This caused the inefficiency in photon search; the item labeled as "γ-found" in the table. This effect could also lead to an error in energy and/or position measurement. It, in turn, would affect the track-cluster matching and the calculation of the invariant mass ($M_{ee\gamma}$ and/or $M_{\pi\pi ee\gamma}$); items shown as "4 matched" and "in the signal box" in the table. Taking the difference in efficiencies for those items above, we found the γ-related inefficiency to be about 20%.

There existed several kinematical cuts which caused differences in efficiency for the two modes. The requirement for charged pions to be inside the calorimeter fiducial region[9] caused the efficiency difference. It was found to be about 3%; the item shown as "π fiducial" in the table. The requirements for momenta (p_π) and their asymmetry (A_{+-}) imposed on charged pions were also the source of the efficiency difference. We estimated that the combined efficiencies were 97% for $\pi^+\pi^-\pi^0_D$ and 90%(81%) for the M1(IB) amplitude; the item named "Nuclear Int." in the table.

We rejected the events that contained $\pi^0 \to e^+e^-\gamma$ candidates for $K_L \to \pi^+\pi^-e^+e^-$. As described in the previous section, this cut was specific to the signal mode. The probability of over-veto due to this cut was estimated in the

---

[8] We used the phase space for the $K_L \to \pi^+\pi^-\pi^0$ decay and the Kroll-Wada spectrum [22] for the π^0 Dalitz decay. See Appendix A.

[9] The fiducial region was defined as the calorimeter acceptance that excluded the peripheral blocks. One of the two pions was required to be inside this region in order to reduce the misidentification ($e \to \pi$) due to shower leakage.

Table 4.3: Acceptances and efficiencies for $K_L \rightarrow \pi^+\pi^-e^+e^-$ and $K_L \rightarrow \pi^+\pi^-\pi^0_D$.

Condition		$\pi^+\pi^-\pi^0_D$	$\pi^+\pi^-e^+e^-$	
			M1	IB
Geometry [a]		2.15×10^{-3}	5.45×10^{-3}	1.16×10^{-3}
Pre cuts	$M_{ee} \geq 4MeV/c^2$ [b]	×0.677	-	-
Trigger	Level 1	×0.535	×0.556	×0.569
	Level 2	×0.817	×0.872	×0.881
	Total	×0.437	×0.485	×0.501
Total Acceptance		0.64×10^{-3}	2.64×10^{-3}	0.58×10^{-3}
Pre-sel.	Total	×0.922	×0.912	×0.921
Basic sel.	$N_{\text{trk}} \geq 4$	×0.744	×0.737	×0.747
	4 matched	×0.469	×0.540	×0.545
	Vertex	×0.937	×0.935	×0.922
	γ found	×0.939	—	-
	In the signal box	×0.921	×0.943	×0.953
	Total	×0.283	×0.351	×0.358
Kinematical	π fiducial [c]	×0.988	×0.966	×0.955
	Nuclear Int. [d]	×0.965	×0.898	×0.807
	γ conv. [e]	×0.918	×0.916	×0.924
	π^0 inclusive	-	×0.979	×0.984
	χ^2_D	-	×0.910	×0.943
	Total	×0.875	×0.708	×0.661
Total Efficiency		0.228	0.227	0.218
Effective acceptance		1.45×10^{-4}	5.99×10^{-4}	1.27×10^{-4}

[a] All of decay products into the calorimeter.

[b] Because of the technical reason of the programming, this cut was implemented in the event generation for the $K_L \rightarrow \pi^+\pi^-e^+e^-$ mode. See the explanation in Appendix A.

[c] The requirement for charged pion position in the calorimeter.

[d] Momentum cut for charged pions and its asymmetry A_{+-}.

[e] Cuts for M_{ee} and N_{shared}.

following way. There were two basic physics processes to be considered; one was an accidental photon which stemmed from different events, and the other was particle interactions due to its own decay products. Examples of the particle interactions, which caused a faked photon cluster, were $\pi^{\pm}$ interaction in the calorimeter and the external radiation from $e^{\pm}$ in materials. The former process sometimes created a wide-spread cluster which might be misidentified as two clusters. The latter process, especially radiation before the magnet, created an extra neutral cluster. These effects were estimated by the simulation and were found to cause 2% over-veto probability; the item shown as "π^0-inclusive" in the table.

The accidental effect was studied by analyzing the properties of extra photons in the $K_L \to \pi^+\pi^-\pi^0_D$ events. Actually, we attempted to calculate the invariant mass of $ee\gamma$ with photons other than the correct one, and we then examined whether or not another π^0 candidate (within 3σ of M_{π^0}) was found. The loss was found negligible and thus is not listed in the table.

The χ^2_D cut was also applied only to the $K_L \to \pi^+\pi^-e^+e^-$ mode, and its efficiency for the M1(IB) amplitude was found to be 91%(94%).

Summing up all the factors described above, we obtained $A \cdot \eta$ for the $K_L \to \pi^+\pi^-\pi^0_D$ and two amplitudes in the $K_L \to \pi^+\pi^-e^+e^-$ to be 1.45×10^{-4}, 5.99×10^{-4} and 1.27×10^{-4}, respectively. Taking the relative strength of two amplitudes in $K_L \to \pi^+\pi^-e^+e^-$ presented in Ref.[5], reviewed in Chapter 1, we found the combined $A \cdot \eta$ to be 4.2×10^{-4}.

The observed number $N(\pi^+\pi^-\pi^0_D)$ for the $K_L \to \pi^+\pi^-\pi^0_D$ mode was 2618 while $N(\pi^+\pi^-e^+e^-)$ was taken to be 2.3 for the upper limit at 90% confidence level. Finally we used the known branching ratios for the normalization mode of $Br(K_L \to \pi^+\pi^-\pi^0) = 0.1256$ and $Br(\pi^0 \to e^+e^-\gamma) = 1.198 \times 10^{-2}$ [21].

We obtained the upper limits for its branching ratio: 3.2×10^{-7} for M1 and 15×10^{-7} for IB at 90% confidence level. In conclusion, using the combined $A \cdot \eta$ for the $K_L \to \pi^+\pi^-e^+e^-$, we placed a 90% confidence level upper limit on the mode:

$$Br(K_L \to \pi^+\pi^-e^+e^-; M_{ee} \geq 4MeV/c^2) < 4.6 \times 10^{-7} \ (90\% C.L.).$$

Chapter 5

Conclusion

In this thesis, the study for the decay mode $K_L \to \pi^+\pi^-e^+e^-$ has been performed using the KEK-E162 data before summer in 1996.

After various cuts to reduce backgrounds, we obtained 2618 $K_L \to \pi^+\pi^-\pi^0_D$ events for the normalization of the number of K_L decays. As for the target mode $K_L \to \pi^+\pi^-e^+e^-$, we found no event in the signal region.

Using the acceptance and efficiency obtained by Monte Carlo simulation, we calculated the single event sensitivity for the decay mode, for two amplitudes in the matrix element separately. Multiplying a factor of 2.3, Poisson upper limit at the 90% confidence level for null observation, we found the upper limits for its branching ratio of 3.2×10^{-7} for M1 amplitude and 15×10^{-7} for IB amplitude. Taking the relative strength of these two amplitudes presented in Ref.[5], we placed a 90% confidence level upper limit on the mode:

$$Br(K_L \to \pi^+\pi^-e^+e^-; M_{ee} \geq 4MeV/c^2) < 4.6 \times 10^{-7} \ (90\% C.L.).$$

This result has improved the previous upper limit by a factor of 5.

We are going to take more data aiming to establish this rare decay mode and determine its branching ratio. The single event sensitivity reaches the level of theoretical prediction even at this time. We expect to observe about 10 $\sim$ 20 events till the end of this experiment. Also, efforts to reduce backgrounds should be done to confirm the decay mode. One of the major source of remaining backgrounds for the mode was thought to be nuclear interactions of neutrons in the beam with residual gas atoms in the decay volume. We plan to evacuate the decay volume in the next phase of this experiment, and expect to eliminate those backgrounds.

Appendix A

Monte Carlo Simulation

In this appendix, the Monte Carlo simulation of the experiment is described. Monte Carlo (MC) simulation was used to obtain acceptances of $K_L \to \pi^+\pi^-e^+e^-$ and $K_L \to \pi^+\pi^-\pi^0_D$, to examine physics backgrounds from other K_L decay, and so on. Our simulation program, which was based on GEANT 3.21 [19], simulated the processes such as K_L decay, flights of decay products, detector response, and interactions occurred in materials in the experiment. GEANT is a system of detector description and simulation tools, developed at CERN and having been used in many particle physics experiments.

At first, the simulation of K_L decay is described. Then, the transportation of particles which was determined by parameters in GEANT codes, and the detector simulation are mentioned in order. Finally, the treatment of beam-originated backgrounds is discussed, which could not be simulated as elementary processes.

A.1 The simulation of K_L decays

The generation of neutral kaons was done by a simple method. First, a source point was determined uniformly in the target region, a 10-mm-diameter and 60-mm-long cylinder. Next, a position at the entrance of the decay volume was determined within the area corresponding to the solid angle of $\pm 4\text{mrad} \times \pm 20\text{mrad}$, in the approximation of uniform distribution.[1] Then, the K_L momentum at the target was determined, taking its distribution obtained by KEK-E137 group [23] who had used the same beam line previous to us and had taken data at the same production angle (2°). Figure A.1 shows the distribution of K_L momentum at the production target. We used the momentum range from 1 GeV/c to 10 GeV/c in the following step. If the K_L decay occurred before the entrance of the decay volume, or it passed through the decay volume, the program went back to the beginning of the K_L generation. Once the K_L decayed in the decay volume, the

---

[1] This method was not equal to the uniform solid angle distribution. Also note that some distortion would exist in vertical direction due to the production angle.

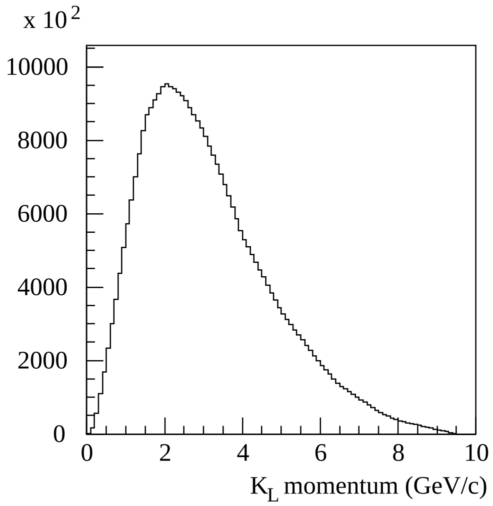

Figure A.1: K_L momentum spectrum used for the Monte Carlo simulation.

control of the process moved to the routine which described kinematics of the specific decay mode.

$K_L \to \pi^+\pi^-\pi^0_D$ includes two decay processes. In the $\pi^0 \to e^+e^-\gamma$ decay, we used the Kroll-Wada spectrum [22]. In the $K_L \to \pi^+\pi^-\pi^0$ decay, we used both the phase space distribution and the energy dependence of Dalitz plot with the parameters summarized in [21]. There existed large difference in the $M_{\pi\pi}$ distribution, and the experimental data agreed with the result from the former, as can be seen in Figure A.2. The acceptance using the phase space was found to be about 15% larger than that using Dalitz plot parameters. We stood the conservative side in placing the upper limit on the signal mode, and thus adopted the events using the phase space in the calculation of the sensitivity.

In case of the $K_L \to \pi^+\pi^-e^+e^-$ decay, we employed the distribution obtained by the calculation of the matrix element in Ref.[5]. By considering the sensitivity of our experiment, we only used terms concerned with M1 and IB contributions explained in the Chapter 1. We also neglected the interference term between M1 and IB contribution, which was proportional to $\sin\phi\cos\phi$. This simplification was valid in the approximation that the acceptance was flat to the angle ϕ and then no contribution remained by the integration of ϕ. The electron mass in the calculation was also neglected. This approximation caused the disagreement in the low invariant mass region of e^+e^- pair (M_{ee}). Figure A.3 shows the comparison between the generated distribution of M_{ee} reduced by M_{K_L} ($\sqrt{y}$) and those in Ref.[5], which were read from the represented figure in the paper. In the region below $M_{ee} = 4MeV/c^2$, left side of the line in the figure, there was obvious discrepancy. So, we used only the region $M_{ee} \geq 4MeV/c^2$ in the calculation of the acceptance and efficiency. Fortunately, this limitation was also required from

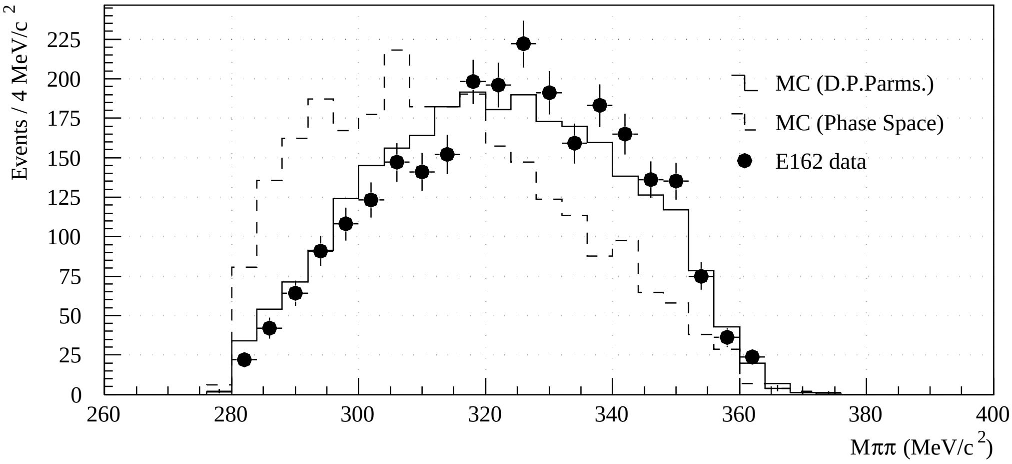

Figure A.2: The comparison of the $M_{\pi\pi}$ distributions for $K_L \to \pi^+\pi^-\pi^0_D$ between Monte Carlo events and the experimental data. The circles with bar show the distribution of experimental data. Two histograms represent the $M_{\pi\pi}$ distributions of simulated events; the histogram drawn by the solid line indicates the result of the events using the Dalitz plot parameters, while the histogram drawn by dashed line represents that by using the phase space distribution.

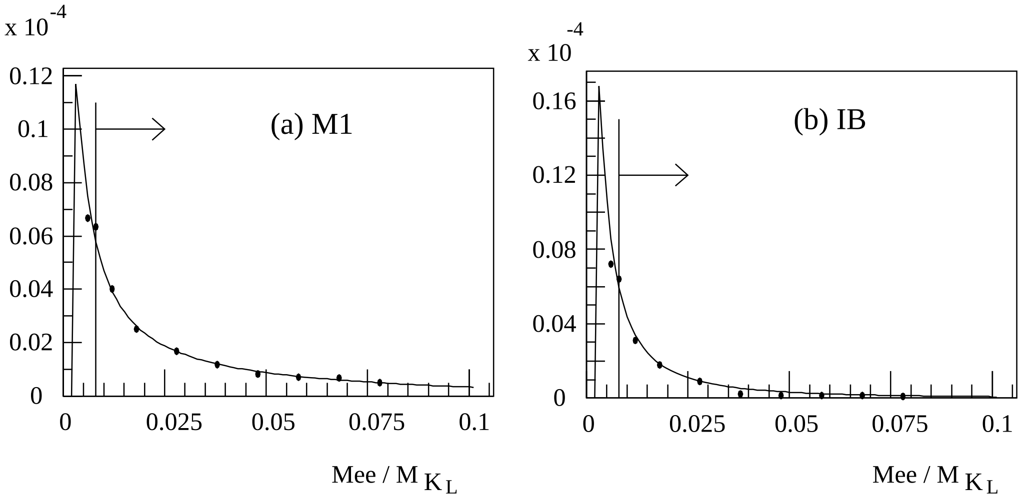

Figure A.3: The invariant mass of e^+e^- pair of the generated $K_L \to \pi^+\pi^-e^+e^-$ events for (a) M1 and (b) IB. The line represents the distribution generated by our simulation program and the round plot shows the values in the reference, which were read from the figure represented in the paper.

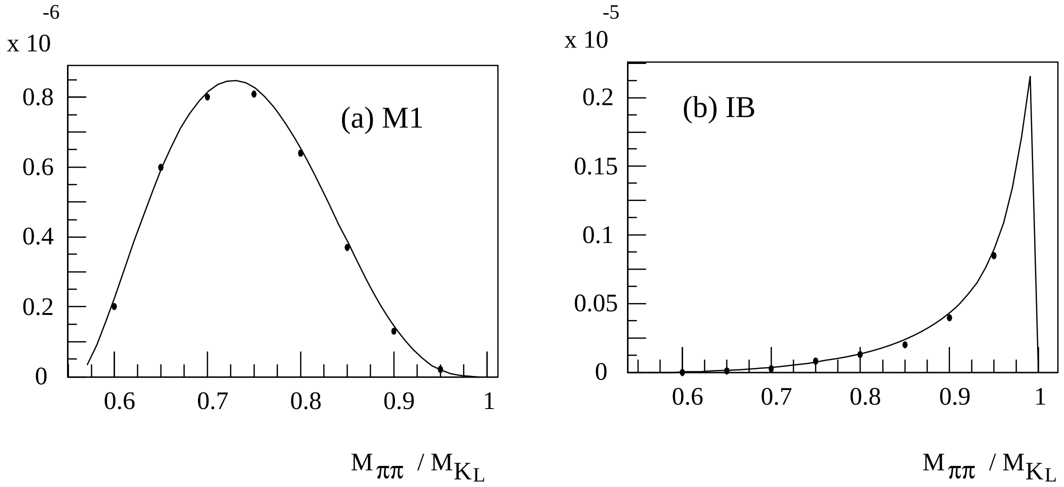

Figure A.4: The invariant mass of $\pi^+\pi^-$ pair of the generated $K_L \to \pi^+\pi^-e^+e^-$ events for (a) M1 and (b) IB. The line represents the distribution generated by our simulation program and the round plot shows the values in the paper, by same method as previous figure.

the viewpoint of the rejection of photon conversion backgrounds.

Same plot for the invariant mass of $\pi^+\pi^-$ ($M_{\pi\pi}$) reduced by M_{K_L} ($\sqrt{x}$), is also shown in Figure A.4, and the generated distribution found to be good agreement with the result in the paper.

The contributions from M1 and IB components were treated separately in order to know the dependence of the acceptance and efficiency on the mechanism in the matrix element. We found that the acceptance of the two were quite different in our experiment, summarized in Table 4.3.

A.2 The transportation of particles

The daughter particles from the K_L decay were transported in the detector under the control of GEANT system. When they passed through detector materials, various interactions occurred. The material list set in the program is shown in Table A.1. In case of charged particles, multiple scattering was simulated using a Moliere scattering distribution. The bremsstrahlung by electrons and the conversion by photons occurred in detector materials. As for charged pions, decay in flight and nuclear interactions with scintillator planes were also simulated.

Table A.1: List of thickness and radiation lengths of material.

Elements	Material	Thickness	
		in cm	in Radiation Length
Decay Volume	Helium	410.0	7.7×10^{-4}
	Window (Al+Mylar)	60 μm [a]	2.0×10^{-4}
TC0F	Plastic Scintillator	0.15	3.6×10^{-3}
TC0R	Plastic Scintillator	0.15	3.6×10^{-3}
DC1	Gas(Ar+ethane)	3.7	3.1×10^{-4} ea.
	Sense wire plane (×2)	0.1 [b]	1.8×10^{-4} ea.
	Field wire plane (×3)	0.1 [b]	6.1×10^{-4} ea.
	Window (Al+Mylar) (×2)	40 μm	1.4×10^{-4} ea.
DC2	same as DC1		
GC	Gas(N_2)	210.8	6.3×10^{-3}
	Window (×2)	60 μm ea. [a]	1.0×10^{-4}
	Mirror (Acryl)	0.2	5.8×10^{-3}
TC1X	Plastic Scintillator	0.26	6.2×10^{-3}
DC3	same as DC1		
DC4	same as DC1		
TC2Y	Plastic Scintillator	1.0	2.3×10^{-2}
TC2X	Plastic Scintillator	1.0	2.3×10^{-2}
TC3X	Plastic Scintillator	1.0	2.3×10^{-2}
Calorimeter	Pure CsI	30.0	1.6×10^{1}
Air Gap	Air		3.04×10^{4}

[a] The aluminum was substituted by the Mylar with equal radiation length.

[b] Each wire plane was treated as a thin sheet placed at Z position of the wire center.

A.3 The detector simulation

The simulation of the detector was categorized into two parts. One was the part simulated by GEANT system, such as the development of electromagnetic shower in the calorimeter and the emission of Cherenkov light by electrons.[2] These were involved as elementary processes in the event generation. The other was that concerning with the detector resolution. The position resolution of drift chambers and energy resolution of the calorimeter, except for the shower fluctuation contribution, were set after the event generation. In the simulation for the analysis in this thesis, the resolution of all chambers were set to be 300 μm, which was worse than that obtained from the experimental data, shown in Chapter 2. The energy resolution was considered to originate only from the shower leakage which was simulated in the generation. It resulted in much better value ($\sim 1.7\%/\sqrt{E}$) than the experimental one, and caused the disagreement between simulated and experimental distributions, for example, in the invariant mass resolution of $M_{ee\gamma}$. It was not a serious matter since we adopted the results from the experimental distribution when we determined the cut values in those distributions.

A.4 Consideration of beam-originated backgrounds

Since we could not well estimated numbers of photons and neutrons in the neutral beam, backgrounds associated with the beam were not simulated as elementary processes. They were studied and estimated only by using experimental data, as discussed in Chapter 4.

Also, effects of the beam intensity, such as accidental hits in the detector and two simultaneous K_L decays, were not simulated. The influence was examined by mixing accidental activities in experimental data into simulated data. Data mixed was taken simultaneously with physics modes by the random trigger (Trig.4) as described in Chapter 2. The amalgamation of accidental activities affected all of the hit information, ADC counts in the calorimeter, and drift time of chambers. TDC data involving drift time of chambers were overlay by accidental hits arriving before the event time. This modification forced the arrival time of the detector to go out of the on-time window. ADC data in the calorimeter was modified that energy deposit by accidental activities was summed up to the correct data, which resulted in incorrect measurement of electron and photon energy, and/or misidentification by the change of E/p value.

Although absolute values of the effects could not be understood in detail, most of them was canceled out by taking the ratio of the two modes: the signal mode $K_L \to \pi^+\pi^-e^+e^-$ and the normalization mode $K_L \to \pi^+\pi^-\pi^0_D$. The most important effect remained was that on the efficiency of photon detection in the

---

[2] The procedure to trace a Cherenkov light to the detecting PMT was coded by us, considering the shape of the reflecting mirror and the light collection funnel.

decay $K_L \to \pi^+\pi^-\pi^0_D$. A signal by a photon would be masked by accidental activities in the calorimeter. Its effect was estimated by the mixing method above, and was found to be less than 5%. The influence on other processes, such as the decline of the tracking efficiency by spurious hits, was examined in both modes and was found to be negligible after taking their ratio. Since the validity of the mixing method was not enough examined by the experimental data, the result here was not used in the calculation of the upper limit of the branching ratio.[3]

---

[3] The effect described here resulted in the lower upper limit if used.

Bibliography

[1] J. H. Chrestenson et al., Phys. Rev. Lett. **13**, 138 (1964).

[2] M. Kobayashi and T. Maskawa, Prog. Theor. Phys. **49**, 652 (1973).

[3] L. Wolfenstein, Phys. Rev. Lett. **13**, 562 (1964).

[4] E. J. Ramberg et al., Phys. Rev. Lett. **70**, 2529 (1993).

[5] L. M. Sehgal and M. Wanninger, Phys. Rev. **D46**, 1035 (1992), *ibid.* **46**, 5209 (E) (1992).

[6] P. Heilinger and L. M. Sehgal, Phys. Rev. **D48**, 4146 (1993).

[7] M. Y. Balats et al., Sov. J. Nucl. Phys. **38**, 556 (1983).

[8] Y. W. Wah, Results and Plans for the Fermilab K^0 Decay Program, in *Proceedings of the XXVI International Conference on High Energy Physics,* Dallas, Texas, 1992, edited by J. R. Sanford, AIP Conf. Proc. No.272, New York, 1992, AIP.

[9] T. Yamashita et al., Nucl. Inst. Meth. **A283**, 709 (1989).

[10] T. Yamashita et al., Nucl. Inst. Meth. **A317**, 213 (1992).

[11] O. Sasaki, IEEE Trans. Nucl. Sci. **38**, 281 (1991).

[12] S. Kubota et al., Nucl. Inst. Meth. **A268**, 275 (1988).

[13] H. Kurashige et al., IEEE Trans. Nucl. Sci. **35**, 1018 (1988).

[14] O. Sasaki et al., IEEE Trans. Nucl. Sci. **35**, 342 (1988).

[15] H. Hinterberger and R. Winston, Rev. Sci. Instr. **37**, 1094 (1966).

[16] C. R. Kerns, IEEE Trans. Nucl. Sci. **24**, 353 (1977).

[17] H. Kurasige et al., IEEE Trans. Nucl. Sci. **41**, 1267 (1994).

[18] T. K. Ohska et al., IEEE Trans. Nucl. Sci. **33**, 98 (1986).

[19] Detector Description and Simulation Tool, CERN Program Library Long Writeup W5013.

[20] G. A. Akopdjanov et al., Nucl. Inst. Meth. **140**, 441 (1977).

[21] Particle Data Group, R. M. Barnett et al., Phys. Rev. **D54**, 1.

[22] N. M. Kroll and W. Wada, Phys. Rev. **98**, 1355 (1955).

[23] T. Akagi et al., Phys. Rev. **D51**, 2061 (1995).